IMAGE FUSION FOR IMPROVING SPATIAL RESOLUTION OF MULTISPECTRAL SATELLITE IMAGES

A THESIS SUBMITTED TO
THE GRADUATE SCHOOL OF NATURAL AND APPLIED SCIENCES
OF
MIDDLE EAST TECHNICAL UNIVERSITY

BY

DENİZ ÜNLÜSOY

IN PARTIAL FULFILLMENT OF THE REQUIREMENTS
FOR
THE DEGREE OF MASTER OF SCIENCE
IN
GEOLOGICAL ENGINEERING

SEPTEMBER 2013

APPROVAL OF THE THESIS

IMAGE FUSION FOR IMPROVING SPATIAL RESOLUTION OF MULTISPECTRAL SATELLITE IMAGES

submitted by **DENİZ ÜNLÜSOY** in partial fulfillment of the requirements for the degree of **Master of Science in Geological Engineering Department, Middle East Technical University** by,

Prof. Dr. Canan Özgen _____
Dean, Graduate School of **Natural and Applied Sciences**

Prof. Dr. Erdin Bozkurt _____
Head of Department, **Geological Engineering Dept., METU**

Prof. Dr. Mehmet Lütfi Süzen _____
Supervisor, **Geological Engineering Dept., METU**

Examining Committee Members:

Prof. Dr. Nuretdin Kaymakçı _____
Geological Engineering Dept., METU

Prof. Dr. Mehmet Lütfi Süzen _____
Geological Engineering Dept., METU

Assist. Prof. Dr. Atilla Arda Özacar _____
Geological Engineering Dept., METU

Dr. Çağıl Kolat _____
VERİSİS Veri ve İletişim Sistemleri A.Ş.

Serkan Öztan _____
ENVY Enerji ve Çevre Yatırımları A.Ş.

Date: _____

I hereby declare that all information in this document has been obtained and presented in accordance with academic rules and ethical conduct. I also declare that, as required by these rules and conduct, I have fully cited and referenced all material and results that are not original to this work.

Name, Last name: DENİZ ÜNLÜSOY

Signature :

ABSTRACT

IMAGE FUSION FOR IMPROVING SPATIAL RESOLUTION OF MULTISPECTRAL SATELLITE IMAGES

Ünlüsoy, Deniz
M.S., Department of Geological Engineering
Supervisor: Prof. Dr. M. Lütfi Süzen

September 2013, 83 pages

In this study, four different image fusion techniques have been applied to high spectral and low spatial resolution satellite images with high spatial and low spectral resolution images to obtain fused images with increased spatial resolution, while preserving spectral information as much as possible. These techniques are intensity-hue-saturation (IHS) transform, principle component analysis (PCA), Brovey transform (BT), and Wavelet transform (WT) image fusion. Images used in the study belong to Çankırı region, and are obtained from Advanced Spaceborne Thermal Emission and Reflection Radiometer (ASTER) satellite.

MATLAB is used to build a GUI to apply and to present the results of the image fusion algorithms. Subjective (visual) and objective evaluation of the fused images have been performed to evaluate the success of the approaches. The objective evaluation methods include correlation coefficient (CC), root mean squared error (RMSE), relative global dimensional synthesis error (ERGAS), and high-pass correlation coefficient (HPCC). For visual evaluation, sulphate index (SI) and mafic index (MI) specific to thermal infrared (TIR) and hydroxyl index "a" (OHIa) specific to shortwave infrared (SWIR) bands are used.

The results indicate that the IHS transformation provides the highest performance in increasing lower spatial resolutions of TIR and SWIR bands of the ASTER images to higher spatial resolution of visible near infrared (VNIR) bands, at the expense of some loss of spectral information. PCA and BT methods, on the other hand, perform better with respect to preservation of spectral information, while being less successful in increasing spatial resolution. WT performs next to IHS transformation for improving spatial resolution and comes after PCA and BT methods with respect to the preservation of spectral information.

Keywords: Remote sensing, Image fusion, IHS transformation, Brovey transformation, Wavelet transformation, PCA.

ÖZ

ÇOKLU SPEKTRAL GÖRÜNTÜLERİN ALANSAL ÇÖZÜNÜRLÜĞÜNÜN GÖRÜNTÜ BİRLEŞTİRME YÖNTEMİ İLE GELİŞTİRİLMESİ

Ünlüsoy, Deniz
Yüksek Lisans, Jeoloji Mühendisliği Bölümü
Tez Yöneticisi: Prof. Dr. M. Lütfi Süzen

Eylül 2013, 83 sayfa

Bu çalışmada dört değişik görüntü birleştirme tekniği yüksek spektral, düşük alansal çözünürlüklü uydu görüntüleri ile yüksek alansal ve düşük spektral uydu görüntülerine uygulanmıştır. Çalışmanın temel amacı, spektral özellikleri olabildiğince koruyarak alansal çözünürlüğü yüksek görüntülerin elde edilmesidir. Kullanılan teknikler yoğunluk-renk tonu-doygunluk (IHS) dönüşüm temelli görüntü birleştirme, temel bileşenler analizi (PCA) temelli görüntü birleştirme, Brovey dönüşümü (BT) temelli görüntü birleştirme ve dalgacık dönüşümlü (WT) görüntü birleştirme olarak seçilmiştir. Çalışmada ASTER uydusundan alınan ve Çankırı yöresine ait görüntüler kullanılmıştır.

Görüntü birleştirme işleminin yapılıp, sonuçlarının sunulması ve karşılaştırılması için MATLAB platformu üzerinde bir arayüz geliştirilmiştir. Farklı tekniklerle elde edilen yüksek çözünürlüklü görüntüler, orijinal görüntüler ve birbirleri ile karşılaştırılmıştır. Korelasyon katsayısı (CC), ortalama karesel hata (RMSE), göreceli küresel boyutsal sentez hatası (ERGAS) ve yüksek geçişli korelasyon katsayısı (HPCC) nesnel değerlendirmede kullanılmıştır. Öznel değerlendirme için termal kızılötesine (TIR) özgü mafik (MI) ve sülfat (SI) indisleri ve kısa dalga kızılötesi (SWIR) kanallarına özgü hidroksil "a" indisi (OHIa) gibi spektral indisler kullanılmıştır.

Görüntü birleştirme uygulamalarından elde edilen sonuçlara göre, IHS temelli görüntü birleştirme tekniği alansal çözünürlüğün arttırılmasında en yüksek performansı göstermektedir. Ancak bu teknik diğer tekniklere göre spektral bilgide daha fazla kayba neden olmaktadır. PCA ve BT teknikleri ise spektral özellikleri korumada daha başarılı olmalarına karşın, alansal çözünürlüğün arttırılmasında IHS ve WT'nin gerisinde kalmaktadır. WT alansal çözünülürlüğün arttırılmasında IHS'den, spektral bilginin korunmasında ise PCA ve BT'den sonra gelmektedir.

Anahtar Kelimeler: Uzaktan algılama, Görüntü birleştirme, Yoğunluk-renk tonu-doygunluk dönüşümü, Brovey dönüşümü, Dalgacık dönüşümü, Temel bileşenler analizi dönüşümü

To my family

ACKNOWLEDGEMENTS

I would like to take this opportunity to express my most sincere gratitude to my supervisor Prof. Dr. Mehmet Lütfi Süzen, who introduced me to the subject of remote sensing, for all his help, guidance and suggestions through the development of this study.

I would like to express my special thanks to my family for their continuous encouragement, understanding, and moral support.

TABLE OF CONTENTS

LIST OF TABLES

TABLES

LIST OF FIGURES

FIGURES

CHAPTER 1

INTRODUCTION

1.1. Purpose and Scope

Remote sensing simply means obtaining information about an object without touching the object itself. It has two facets; acquiring data by a device at a distance from the object, and analysing data of the object to interpret its physical properties. These two aspects are closely connected to each other.

The basic fact in remote sensing is that different wavelength ranges of the electromagnetic spectrum is reflected or emitted from an object at certain intensity, which is dependent upon the physical and compositional attributes of the object. Remote sensing today plays an important role in geological analysis of large areas which utilizes electromagnetic spectrum not only within the visible range but also beyond the visible range that human eye can't perceive.

The unique spectral signatures of rocks, minerals, and other geological elements are used to map these geological elements in large areas in a short time using remote sensing data. Earth observation systems generally include infrared region of the electromagnetic spectrum, which include the visible-near infrared (VNIR) and shortwave infrared (SWIR). Further some imaging systems such as LANDSAT and ASTER cover thermal infrared (TIR) region, which is a mid-long wave infrared region in the spectrum. TIR radiance values of objects can also be used for mapping similar to VNIR and SWIR.

As useful as it may be, remote sensing like any tool requires continuously increasing improvement. Similarly advances in the technology necessitate the improvement of the methods accordingly, both in terms of accuracy and precision. Image fusion is one of the techniques that are employed to increase spatial and/or spectral resolution of remotely sensed data by fusing a high spatial but low spectral resolution image with a low spatial high spectral resolution image.

The purpose of this study is to fuse TIR and SWIR bands of ASTER with VNIR bands, while evaluating the multispectral infrared data with increased resolution for lithological discrimination and mapping using the basic image fusion techniques. Evaluation techniques will reveal which methods provide the best information and show how they compare to the original non-fused data. To accomplish these objectives, a graphical user interface (GUI) was prepared using the commercial software MATLAB and its Image Processing toolbox which contains commands and utilities that are commonly used in image processing applications.

1.2. Literature Survey

The most common practice in image fusion, for the purpose of increasing spatial resolution, is to fuse panchromatic images with multispectral images. In this literature survey papers on thermal imagery and image fusion used in earth observation were researched. It is noted in the literature that in image fusion applications, thermal or other more specific bands are rarely used and most image fusion attempts using near infrared bands involves fusing it with the entire multispectral visual bands. The majority of the applications involve security and medical imaging. Yet the major use of thermal imaging lies in forestry, oceanography, and agriculture. There are also some papers in literature that make use of pansharpening of thermal data with image fusion and some using ASTER data. The literature survey to follow is concentrated on the work more closely related to the problem in hand.

Collins, et al (1997), in their paper analysed "thermal imagery from the Spatially Enhanced Broadband Array Spectrograph System (SEBASS) for target detection purposes. The push-broom sensor was operated as part of the Western Rainbow experiment in October 1995. Data from 7.8-13.4 microns were collected in 128 wavelength bands, with 128 pixels in the cross-track direction. The data set had a nominal ground-resolution of better than one meter. Analysis techniques normally used in the reflective domain, with traditional imaging spectrometers, were used for the thermal data. Analysis was done in both the radiance and emissivity domains, following careful thermal calibration and atmospheric compensation. The techniques utilized were principal components, spectral angle mapper, and spectral matched filter. All were successful, with the first two showing a success rate comparable to that found in similar experiments in the reflective domain. The principal components technique was successful in discriminating man-made objects and disturbed earth from the desert background, much as expected. It was also successful in distinguishing between different categories of man-made objects. Of the latter two techniques, the spectral matched filter was more successful. This relatively greater success is attributed to the sensitivity of the spectral angle mapper to calibration errors, particularly in the conversion from radiance to emissivity. Analysis of the long-wave infrared (LWIR) spectral data resulted in the successful detection of military targets and demonstrated a significant improvement in detection success rate over traditional single-band, infrared forward looking infrared radiometer (FLIR) imagery. Both target and background materials were detected, characterized, and classified using standard hyperspectral analysis algorithms historically used for the analysis of data collected within the visible and near-infrared regions of the electromagnetic spectrum. Principal components analysis demonstrated that SEBASS was capable of collecting thermal spectral data with sufficient spectral and radiometric resolution to detect and discriminate military targets. The analysis revealed that the data collected by SEBASS were not only capable of discriminating between the majority background and man-made materials, but were also capable of discriminating between classes of man-made materials." In this paper the importance of the spectral resolution of thermal infrared band is presented.

The report written by Yin and Malcolm (2000) is about the fusion of thermal images with optical images. It is stated that "the mechanisms that produce thermal images are different from those that produce visual images. Thermal image produced by an object's surface can be interpreted to identify these mechanisms. Thus thermal images can provide information about the object being imaged which is not available from a visual image. The objective of this project is to study the integration of information obtained from thermal (infrared) images

and that obtained from visual intensity images. The study is conducted by investigating the fusion techniques in an application of the non-destructive moisture detection for construction. Several fusion approaches have been explored. The approaches make available information that cannot be obtained by processing visual images alone or thermal images alone, and which is useful for the interpretation of imaged scenes. The approach developed identifies the type of information to be extracted from each image and establishes a way of combining this information for this general class of applications. In the project, a primary study on multiple sensor fusion is performed. Applications of these approaches in non-destructive test of construction slab show that the proposed fusion approaches do help to enhance some weak features exhibited both in optical and particularly in infrared images. Through the study of this project, it can be concluded that fusion does provide an intelligent and cost-effective way to achieve reliable perception and detection in the case where the signal is weak and cannot be reliably detected by using only one kind of available sensor. Thus, it is concluded that fusion of multiple sensors has a good prospect in industrial applications." This report shows methods for fusing thermal and optical images and gives mathematical equations such as linear fusion as displayed below that might be useful for fusion attempts in the present thesis work.

$$I_{fused}(x, y)=aI_{IR}(x, y)+(1-a)I_{op}(x, y)$$

The paper by Kruse (2002) shows applications of ASTER's bands other than TIR. In this research "multispectral short-wave infrared (SWIR) and long-wave-infrared (LWIR) remote sensing to map mineralogy associated with hot springs and epithermal mineral deposits were used. Selected sites around the world covering a range of active/inactive hot springs and deposit types are being studied using the MODIS/ASTER airborne simulator (MASTER) and the Advanced Spaceborne Thermal Emission and Reflection Radiometer (ASTER). MASTER and ASTER data analysis contribute to mineral mapping in the VNIR/SWIR, however, their main contribution is improved mapping of siliceous sinter utilizing LWIR signatures. Integrated study using these VNIR/SWIR/LWIR remote sensing datasets is said to be in progress. SWIR spectral signatures and mineral maps derived from MASTER and ASTER data generally agree with those extracted from higher spectral resolution hyperspectral data, thus validating the multispectral instruments' performances. Analysis of the SWIR MASTER/ASTER data allow mapping of characteristic minerals associated with hot springs/mineral deposits, including carbonates, kaolinite, alunite, buddingtonite, muscovite, and hydrothermal silica. Mineral identification and distribution was verified utilizing ground spectral measurements and mineral maps produced from AVIRIS hyperspectral data. LWIR spectral signatures principally allowed improved mapping of the distribution of siliceous sinter associated with these deposits. Integrated analysis of the MASTER/ASTER data using both the SWIR and LWIR spectral data is in progress with the goal of refining maps showing the distribution of key minerals associated with active and fossil hot springs and epithermal mineral deposits."

Aiazzi, et al (2005) states “image fusion aims at the exploitation of the information conveyed by data acquired by different imaging sensors. A notable application is merging images acquired from space by panchromatic and multi- or hyper-spectral sensors that exhibit complementary spatial and spectral resolution. Multiresolution analysis has been recognized efficient for image fusion. The Generalized Laplacian Pyramid (GLP), in particular, has been proven to be the most efficient scheme due to its capability of managing images whose scale ratios are fractional numbers (non-dyadic data) and to its simple and easy implementation. Data merge based on multiresolution analysis, however, requires the definition of a model establishing how the missing spatial details to be injected into the multispectral bands are extracted from the panchromatic image. The model can be global over the whole image or depend on the local space-spectral context. Each of the five thermal infrared (TIR) images of ASTER (90m) is merged with the most correlated visible-near infrared (VNIR) image (15m). Due to the 6:1 scale ratio, the GLP has been utilized. The injection of spatial details has been ruled by means of the Spectral Distortion Minimizing (SDM) model that minimises the spectral distortion between the resampled and fused images. Notwithstanding the lack of a spectral overlap between the VNIR and the TIR bands, experimental results show that the fused images keep their spectral characteristics while the spatial resolution is enhanced. The GLP scheme demonstrated its capability to merge images at any rational scale ratio, thus being superior to any dyadic wavelet scheme. In the case of 6:1 ASTER VNIR-TIR image fusion only the composition of two cascaded filters is needed for reduction and expansion. In addition, the adoption of the SDM injection model guarantees that the fused images have no spectral distortion with respect to the simply expanded images. This property can be particularly useful when, as in the ASTER case, no spectral overlap exists between the images that are to be merged. The analysis of correlation between bands is useful to find out the most suitable band from which to extract the spatial details to be injected.”

Jiménez-Muñoz and Sobrino (2007) in their paper show an application of ASTER TIR bands and present the important concept of thermal imaging, which is retrieving land-surface temperature. In the paper it is explained that “ASTER provides the user community with standard products of land-surface temperature (LST) and emissivity using the temperature and emissivity separation (TES) algorithm. This letter analyses the feasibility of using two-channel (TC) algorithms for LST retrieval from ASTER data, which could be considered as an alternative or complementary procedure to the TES algorithm. TC algorithms have been developed for all the ASTER thermal infrared bands combinations, and they have been applied to six ASTER images acquired over an agricultural area of Spain in 2000, 2001, and 2004. LST values obtained with TC algorithms were compared with the TES product. In addition, the TC algorithms were tested using simulated data and ground-based measurements collected coincident with the ASTER acquisition in 2004. The results show that TC algorithms provide similar accuracies than the TES algorithm (~1.5 K), with the main advantage that the atmospheric correction is included in the algorithm itself.”

Strait, et al (2008), discussed pansharpening combinations of a low-resolution colour multispectral image with a high-resolution greyscale panchromatic image to create a high-resolution fused colour image. This paper is important in the fact that it shows how comparisons are made among image fusion techniques and how their relative success is evaluated. In this paper they examine five different pan-sharpening methods: IHS, PCA, Wavelet fusion, P+XS, and variational wavelet pan-sharpening (VWP) and evaluate their effectiveness. Additionally, they propose an extension to the IHS pan-sharpening method to

improve the resulting spectral quality. In order to compare the method results spatial and spectral qualities are evaluated by relying on both visual inspection and metric performance data. The results indicate that VWP is most effective in preserving spectral data, while IHS methods produce images with the best spatial quality. In comparing the spatial quality, as mentioned before, it is relatively easy to judge spatial quality just by looking at the image. For example, IHS and PCA demonstrate clear edges whereas Wavelet experiences what is called a stair-casing effect. Similarly for all the other images this pattern follows. In the results of the spatial metrics, it confirms the prediction that IHS and PCA have the highest spatial quality, but it misleads the reader in evaluating P+XS and Wavelet. P+XS have a lower spatial evaluation value than Wavelet, yet P+XS visually look better. Overall, from the average of the results of the six images; it is clear the IHS and PCA spatially perform best outputs. The spectral quality was more difficult to judge visually; therefore many metrics were used in order to evaluate the results. In all the fused images, IHS and PCA have the highest colour distortion. This is due to overusing the panchromatic image. The colours visually look very different that the original MS. It is difficult to say which of the other images match better to the MS. The metrics were run on all the images and an average of the results was taken. Looking at the results it can be concluded from the metrics that VWP performs best spectrally. In comparing the three IHS methods only, the metrics conclude the original IHS performs best spatially whereas the Adaptive IHS performs best spectrally. In conclusion, overall the VWP performs best spectrally and the IHS performs best spatially. There is always a trade off in spectral and spatial quality, because of this the choice of method can depend on the how the fused image will be used. Also given the metric results, it was concluded that among the three different IHS methods, the Adaptive IHS performs best spectrally.

Li and Yang, (2011), deals with “the remote sensing image pansharpening problem from the perspective of compressed sensing (CS) theory which ensures that with the sparsity regularization, a compressible signal can be correctly recovered from the global linear sampled data. First, the degradation model from a high to low-resolution multispectral (MS) image and high-resolution panchromatic (PAN) image is constructed as a linear sampling process which is formulated as a matrix. Then, the model matrix is considered as the measurement matrix in CS, so pan-sharpening is converted into signal restoration problem with sparsity regularization. Finally, the basis pursuit (BP) algorithm is used to resolve the restoration problem, which can recover the high-resolution MS image effectively. The QuickBird and IKONOS satellite images are used to test the proposed method. The experimental results show that the proposed method can well preserve spectral and spatial details of the source images. The pansharpened high-resolution MS image by the proposed method is claimed to be competitive or even superior to those images fused by other well-known methods. In the novel pan-sharpening method based on CS technique, based on the PAN and MS images generation model, pan-sharpening problem is referred as an ill-posed inverse problem. Then, the sparsity regularization is employed to address the ill-posed inverse problem, and the high-resolution spectral image can be effectively recovered. The method is tested on QuickBird and IKONOS images and compared with six well-known methods: 1) Generalized IHS; 2) Gram-Schmidt Transform; 3) Singular Value Thresholding; 4) Context Based Decision; 5) Additive Wavelet Based Fusion; and 6) Genetic Algorithm based methods. The spectral and spatial information are comprehensively evaluated using several image quality measures. The experimental results demonstrate the effectiveness of sparsity as a prior for satellite PAN and MS image fusion. In addition, it was noticed that the

proposed method can easily process image fusion and restoration when the source images are corrupted by noise by only adjusting the parameter ε. However, the proposed scheme takes more time than traditional methods." The way the comparison was done between different image fusion methods was the highlight of the paper. The novel fusion technique had its strengths with short comings.

Jeganathan et al (2011), not only shows the application of pansharpening thermal images of ASTER but also shows the limitations of how much the resolution can increase without giving error. According to the authors: "Fine spatial resolution (e.g., <300m) thermal data are needed regularly to characterise the temporal pattern of surface moisture status, water stress, and to forecast agriculture drought and famine. However, current optical sensors do not provide frequent thermal data at a fine spatial resolution. The TsHARP model, which is a thermal data sharpening model developed by Agam et al. (2007), provides a possibility to generate fine spatial resolution thermal data from coarse spatial resolution (≥1 km) data on the basis of an anticipated inverse linear relationship between the normalised difference vegetation index (NDVI) at fine spatial resolution and land surface temperature at coarse spatial resolution. The study utilised the TsHARP model over a mixed agricultural landscape in the northern part of India. Five variants of the model were analysed, including the original model, for their efficiency. Those five variants were the global model (original); the resolution-adjusted global model; the piecewise regression model; the stratified model; and the local model. The models were first evaluated using ASTER thermal data (90m) aggregated to the following spatial resolutions: 180 m, 270 m, 450 m, 630 m, 810m and 990 m. Although sharpening was undertaken for spatial resolutions from 990m to 90m, root mean square error (RMSE) of less than 2000 could, on average, be achieved only for 990–270m in the ASTER data. The RMSE of the sharpened images at 270 m, using ASTER data, from the global, resolution-adjusted global, piecewise regression, stratification and local models were 1.91, 1.89, 1.96, 1.91, 1.70 K, respectively. The global model, resolution adjusted global model and local model yielded higher accuracy, and were applied to sharpen MODIS thermal data (1 km) to the target spatial resolutions. Aggregated ASTER thermal data were considered as a reference at the respective target spatial resolutions to assess the prediction results from MODIS data. The RMSE of the predicted sharpened image from MODIS using the global, resolution-adjusted global and local models at 250m were 3.08, 2.92 and 1.98 K, respectively. The local model consistently led to more accurate sharpened predictions by comparison to other variants."

Al-Wassai, et al (2012), compares various image quality assessment methods with a new method. It is stated that "most important details of the image are in edges regions, but most standards of image estimation do not depend upon specifying the edges in the image and measuring their edges. However, they depend upon the general estimation or estimating the uniform region, so this study deals with new method proposed to estimate the spatial resolution by Contrast Statistical Analysis (CSA) depending upon calculating the contrast of the edge, non-edge regions and the rate for the edges regions. Specifying the edges in the image is made by using Sobel operator with different threshold values. In addition, estimating the colour distortion added by image fusion based on Histogram Analysis of the edge brightness values of all RGB-colour bands and L component. Results of the study showed the importance of proposed new CSA as a criterion to measure the quality evaluation for the spatial resolution of the fused images, in which the results showed the effectiveness of high efficiency when compared with the other criterion methods for measurement."

In Okyay (2012), ASTER thermal multispectral infrared data is evaluated in regard to lithological discrimination and mapping through emissivity values rather than conventional methods that utilize radiance values. In order to reach this goal, Principle Component Analysis (PCA) and Decorrelation Stretch techniques are utilized for ASTER VNIR and SWIR data. Furthermore, the spectral indices which directly utilize the radiance values in VNIR, SWIR and TIR are also included in the image analysis. The results show that utilizing emissivity values possesses potential for discrimination of organic matter bearing surface mixtures which has not been possible through the conventional methods. It is concluded that increased resolution is necessary for further assessment of accuracy.

1.3. Motivation

The present 90 meter resolution thermal infrared bands and the 30 meter resolution shortwave infrared (SWIR) bands of ASTER are not sufficient for detailed analysis. To improve this deficiency by the use of image fusion techniques, one possible approach is to merge product images of this band and images from higher resolution bands of ASTER such as visible and near infrared (VNIR) which has 15 meter resolution.

In the literature survey, it is seen that while traditional pan-sharpening fusing pan-chromatic images with multispectral images, only a few studies actually used thermal infrared images for this purpose. Aiazzi, et al (2005) is probably the only researcher who utilized image fusion to improve the resolution of thermal images. However, he used just one method of image fusion in his study. While, the study indicated that the potential of the approach is promising, the level of possible improvement by other methods has not yet been investigated. The proposed present thesis study, therefore, aims to use other image fusion methods to determine the limits of improvement possible. It is hoped to reach a definite conclusion as to the best method(s) for increasing spatial resolution of the ASTER infrared bands without losing spectral information.

1.4. Organization of the Thesis

This thesis includes seven chapters and the contents of the chapters are as follows: Chapter 1 defines the purpose and scope of the thesis; Chapter 2 includes information on ASTER, the data used, and the location and geology of the study area; Chapter 3 covers the background information about fundamentals of image fusion, use of objective evaluation methods; Chapter 4 is where the GUI is presented; Chapter 5 gives the results of the image analyses; Chapter 6 has detailed case studies on portions of the study area; and finally Chapter 7 includes the discussion, conclusion, limitations, and recommendations for future work.

CHAPTER 2

STUDY AREA AND DATA

2.1. Basic Information on ASTER

ASTER (Advanced Spaceborne Thermal Emission and Reflection Radiometer) is a satellite launched in December 1999 as part of NASA's Earth Observing System (EOS). ASTER is developed by NASA, Japan's Ministry of Economy, Trade and Industry (METI) and Japan's Earth Remote Sensing Data Analysis Centre (ERSDAC). ASTER has been providing maps of land surface temperature, reflectance, and elevation. As one of the EOS platforms ASTER is also part of NASA's Science Mission Directorate and the Earth-Sun System. Its goal is to observe, understand, and model the Earth system to discover how it is changing, to better predict change, and to understand the consequences for life on Earth (ASTER Mission, 2004).

ASTER captures data in 14 bands, from the visible to the thermal infrared wavelengths and provides stereo viewing capability for digital elevation model creation. ASTER data are used by other instruments for validation and calibration. Information on the detailed specifications of the 14 bands is presented in Table 1 (ASTER Mission, 2004).

Table 1 Detailed specifications of ASTER (ASTER Mission, 2004)

Band	Label	Wavelength (μm)	Resolution (m)	Nadir or Backward	Description
B1	VNIR_Band1	0.520-0.600	15	Nadir	Visible green/yellow
B2	VNIR_Band2	0.630-0.690	15	Nadir	Visible red
B3	VNIR_Band3N	0.760-0.860	15	Nadir	Near infrared
B4	VNIR_Band3B	0.760-0.860	15	Backward	
B5	SWIR_Band4	1.600-1.700	30	Nadir	Short-wave infrared
B6	SWIR_Band5	2.145-2.185	30	Nadir	
B7	SWIR_Band6	2.185-2.225	30	Nadir	
B8	SWIR_Band7	2.235-2.285	30	Nadir	
B9	SWIR_Band8	2.295-2.365	30	Nadir	
B10	SWIR_Band9	2.360-2.430	30	Nadir	
B11	TIR_Band10	8.125-8.475	90	Nadir	Long-wave infrared or thermal IR
B12	TIR_Band11	8.475-8.825	90	Nadir	
B13	TIR_Band12	8.925-9.275	90	Nadir	
B14	TIR_Band13	10.250-10.950	90	Nadir	
B15	TIR_Band14	10.950-11.650	90	Nadir	

2.2. ASTER Data Specifications

ASTER is one of five remote sensor devices on board Terra satellite. It has been collecting data in all 14 bands since February, 2000. Due to operational problems of SWIR detector cooler system starting in 2007, data quality degraded. Since May 2008, the ASTER SWIR data were not of adequate data quality. From March 13th, 2010 SWIR detectors are not providing data (ASTER GDS, 2010).

ASTER provides data in Visible and Near Infrared (VNIR), Short Wave Infrared (SWIR) and Thermal Infrared (TIR) subsystems with 14 bands. The VNIR subsystem has 3 bands. It also includes an additional back-looking near-infrared band which provides stereoscopic capability. The SWIR and TIR subsystems have 6 and 5 bands, respectively. The spatial resolutions of the subsystems are 15m in VNIR, 30m in SWIR, and 90m in TIR bands. Every ASTER scene covers an area of 60x60 km. (ASTER Mission, 2004).

The Terra satellite system on which ASTER is boarded is a sun-synchronous satellite that follows a circular, near-polar orbit at an altitude of 705 km. The equatorial crossing of the satellite is at 10:30 a.m. local time and the satellite returns to the same orbit every 16 days.

Throughout the study ASTER image with granule ID of AST3A1 0507270844010603311228 is utilized. ASTER Level-3 data is the orthorectified image product which includes Level-1B radiometrically and geometrically calibrated radiance for every bands including Band3B. Therefore no further geometric correction has been done. Detailed information about the utilized ASTER image is presented in Table 2.

Table 2 Detailed information on the ASTER image

Granule ID	AST3A1 0507270844010603311228
Processing Level	3
Acquisition Date	Nov 17, 2002
Source Data Product	ASTL1A 0211170839210212050221
Scene Center	40° 27' 26.6979" N, 33° 44' 8.6532" E
North Latitude	40° 47' 13.0372" N
South Latitude	40° 07' 34.2937" N
West Longitude	33° 17' 13.0070" E
East Longitude	34° 11' 19.9205" E
Map Projection	Universal Transverse Mercator
UTM Zone	36 N

2.3. Location of Study Area

The study area is located within the Çankırı Basin in northern central Anatolia, Figure 1. The boundaries of the study area is determined by the area covered in the ASTER data that includes Çankırı and Eldivan settlements in the west, Korgun at northwest, Tatlıpınar in the northeast; Dedeköy village in the center, Boyacıoğlu to the east, and Sulakyurt in the south.

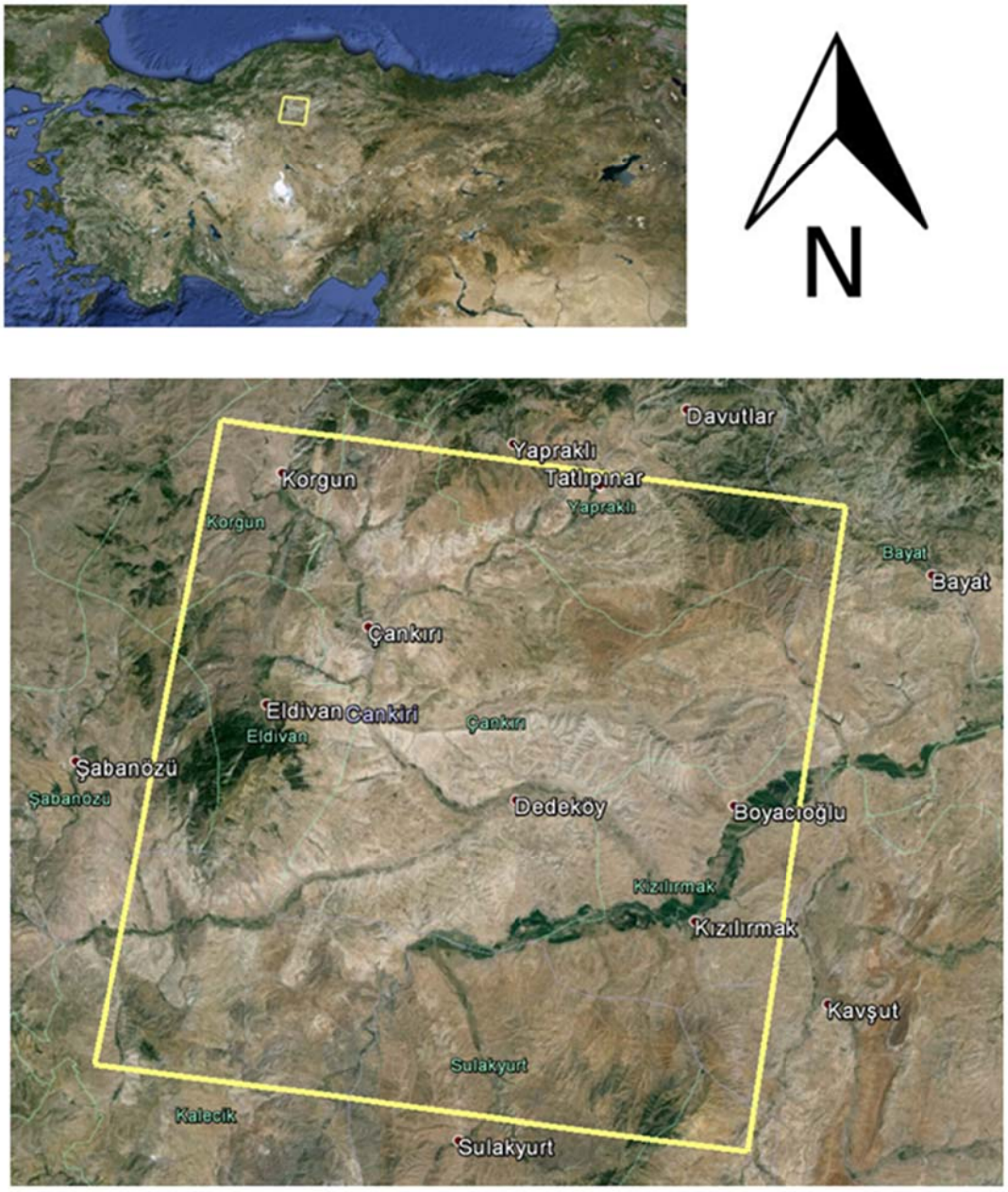

Figure 1 Location of the study area.

2.4. Geology of the Study Area

The Çankırı Basin which contains the study area is located within the İzmir–Ankara–Erzincan Suture Zone. The basement of the basin is covered by the North Anatolian Ophiolitic Melange (NAOM) and the Sulakyurt Granitoid. It is underlain by an upper Cretaceous ophiolitic melange and granitoids of the Kırşehir block. Isolated outcrops of ophiolite-related rocks with pelagic limestones, radiolarites and sheeted dyke complexes, intruded by the granitoids, are present in the southern part of the basin. (Kaymakçı, 2000).

Within the majority of the study area are Deyim, Bozkır, Süleymanlı, Tuğlu, Çandır, and İncik formations along with NAOM as shown in Figure 2. There are also small areas that contain Paleocene-Eocene units, Upper Cretaceous units, and Sulakyurt Granitoids. The major formations' lithology is briefly explained below as given by Kaymakçı (2000) and Kaymakçı, et al (2001).

"North Anatolian Ophiolitic Melange (NAOM): Lithologically, the NAOM is composed of a tectonic mixture mainly of spilites, pillow lavas, diabase dykes, red to purple radiolarian chert, cherty limestone, reddish pelagic mudstone and various serpentinized ultramafic rocks including peridotites, harzburgites and pyroxenites. The NAOM also includes layered gabbros, plagiogranites and various limestones derived from nearby platforms during accretion.

İncik Formation: The İncik formation is the most widespread and voluminous unit of the Çankırı Basin. The formation is characterized by alternation of very thick bedded red conglomerates with very thick bedded red sandstones and purple to brick red thick to very thick bedded mudstones in the northern and south-western parts of the basin; by creamy white gypsum which laterally and vertically grades into green shale in the eastern part of the basin. Higher up in the eastern part, the formation is characterized by an alternation of brick red to purple sandstones, siltstones, shale and greenish gray to bluish shale and very thick bedded red to orange gypsum layers.

Çandır Formation: The formation is characterized by an alternation of red to pink, buff to creamy white pebbly mudstone, clayey limestone, siltstone, matrix supported conglomerate intercalated with white limy-marl, thin silty-limestone, oolite bearing limestone, clayey limestone and very thin organic rich layers at the bottom; alternation of red to pink sandy-silty mudstone, loose matrix supported conglomerates, clayey sandstone, siltstone intercalated with caliche limestone, paleosol layers with carbonate concretions and cross bedded sandstone and conglomerates locally discordant with these layers in the middle; and pink sandy, limy-concretion bearing mudstone, clayey porous limestone, siltstone, silty-limestone, white to creamy white marl, greenish shale alternations and clayey, pebbly sandstone intercalations at the top.

Tuğlu Formation: The formation is characterized by dark gray shale, mudstone, siltstone and sandstone alternations at the bottom; alternation of green, pelecypoda bearing stiff bentonitic claystone and dark green to gray organic rich mudstone, intercalated with cherty limestone beds and lenses of conglomerate along with very thin coal seams in the middle; and at the top it gradually becomes marl dominated and grades laterally into alternation of thick-bedded white gypsum and thick bedded yellow to pinkish silty mudstone.

Süleymanlı Formation: The formation is characterized mainly by an alternation of thin bedded red to buff, brick red mudstone, grey marl with small gastropod fragments, buff laminated mudstone, thin bedded siltstone, silty and sandy mudstone alternation while at the bottom the formation is dominated by conglomerates along western margin of the Çankırı Basin and at the top it becomes finer and more shale-mud dominated into the centre of the basin.

Bozkır Formation: The formation is mainly characterized by alternation of gypsum with marls and thin bedded sandstones while the dominant lithology is white to pale grey gypsum.

Deyim Formation: The Deyim Formation is characterized mainly by variable sized, poorly sorted, polygenic loose conglomerates/gravel and sandstone (loosely compacted coarse clastics) with intercalation of minor fine clastics."

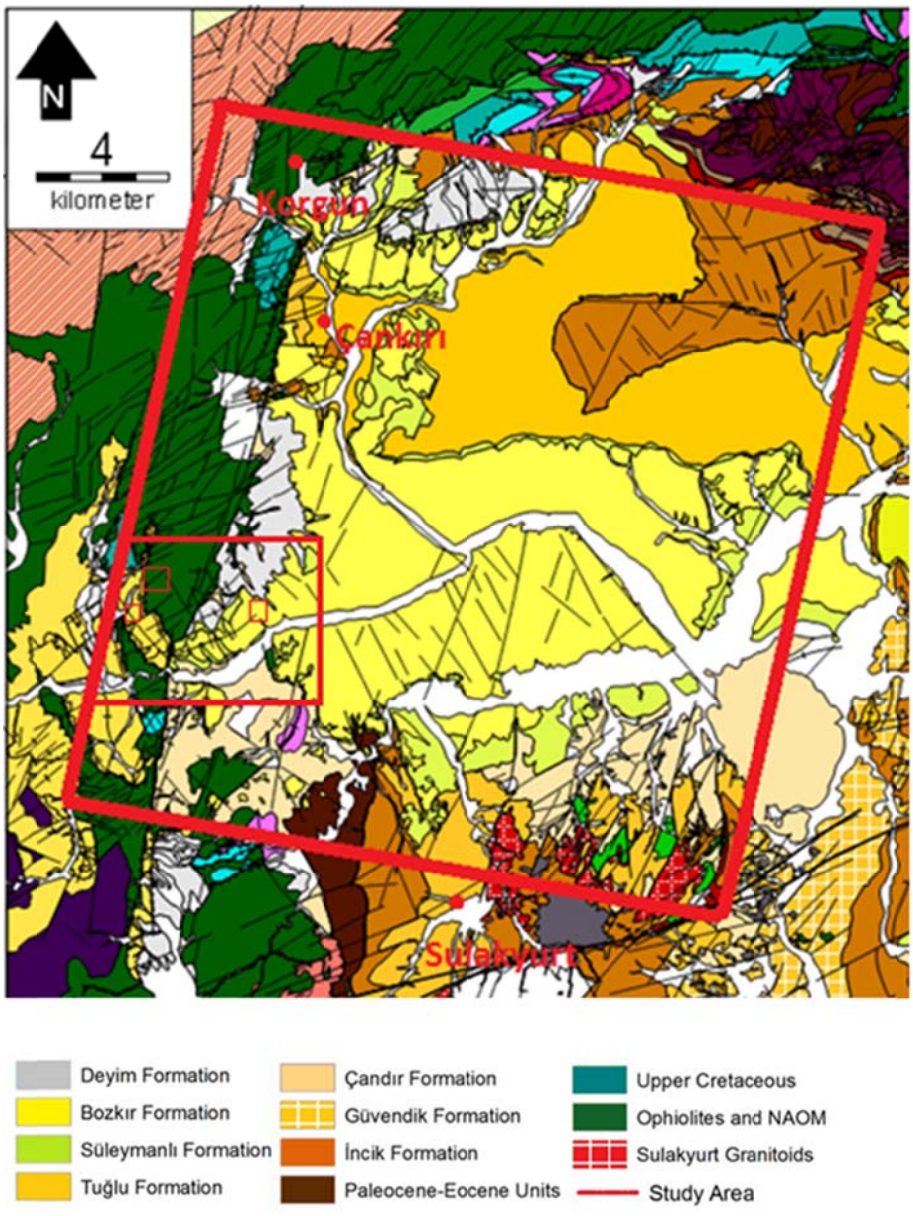

Figure 2 Geological map of the Çankırı Basin (Kaymakçı, 2000) with study area and case study areas displayed on it.

CHAPTER 3

METHODOLOGY

3.1. Fundamentals of Image Fusion

In image fusion applications, best quality information from two or more images are gathered and combined in a single fused image which has reduced shortcomings of original images. This single image will provide more information than the original images. A general illustration of the ideal concept is given in Figure 3 (Güngör, 2008).

In remote sensing applications, the increasing availability of space borne sensors which have different capabilities has led to development of different image fusion algorithms. Most applications of image processing require high spatial and high spectral resolution in the fused image. Available data from different sensors are not of the same specifications and as such cannot provide such high resolution data. In image fusion images from different information sources can be used. The fused image are likely to have combinations of spatial and spectral resolution characteristics, therefore possible adverse effect of distorting the spatial and/or spectral information of the MS data may occur during fusion.

In the majority of the earth observation satellite products, two types of images are available. The panchromatic or any monochromatic image acquired by satellites have maximum resolution available and the multispectral images will be of coarser resolution, two or four times lower. The multispectral data by definition has a finer spectral resolution than that of monochromatic high spatial resolution image. The process of image fusion involves the merging of the high resolution image with the multispectral data to convey more information.

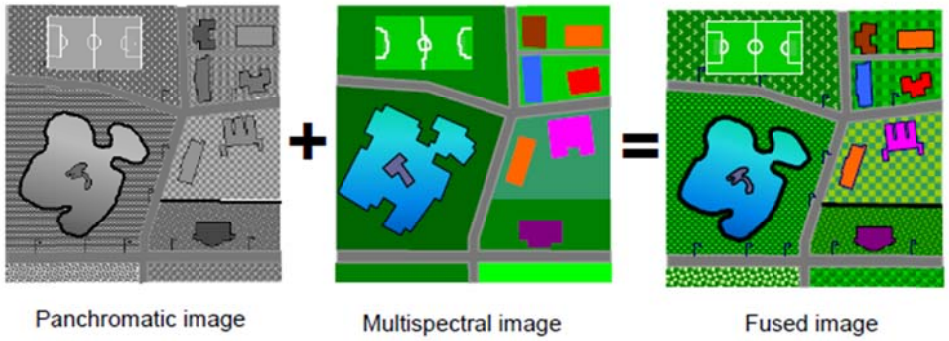

Figure 3 General example of image fusion (Güngör, 2008)

Several methods have been proposed in literature for merging satellite images. Image fusion methods can be broadly classified into two as transform domain fusion and spatial domain fusion.

Transform Domain Fusion: In transform domain fusion methods the input images are first transformed then fused and the result is converted back by an inverse transform. In these methods the fusing coefficients are calculated with fusion rules which are either pixel based or region based (Oudre, 2007).

Spatial Domain Fusion: In spatial domain fusion input images are worked on directly. Weights are estimated for each input image and for each pixel with iterative methods which optimize a cost function (Oudre, 2007).

The fusion methods such as averaging, Brovey Transformation (BT) (Al-Wassai, et al, 2011), principal component analysis (PCA) (Canga, 2002), and Intensity-Hue-Saturation IHS based methods (Tu, et al, 2001) fall under spatial domain approaches.

Another important spatial domain fusion method is the high pass filtering based technique. Here the high frequency details are injected into up-sampled version of MS images. The disadvantage of spatial domain approaches is that they produce spatial distortion in the fused image. Spectral distortion becomes a negative factor while we go for further processing, such as classification problem.

Spatial distortion can be handled by transform domain approaches on image fusion. Some other transform domain fusion methods have also been developed, such as Laplacian pyramid based, curvelet transform based, etc. These methods show a better performance in spatial and spectral quality of the fused image compared to other spatial methods of fusion.

The images to be used in image fusion should be registered before the process and misregistration is a major source of error in image fusion. The most commonly used image fusion methods are listed below and will be described together with their basic formulation in the following sections.

- IHS transform based image fusion,
- Brovey Transform (BT),
- Wavelet transform image fusion (WT),
- Principal component analysis (PCA) based image fusion,

3.1.1. Intensity-Hue-Saturation (IHS) Transformation

The original RGB colour space is not sufficient for image fusion process since the correlation of the image channels is not clearly presented. IHS gives the opportunity of displaying separate channels with certain colour properties, namely intensity (I), hue (H), and saturation (S). Intensity, vector 1 (v1), and vector 2 (v2) can be obtained from the RGB values of each pixel, with coefficients related to image cube geometry (Tu, et al, 2001).

$$\begin{bmatrix} I \\ v1 \\ v2 \end{bmatrix} = \begin{bmatrix} \frac{1}{3} & \frac{1}{3} & \frac{1}{3} \\ \frac{-\sqrt{2}}{6} & \frac{-\sqrt{2}}{6} & \frac{2\sqrt{2}}{6} \\ \frac{1}{\sqrt{2}} & -\frac{1}{\sqrt{2}} & 0 \end{bmatrix} \begin{bmatrix} R \\ G \\ B \end{bmatrix}$$

The intensity I describes the total colour brightness and exhibits as the dominant component, a strong similarity to the more highly resolved panchromatic image. Therefore, the intensity of the MS image pixel is replaced by the intensity of the corresponding pixel of high-resolution (Panchromatic) data and then the merged result is converted back into the RGB space.

$$\begin{bmatrix} R \\ G \\ B \end{bmatrix} = \begin{bmatrix} 1 & -\frac{1}{\sqrt{2}} & \frac{1}{\sqrt{2}} \\ 1 & -\frac{1}{\sqrt{2}} & -\frac{1}{\sqrt{2}} \\ 1 & \sqrt{2} & 0 \end{bmatrix} \begin{bmatrix} I_{pan} \\ v1 \\ v2 \end{bmatrix}$$

This transformation may involve a large number of calculations. To reduce calculation time, a new algorithm involving only summation and subtractions is proposed (Tu, et al, 2001).

$$\begin{bmatrix} R \\ G \\ B \end{bmatrix} = \begin{bmatrix} 1 & -\frac{1}{\sqrt{2}} & \frac{1}{\sqrt{2}} \\ 1 & -\frac{1}{\sqrt{2}} & -\frac{1}{\sqrt{2}} \\ 1 & \sqrt{2} & 0 \end{bmatrix} \begin{bmatrix} I_{pan} \\ v1 \\ v2 \end{bmatrix}$$

$$= \begin{bmatrix} 1 & -\frac{1}{\sqrt{2}} & \frac{1}{\sqrt{2}} \\ 1 & -\frac{1}{\sqrt{2}} & -\frac{1}{\sqrt{2}} \\ 1 & \sqrt{2} & 0 \end{bmatrix} \begin{bmatrix} I + (I_{pan} - I) \\ v1 \\ v2 \end{bmatrix} = \begin{bmatrix} R + (I_{pan} - I) \\ G + (I_{pan} - I) \\ B + (I_{pan} - I) \end{bmatrix}$$

An example application for the use of IHS fusion is given in Figure 4.

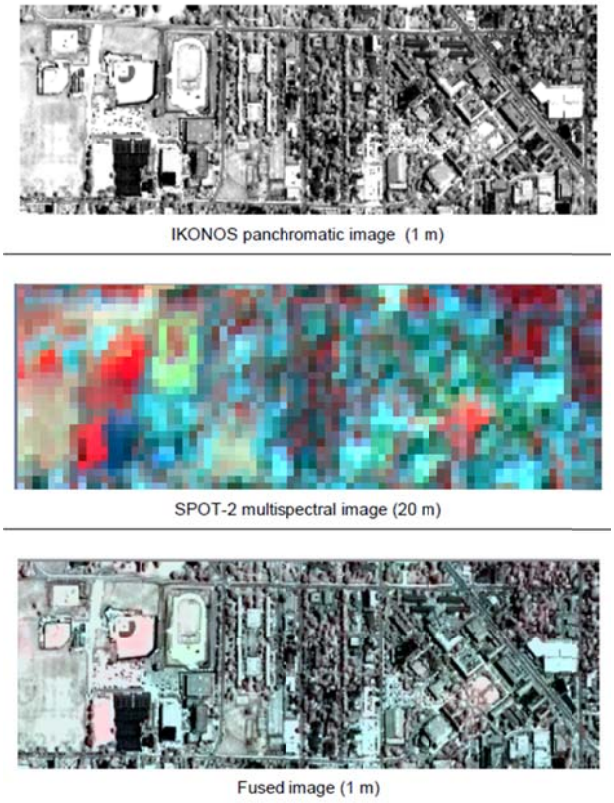

Figure 4 Classical IHS Fusion of IKONOS Panchromatic and SPOT-2 (Güngör, 2008)

Classical IHS method suffers from colour distortion because of the limitation that the method can fuse only three multispectral bands even if the multispectral image has more than three bands. The different band combinations result in fused products with different qualities, which in turn make the classical IHS method inconsistent. The reason of this inconsistency and the colour distortion stems from discarding some of the bands from the intensity calculation (Tu, et al, 2001).

Every different band combination gives a different detail image since the detail image is obtained as the difference of the panchromatic and the intensity images, and the quality of the fused image depends on this detail image. To overcome the limitations of the classical IHS method, the generalized IHS approach which enables fusion of more than three multispectral bands is used. The generalized IHS method is designed to use all available bands to calculate the overall intensity. For this reason, the detail image to be added to each multispectral band is calculated by the contribution of all available bands (Tu, et al, 2001).

$$\begin{bmatrix} R_{\text{new}} \\ G_{\text{new}} \\ B_{\text{new}} \end{bmatrix} = \begin{bmatrix} 1 & -1/\sqrt{2} & 1/\sqrt{2} \\ 1 & -1/\sqrt{2} & -1/\sqrt{2} \\ 1 & \sqrt{2} & 0 \end{bmatrix} \begin{bmatrix} I_0 + (I_{\text{new}} - I_0) \\ v1_0 \\ v2_0 \end{bmatrix}$$

$$= \begin{bmatrix} 1 & -1/\sqrt{2} & 1/\sqrt{2} \\ 1 & -1/\sqrt{2} & -1/\sqrt{2} \\ 1 & \sqrt{2} & 0 \end{bmatrix} \begin{bmatrix} I_0 + \delta \\ v1_0 \\ v2_0 \end{bmatrix}$$

$$= \begin{bmatrix} R_0 + \delta \\ G_0 + \delta \\ B_0 + \delta \end{bmatrix}$$

Fusion results show that the generalized IHS method reduces the colour worsening effect and resolves the inconsistency problem of the classical IHS method by producing more stable fusion results (Tu, et al, 2001).

3.1.2. Brovey Transform

The Brovey Transform (BT) uses ratios to sharpen MS images. As BT was formulated to produce RGB images, the formulation is limited to only three bands (Al-Wassai, et al, 2011).

The basic idea for BT stems from the desire to use the four basic arithmetic operations. Practically all combinations of arithmetic operations including addition, multiplication, normalized division, ratios, and subtraction have been employed in the fusion of MS and PAN images. These arithmetic operations are applied on the MS and PAN bands which have been combined in different ways to achieve a better fusion effect (Al-Wassai, et al, 2011). These models assume that there is high correlation between the PAN and each of the MS bands. Some of the popular arithmetic combination methods for pansharpening are the Brovey Transform, Colour Normalized Transformation, and Multiplicative Method.

Of the four possible arithmetic methods only the multiplication is unlikely to distort the colours by transforming an intensity image into a panchromatic image. In the multiplicative method, each pixel in each band k of MS data is multiplied by the corresponding pixel of the PAN data. To eliminate the increased brightness, the square root of the resulting data set is taken. The square root of the multiplicative data set reflects the mixed spectral properties of both sets. The fusion algorithm formula is as follows.

$$F_{k(i,j)} = \sqrt{M_{k(i,j)} P_{(i,j)}}$$

Therefore this algorithm is a simple multiplication of each multispectral band with the panchromatic image. The advantage of the algorithm is that it is straightforward and simple. By multiplying the same information into all bands, however, it creates spectral bands of a higher correlation which means that it does alter the spectral characteristics of the original image data.

This method is computationally simple; it is generally the fastest method and requires the least system resources. However, the resulting merged image does not retain the spectral characteristics of the input multispectral image fully. The intensity component is increased, making this technique good for highlighting urban features which tend to be higher reflecting components in a visible/near infrared image (Harish, et al, 2011).

Brovey transformation is basically an extension of the multiplicative method. The extension consists of normalizing the MS pixel data by dividing each value by the average pixel value of the three MS bands. The following equation gives the mathematical formula for the BT:

$$F_{k(i,j)} = \frac{M_{k(i,j)} P_{(i,j)}}{\sum_{k} M_{k(i,j)}} \qquad k=1, 2, 3; \qquad i=1, 2, \ldots, m; \qquad j=1,2, \ldots, n$$

In this equation k indicates the MS band, and i and j indicate the pixel of interest. It is based on the assumption that the spectral range of the panchromatic image is same as that covered by multispectral bands. The BT may cause colour distortion if the spectral range of the high resolution image is different from the spectral range covered by the MS bands.

An application of Brovey Fusion is illustrated in Figure 5.

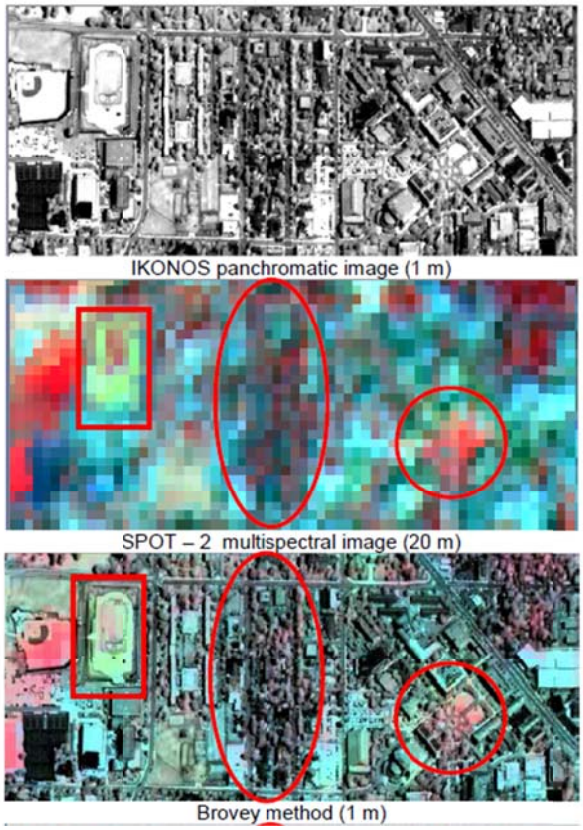

Figure 5 Brovey Fusion of IKONOS Panchromatic and SPOT-2 (Güngör, 2008).

3.1.3. Wavelet Transform Fusion

The most common form of transform image fusion is the wavelet transform fusion. In common with all transform domain fusion techniques the transformed images are combined in the transform domain using a defined fusion rule, then transformed back to the spatial domain to give the resulting fused image (Nicolov, et al, 2000). The process is illustrated in Figure 6. Wavelet transform fusion is more formally defined by considering the wavelet transforms ω of the two registered input images $I_1(x, y)$ and $I_2(x, y)$ together with the fusion rule ϕ. Then, the inverse wavelet transform ω^{-1} is computed, and the fused image I(x, y) is reconstructed:

$$I(x, y) = \omega^{-1}(\phi(\omega(I_1(x, y)), \omega(I_2(x, y))))$$

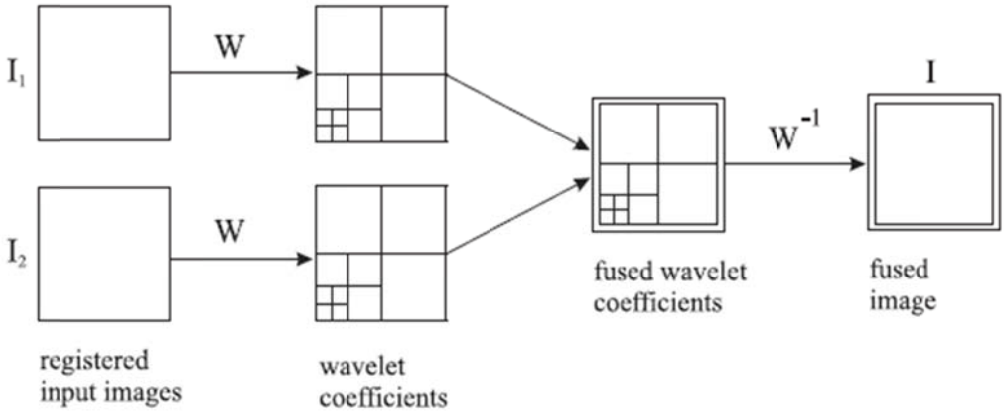

Figure 6 Fusion of the wavelet transforms of two images (Nicolov, et al, 2000)

There are many combinations of different decomposition levels and fusion rules such as maximum, minimum, multiplication, addition, geometric averaging. The possibilities display wavelet transform's flexibility in image fusion. Specialized fusion rules can also be developed to get better results on specific images. However it is not possible to display every possible option in wavelet image fusion.

For the sake of simplicity in this study the decomposition level of wavelet transformation is selected as the maximum of the program being used, which is level five. The fusion rule was selected to be averaging, since other fusion rules available in MATLAB wavelet tool were too close to image fusion methods discussed in this chapter.

3.1.4. Principal Component Analysis

The PCA is a mathematical procedure that uses an orthogonal transformation to convert a set of observations of possibly correlated variables into a set of values of linearly uncorrelated variables called principal components. It computes a compact and optimal description of the data set. The first principal component accounts for as much of the variance as possible. First principle component is taken to be along the direction with the maximum variance. The second principle component is constrained to lie in the subspace orthogonal to the first. Within this subspace, third component points the direction of maximum variance direction in the subspace perpendicular to the first two and so on (Kumar, 2009).

The PCA is also called as Karhunen-Loéve transform or the Hotelling transform. The PCA does not have a fixed set of basis vectors like Fast Fourier Transform (FFT), Discrete Cosine Transform (DCT) and wavelet, etc.; its basis vectors depend on data set. The eigenvectors and eigenvalue of covariance matrix are computed and then sorted by decreasing eigenvalue. The first column of eigenvector (V), which corresponds to larger eigenvalue, is considered to compute P_1 and P_2 as

$$P_1 = \frac{V(1)}{\sum V} \qquad \text{and} \qquad P_2 = \frac{V(2)}{\sum V}$$

The information flow diagram of PCA-based image fusion algorithm is shown in Figure 7 below. The input images (images to be fused) $I_1(x, y)$ and $I_2(x, y)$ are arranged in two column vectors and their empirical means are subtracted. The resulting vector has a dimension of n x 2, where n is length of the each image vector. Compute the eigenvector and eigenvalues for this resulting vector are computed and the eigenvectors corresponding to the larger eigenvalue obtained. The normalized components P_1 and P_2 (i.e., $P_1+P_2=1$) using third equation are computed from the obtained eigenvector. The fused image is:

$$I_f(x, y)=P_1I_1(x, y)+P_2I_2(x, y)$$

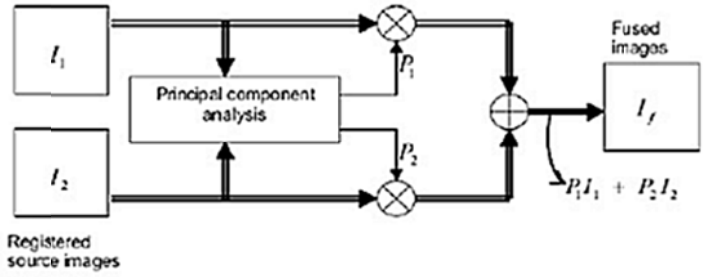

Figure 7 Information flow diagram in image fusion scheme using PCA. (Kumar, 2009)

PCA method is data dependent. The size of the input images affects the fusion results. Moreover, the correlation among the high spatial resolution and the first principal component of the higher spectral resolution image also affect the performance of the method. If the correlations are higher, better fused images are obtained. On the other hand, if the correlations are lower, the fused results may not be satisfactory both in terms of colour and spatial detail content. The linear regression method is successful in preserving the colour content of the original multispectral image; however, it produces spatial artifacts which deteriorate the performance of this method in terms of spatial detail transfer from the panchromatic image. The reason of being not successful is using the same weighting coefficients for the pixels covered by the local window. This problem gets worse when images from different sensors are fused (Kumar, 2009).

3.2. Objective Evaluation of Image Fusion

In the reference by Malviya and Bhirud (2010), it is argued that "the general requirements of an image fusion process are that it should preserve all valid and useful pattern information from the source images, while at the same time not introducing artifacts that could interfere with subsequent analysis. However it is not possible to combine images without introducing some form of distortion. As the image fusion technologies have been developing quickly in a number of applications such as remote sensing, medical imaging, machine vision, and military applications in recent years, the methods that can assess or evaluate the performances of different fusion technologies have been recognized as an urgent requirement."

The evaluation procedures are based on the verification of the preservation of spectral characteristics and the improvement of the spatial resolution. In practice, the most common way of evaluating the relative success of image fusion is based on subjective image viewing tests. Comparative evaluation by human visual inspection in image fusion is used to assess the relative fusion performance of different fusion schemes. The visual appearance may be subjective and depends on the human interpreter, but the power of the visual cognition as a final backdrop cannot be underestimated (Klonus-Ehlers, 2009).

Even though the human visual system is still the most complex and able tool, in certain cases it may be inadequate for the evaluation and comparison of image fusion experiments. Therefore, a number of statistical evaluation methods are used to measure the evaluation of fusion performance. In devising objective measures for the performance of image fusion methods, two points should be emphasized: fusion quality and computational complexity. These methods have to be objective, reproducible, and of quantitative nature. Although there have been many attempts, as yet no universally accepted standard has emerged for evaluating image fusion performance.

The following sections explain in detail selected spectral and spatial evaluation methods. There are many methods in the literature; however, they all seem to result in similar results without any one of them providing a more decisive conclusion compared to the others. Therefore, in this study only the most basic and widespread objective evaluation methods were implemented.

3.2.1. Spectral Evaluation

A number of statistical evaluation methods are used to measure after-fusion colour fidelity. The most commonly used measures selected for the study to compare the performance of image fusion methods are introduced in the following sections.

3.2.1.1. The Correlation Coefficient (CC)

The main objective of image fusion applications is to preserve the maximum spatial and spectral information from the original images without changing the relationships among the original bands. Correlation coefficients are used to objectively determine the quality of the fused images. The value of CC ranges from -1 to 1. The higher the correlation coefficient value, the higher the quality of spectral information in the fused image compared with the original MS image.

Correlation coefficient represents the overall quality of the fused image. Certain features can give a better response to the fusion algorithm implemented. Therefore, fusion quality will depend on the size of the window used. For this reason, it is suggested to calculate the correlation coefficient for a small window instead of the entire image (Klonus-Ehlers, 2009). Formula for CC is below, where r is the correlation coefficient, I_r is the intensity value of reference image and I_f is the intensity value of fused image, and sI is standard deviation of the image.

$$r = \frac{1}{n-1}\sum_{i=1}^{n}\left(\frac{I_{ri}-\overline{I}_r}{sI_r}\right)\left(\frac{I_{fi}-\overline{I}_f}{sI_f}\right), \qquad sI = \sqrt{\frac{1}{n}\sum_{i=1}^{n}(I_i-\overline{I})^2}$$

3.2.1.2. Root Mean Squared Error (RMSE)

The root mean squared error (RMSE) displays spectral distortion of the fused band when compared with the original low spatial resolution data. It is computed by the difference of the standard deviation and the mean of the fused and the original image. The best possible value is again 0.

$$RMSE = \sqrt{\frac{1}{MN}\sum_{i=1}^{M}\sum_{j=1}^{N}(I_r(i,j)-I_f(i,j))^2}$$

In the above equation, M and N are matrix sizes for the reference and fused images, respectively (Malviya and Bhirud, 2010).

3.2.1.3. Relative Global Dimensional Synthesis Error (ERGAS)

The formula for Relative Global Dimensional Synthesis Error (French name acronym: ERGAS) in fusion is as follows:

$$ERGAS = 100\frac{h}{\ell}\sqrt{\frac{1}{n}\sum_{i=1}^{n}\frac{RMSE_i^2}{MR_i^2}}$$

where MR_i is the mean radiance of the i^{th} MS band, h is the spatial resolution of the high resolution image, ℓ is the spatial resolution of the low resolution image. ERGAS offers a global depiction of the quality of radiometric distortion of the fused product.

The lower the value of the RMSE index and the ERGAS index, the higher the spectral quality of the fused images (Klonus-Ehlers, 2009).

The two comprehensive quality indices RMSE and ERGAS are normally employed to assess fusion algorithms by evaluating the quality of the entire synthetic images other than individual fused bands. It is worth pointing out that these indices along with the previously mentioned quality indices for individual bands, such as correlation coefficient, are scene-dependent. For a smooth scene with small diversities of spatial signals and spectral frequencies, the quality of a synthetic image will be high; with lower RMSE and ERGAS values. For a complex scene with large spatial and spectral varieties, when an identical fusion algorithm is applied to it, the case will be reversed: the quality of the resultant synthetic image will be low; the RMSE and ERGAS values will be high (Jing, 2008).

3.2.2. Spatial Improvement Evaluation

Determination of a balanced spectral characteristics preservation and spatial improvement combination is the main goal of image fusion applications. It must be noted that if no spatial improvement is obtained, spectral properties are fully preserved. It has been common in most studies to deal with spectral improvement while less attention has been paid on spatial improvement. Therefore the quantitative method named high-pass correlation coefficient (HPCC) is used to evaluate the level of improvement in spatial resolution.

The calculation of the HPCC starts with the application of a high-pass (HP) filter with a 3×3 Laplacian kernel to the high spatial resolution image, and then to each band of the fused image. Next step is the calculation of the correlation coefficients between the HP filtered bands and the HP filtered high spatial resolution images. Any HP filter can be used for this purpose.

3.3. Preprocessing

Preprocessing of ASTER images involve the calibration of ASTER VNIR, SWIR and TIR bands; recalibration of ASTER TIR bands. In this process, raw digital numbers are converted into radiance values. For this purpose, gain and offset settings of the ASTER data are obtained from the metadata file. The data used in this study have "High Gain" settings in VNIR Band 1 and Band 2, while Band 3N and Band 3B have "Normal Gain" settings. For SWIR and TIR, all the bands have "Normal Gain" settings. Unit conversion coefficients (UCC) were then selected for all 14 ASTER bands accordingly.

As explained in section "2.2. ASTER Data Specifications", ASTER TIR bands should be recalibrated in order to compensate the delay in radiometric calibration coefficient (RCC) updating.

3.3.1. Calibration of ASTER VNIR, SWIR and TIR Images

For the calibration of VNIR, SWIR and TIR images, the raw "digital number" values recorded by the sensor are converted to at-sensor radiance. For this conversion, the raw digital number is corrected for sensor gain and offset by applying the following equation.

$$L' = (DN - 1) * UCC$$

where
L' at-sensor radiance,
DN digital number in the original ASTER image;
UCC unit conversion coefficient

The unit conversion coefficients depend on the gain setting of the band, which was used during image acquisition, as well as on the band of ASTER image. The gain and offset settings of the bands in an ASTER image can be obtained from the image metadata file of the raster. Detailed information regarding the unit conversion coefficients can be found in Table 3 (Yüksel et al, 2008; Smith, 2012).

Table 3 The Unit Conversion Coefficient of each ASTER bands (Smith, 2012; Yüksel et al, 2008)

	Band Number	Coefficient [W/(m^2 sr µm)]			
		High Gain	Normal Gain	Low Gain 1	Low Gain 2
VNIR	1	0,6760	1,6880	2,2500	N/A
	2	0,7080	1,4150	1,8900	
	3N	0,4230	0,8620	1,1500	
	3B	0,4230	0,8620	1,1500	
SWIR	4	0,1087	0,2174	0,2900	0,2900
	5	0,0348	0,6960	0,0925	0,4090
	6	0,0313	0,0625	0,0830	0,3900
	7	0,0299	0,0597	0,0795	0,3320
	8	0,0209	0,0417	0,0556	0,2450
	9	0,0159	0,0318	0,0424	0,2650
TIR	10	N/A	0,006882	N/A	N/A
	11		0,00678		
	12		0,00659		
	13		0,005693		
	14		0,005225		

3.3.2. Recalibration of ASTER TIR Images

ASTER TIR products processed before Feb 8, 2006 are known to include an error due to delay in Radiometric Calibration Coefficient (RCC) updating. This error was reduced for RCC version 2.09 or later, which relate to the products observed after October 2002. However, for the RCC versions before 2.09 the error is large. Therefore, TIR images processed before the date stated requires recalibration before any further analysis. Recalibration coefficients only require observation date (UTC) and the RCC version of the image both of which can be found in metadata file. Along with the coefficients estimated calibrated errors are also provided (Tonooka et al, 2003; Sakuma et al, 2005). The modified method follows a linear approach based on the equation below.

$$\text{Recalibrated Radiance} = (A * \text{Original Radiance}) + B$$

where

Original_Radiance	*calibrated at-sensor radiance*
A	*first constant of RCC,*
B	*second constant of RCC*

The coefficients and estimated errors of radiance and temperature are presented in Table 4.

Table 4 Radiometric calibration coefficient (RCC) for ASTER TIR bands (Tonooka et al, 2003; Sakuma et al, 2005)

Band	A	B	Estimated Changes (Upper: Radiance, Lower: Temperature)			
			@ 270 K	@ 300 K	@ 320 K	@ 340 K
10	1,008392	-0,0414	-0,000	+0,037	+0,072	+0,115
			-0,00 K	+0,20 K	+0,31 K	+0,41 K
11	1,016543	-0,0861	+0,000	+0,074	+0,140	+0,222
			+0,00 K	+0,41 K	+0,62 K	+0,82 K
12	1,029099	-0,1595	+0,000	+0,128	+0,240	+0,377
			+0,00 K	+0,73 K	+1,12 K	+1,47 K
13	1,014767	0,0867	-0,000	+0,057	+0,105	+0,161
			-0,00 K	+0,39 K	+0,61 K	+0,81 K
14	1,018525	-0,1082	+0,000	+0,066	+0,120	+0,182
			+0,00 K	+0,49 K	+0,77 K	+1,03 K

3.3.3. Resampling

ASTER VNIR, SWIR, and TIR subsystems have different spatial resolutions; 15m, 30m and 90m respectively. In order to perform image fusion the spatial resolutions should be the same which requires resampling. Down-sampling VNIR data (15m) to SWIR (30m) or TIR resolution (90m) reduces the level of detail, while up-sampling TIR and SWIR to VNIR resolution does not change the level of detail significantly. All the TIR and SWIR bands are resampled according to nearest neighbour resampling method to 15m where VNIR Band 3N is used to match reference and to ensure the pixels are superimposed correctly.

3.4. Spectral Indices

Spectral indices which are pre-defined coefficients. They are used to derive the physical meaning indicated by the image data. Thus the spectral index images show the differentiation of the selected outcrops providing a useful facility for the geological interpretation.

Several indices for surface material discrimination based on ASTER SWIR and TIR data can be found in the literature. This present research utilizes sulphate and mafic indices for VNIR-TIR fusions and OHIa index for VNIR-SWIR fusions to test the improvement of image fusion have over non-fused images. More ASTER TIR and SWIR spectral indices are present in GUI and their equations are given in next chapter as they are not part of the study.

3.4.1. TIR Spectral Indices

The mafic index (MI) which is essentially based on the bulk silica content of the target materials is defined by the equation below based on the spectral emissivity and absorption property of silica. (Ninomiya and Fu, 2002)

$$MI = \frac{Band12}{Band13}$$

The next index calculated for TIR is the sulphate index (SI). The spectral property of the sulphate minerals such as gypsum shows high emissivity in ASTER band-10 and band-12 region and high absorption in ASTER band-10 region (Öztan and Süzen, 2011).

$$SI = \frac{Band10 * Band12}{Band11 * Band11}$$

3.4.2. SWIR Spectral Indices

The hydroxyl index “a” (OHIa) is calculated for SWIR bands of ASTER and is used to reveal hydroxyl bearing minerals such as montmorillonite and mica. (Ninomiya and Fu, 2002)

$$OHIa = \frac{Band4 * Band7}{Band6 * Band6}$$

CHAPTER 4

GRAPHICAL USER INTERFACE

Image fusion applications involve large amounts of data and require complex calculations through processes with a relatively high number of steps. To carry out these steps, an easy to use and flexible Graphical User Interface has to be used for time efficiency. The commercial software MATLAB has an Image Processing toolbox which contains many useful commands and utilities that are commonly used in image processing applications (MATLAB, 2011a). In this study a special GUI based on MATLAB is developed and used. The GUI is designed in modular form and as such can be further extended and modified without damaging its integrity. The main window of the GUI is shown in Figure 8. Details on the design and basic capabilities of the GUI are given in this chapter.

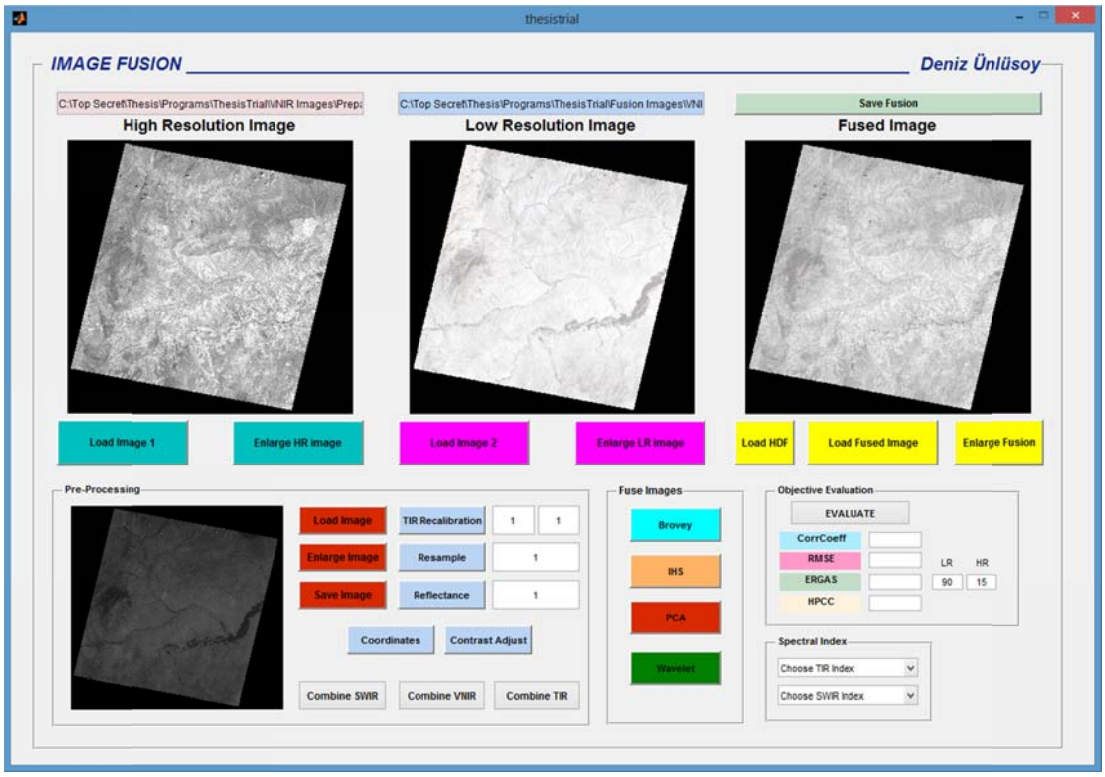

Figure 8 MATLAB graphical user interface for image fusion and spectral indices

The GUI comprises of five main parts each with a separate function; namely the image display, pre-processing, image fusion, spectral indices, and objective evaluation. In the following details of each part is given.

The GUI is capable of loading and displaying a high resolution (HR) image, a low resolution (LR) image, and a display window for the fused image. The buttons used for these purposes are “Load Image 1”, “Load Image 2”, and “Load Fused Image” placed just under the displays. Right next to each load image button is a button to enlarge the loaded image. The buttons for these are “Enlarge HR Image”, “Enlarge LR Image”, and “Enlarge Fusion”, each enlarging high resolution, low resolution, and fusion images respectively. The name and location of the image files loaded are displayed right above the high and low resolution images. Above the fused image is “Save Fusion” button which is used to save the resulting image fusion from HR and LR images. It is possible to reload an already fused and saved image to the fused image display. The part of the GUI devoted to the part described here is shown in Figure 9.

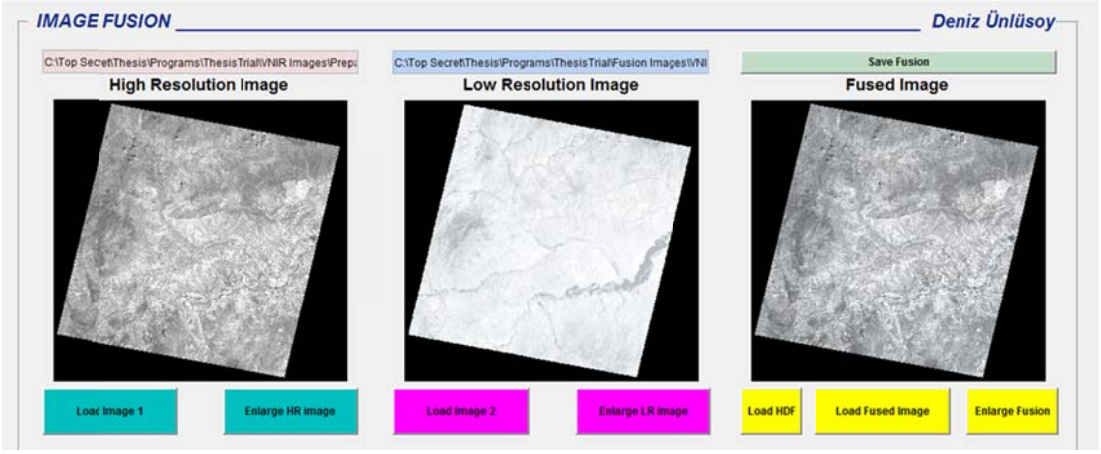

Figure 9 MATLAB graphical user interface for image display.

There is also a special “Load HDF” button for HDF files left of “Load Fused Image” button, which opens the Matlab HDF import tool, shown in Figure 10. From here user selects the data field and the desired band then press the “import” button on the lower right corner. Image data from HDF files are imported as 3 bands per SWIR, VNIR, and TIR. The bands are to be imported with proper names such as; SWIR1, SWIR2, SWIR3, VNIR1, VNIR2, and VNIR3. If the images are not imported with proper names and error message will pop up warning the user while providing the file names required.

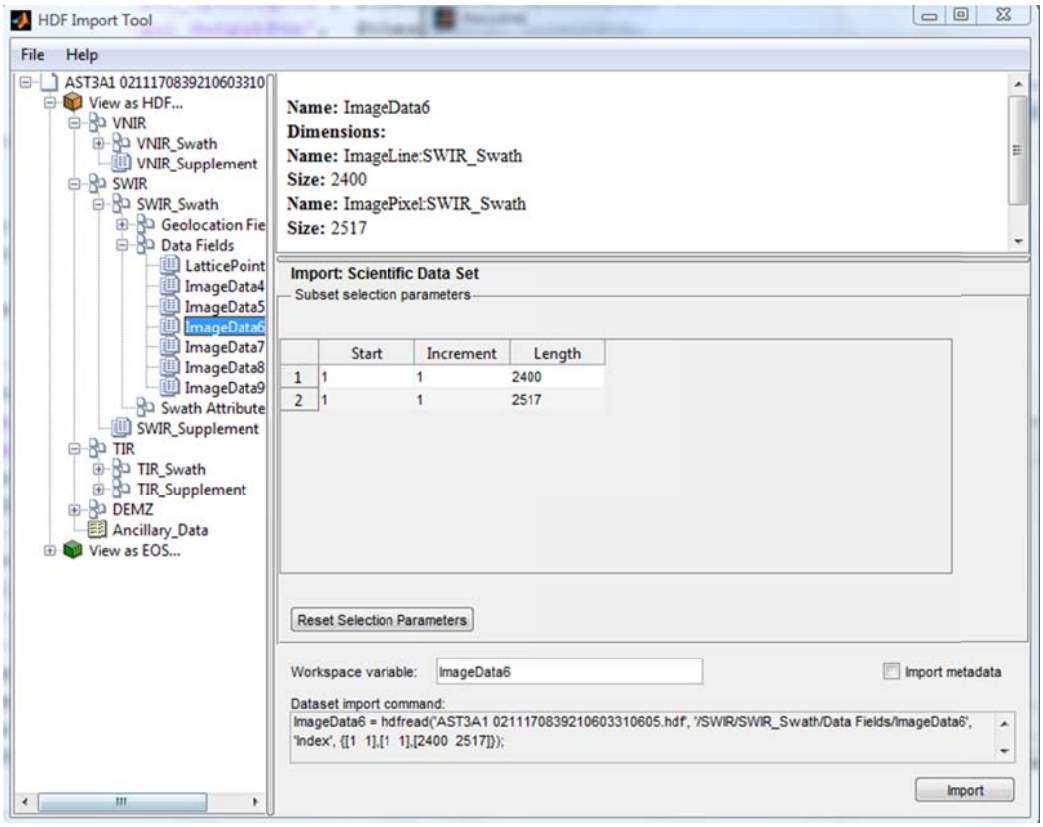

Figure 10 MATLAB graphical user interface HDF import tool.

In "Pre-Processing" section, shown enlarged in Figure 11, there are three buttons used to load, enlarge, and save images that are to go through image processing before the image fusion. A special button "TIR Recalibration" is provide to correct an error in ASTER TIR images processed before Feb 8, 2006 due to delay in Radiometric Calibration Coefficient (RCC) updating. The two edit boxes on the right of this button are to be used for entering the A and B coefficients listed in Table 4. A second button "Resample" is used to resample the images which may be of different resolutions. The resampling multiplier is entered in the edit box on the right side of the button. Since ASTER images have data in the form of thermal emissivity, data should be converted into reflectance. This conversion to reflectance is done by using "Reflectance" button. Next to it there is an edit box for entering the band constant. The Reflectance button is pressed after entering the band constant. If the band constant is not entered then a default value of "1" will be used. User must obtain the relevant band constant according to whether the image data bands were taken in low gain, normal gain, or high gain.

Two additional buttons, "Coordinates" and "Contrast Adjust" below may be used to show geographical coordinates on the images (provided that they are given) and to perform a simple adjustment of contrast on the loaded image. A more sophisticated adjustment of contrast is performed by the MATLAB "imtool" command described later in this section.

The bottom row contains the three buttons "Combine VNIR", "Combine SWIR", and "Combine TIR" which will merge imported HDF images into false colour RGB images and display them. From the displayed image user can save the images with most common image formats of preference available in Windows Explorer.

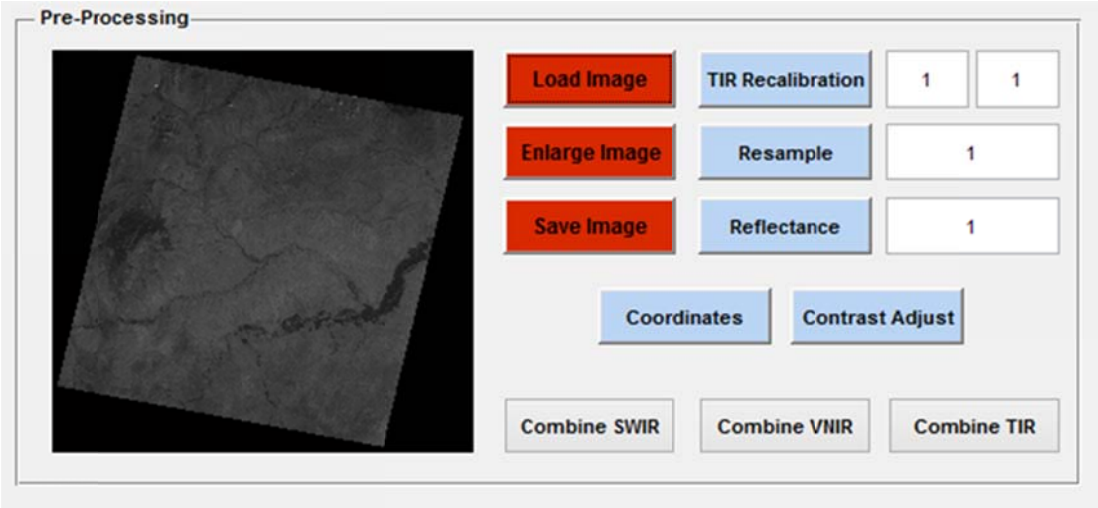

Figure 11 MATLAB graphical user interface Pre-Processing tool.

On the third part of the GUI, there are for buttons each associated with a different image fusion method; namely the Brovey IHS, PCA, and Wavelet image fusion methods. Pressing on one of these buttons will fuse the high and low resolution images and display the fused image at the "Fused Image" location in the first part.

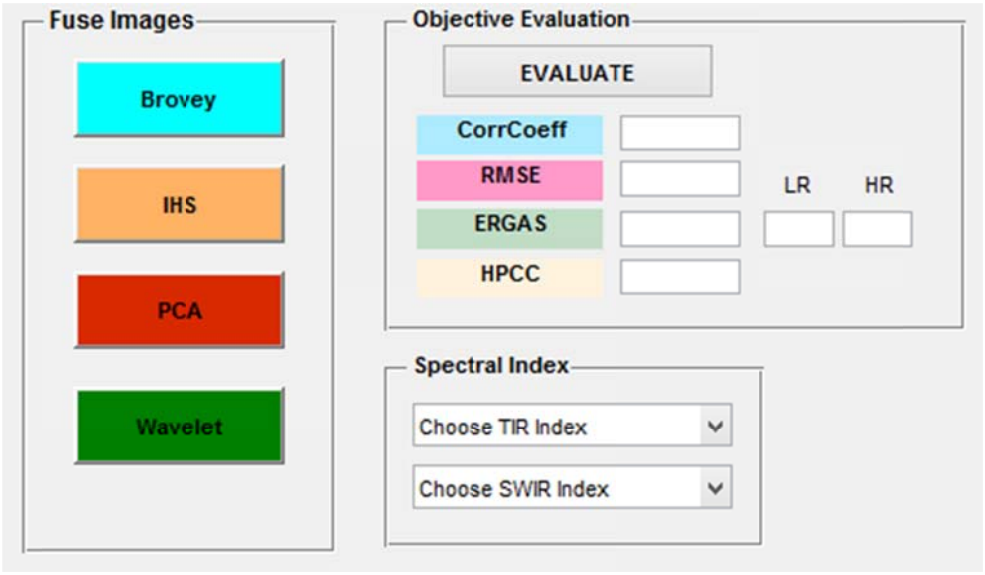

Figure 12 MATLAB graphical user interface for image fusion and objective evaluation.

Wavelet image fusion button opens a very detailed wavelet toolbox of MATLAB, shown in Figure 13, with its own GUI. On this GUI, "Image Fusion" option under "Specialized Tools 2-D" must be selected. This opens a new window shown in Figure 14. Here under "File" menu, the high and low resolution images to be fused are loaded. Both images have to be loaded in RGB format. The "Decomposition level" vary from 1 to 5, and for the applications of interest in this study, the highest value is selected and decompose button is to be pressed. Then the fusion method is selected and the "Apply" button has to be pressed to make the fusion. At the end the resulting fused image can be saved "Save synthesized image under "File" menu.

The fourth part of the GUI is for the objective evaluation of the fusion process. Pressing the "Evaluate" button on Figure 12 will yield the results of the objective evaluation of the fused image in the form of Correlation Coefficient, RMSE, ERGAS, and High-pass Correlation Coefficient. The first three evaluation methods compare the spectral quality of the fused image with the LR image, while the last one makes a spatial quality comparison with the high resolution image. For this function to work HR, LR, and Fused images must all be loaded on the GUI. For ERGAS to work the pixel sizes of HR and LR images must be entered in to the boxes next to ERGAS result display box.

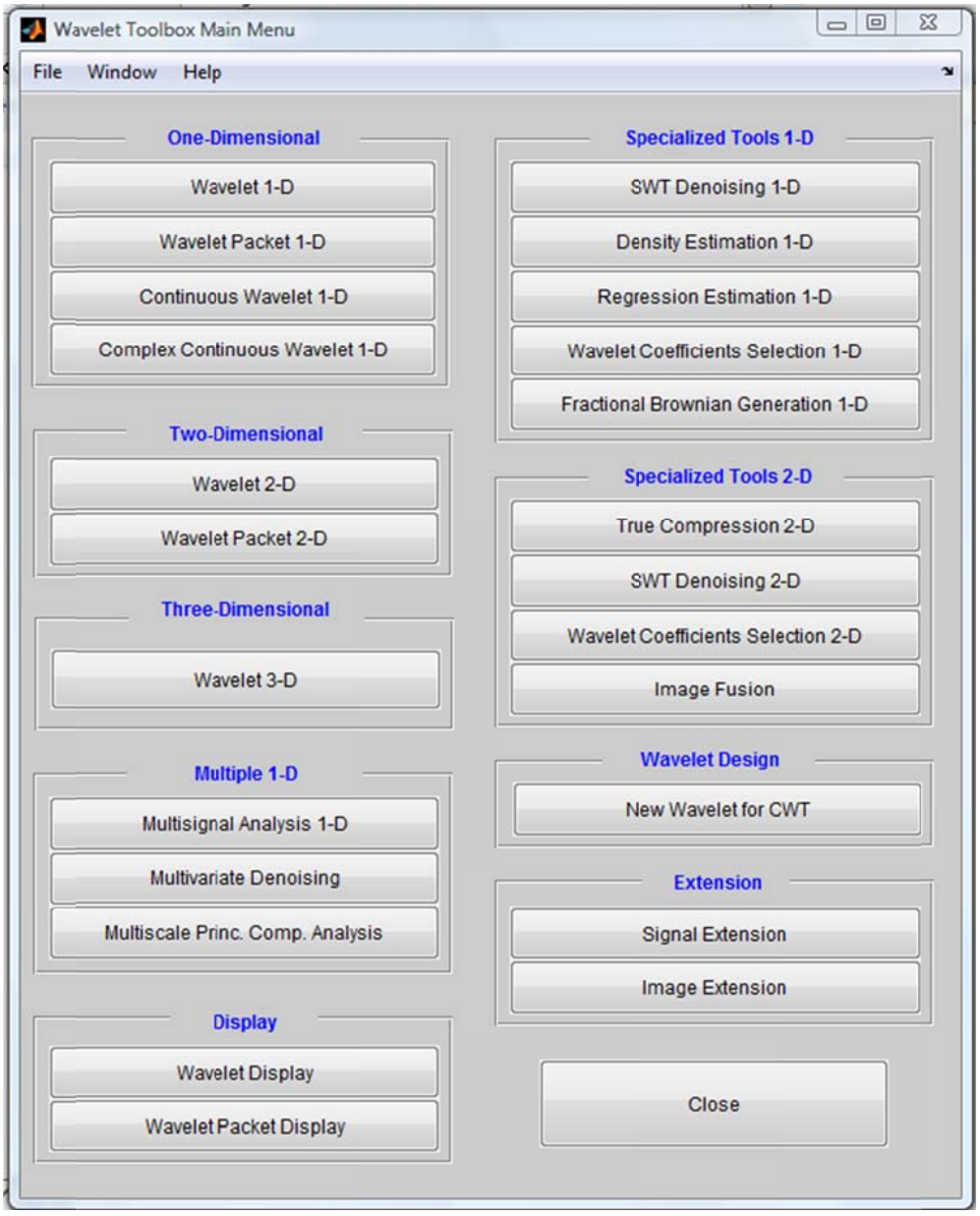

Figure 13 MATLAB wavelet toolbox menu

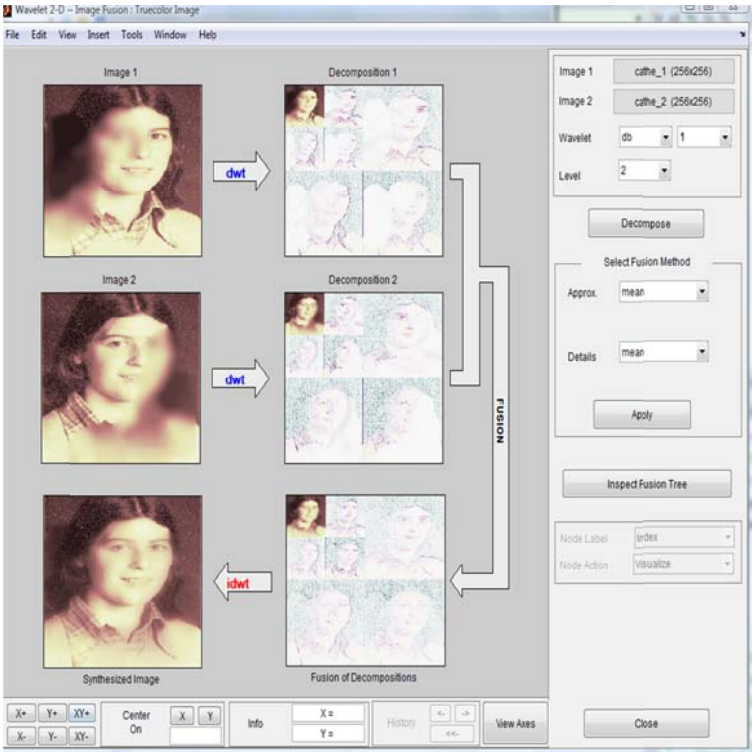

Figure 14 MATLAB wavelet toolbox-wavelet 2-D image fusion

The fifth and final part of the GUI is the 'Spectral Index' box on the right bottom of Figure 12. It has two drop boxes for creating spectral index map from the image in the fused image display as shown in Figure 15 in their open forms. The first drop box is for producing Quartz (QI), Sulphate (SI), Carbonate (CaI), and Mafic (MI) spectral index maps. User must make sure that the fused image has TIR as LR component. The second drop box is for fused images that have SWIR for LR component and contains Brightness (BI), Alunite (AI), Calcite (CI), Kaolinite (KI), Residual (RI), OHIa and OHIb spectral index map options.

Equations of spectral indices not provided in previous chapter's "3.4. Spectral Indices" section are given below.

QI = (band11*band11) / (band10*band12) (Ninomiya and Fu, 2002)

CaI = band13 / band14 (Ninomiya and Fu, 2002)

BI = 0.460*band5+0.452*band6+0.427*band7+0.458*band8+0.438*band9 (Yamaguchi and Takeda, 2003)

Al = -0.511*band5-0.003*band6+0.802*band7+0.059*band8-0.304*band9 (Yamaguchi and Takeda, 2003)

CI = -0.232*band5+0.478*band6+0.802*band7+0.072*band8+0.436*band9 (Yamaguchi and Takeda, 2003)

KI = 0.663*band5-0.336*band6+0.387*band7-0.511*band8-0.191*band9 (Yamaguchi and Takeda, 2003)

RI = 0.184*band5+0.674*band6-0.141*band7-0.050*band8-0.699*band9 (Yamaguchi and Takeda, 2003)

OHIb = (band4*band7) / (band5*band5) (Ninomiya and Fu, 2002)

Selecting any spectral index from the drop boxes will open an image tool as shown in Figure 16 with the spectral index image in it. From this image tool, the user can use adjust contrast option (which is the 4th button from the left on the toolbar) to get the ideal image contrast in order to express any feature of interest better. After the best possible contrast is obtained, the user can save the image in any of the available formats.

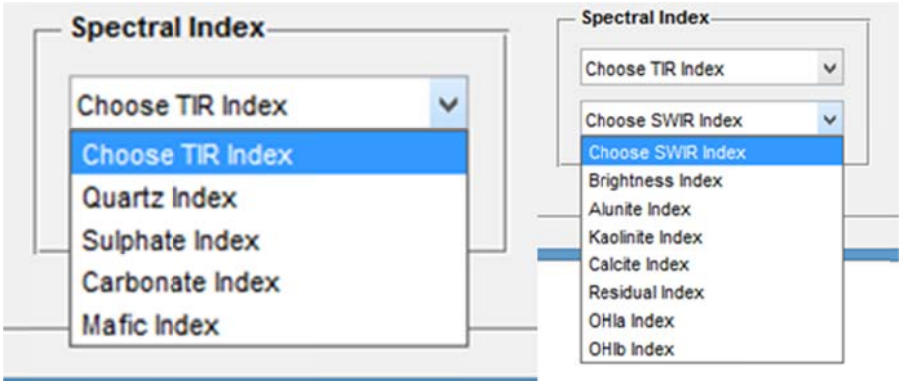

Figure 15 Spectral Index; TIR index and SWIR index drop box selections

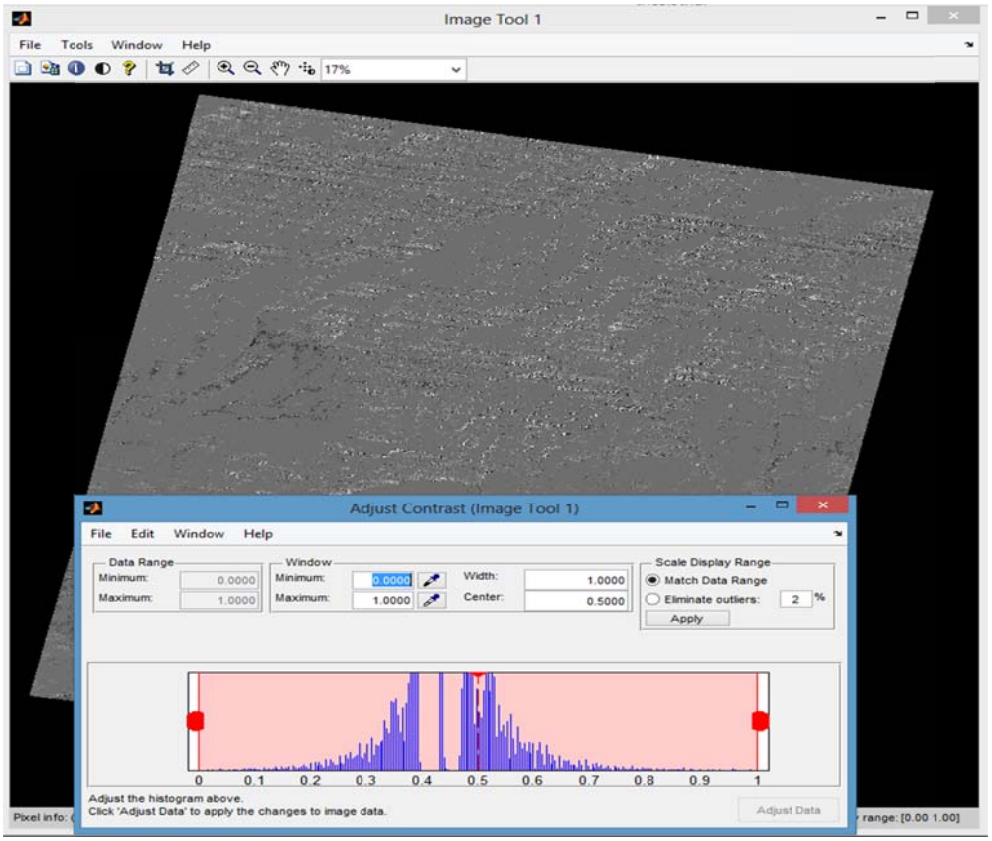

Figure 16 MATLAB image toolbox and contrast adjustment

CHAPTER 5

EXPERIMENTATIONS AND RESULTS

5.1. Image Fusion

5.1.1. VNIR-TIR Image Fusion

In this step VNIR 3N band is used as the high resolution band since it is least affected by atmospheric effects, thus creating less error during the fusion. All TIR images are resampled to 15 meters per pixel resolution before the fusion and selected bands are combined into RGB images for distinct spectral index maps. TIR bands 10, 11, and 12 are combined into one RGB image to be fused with a VNIR 3N RGB image to produce Quartz and Sulphate indices, while TIR bands 12, 13, and 14 are used for Carbonate and Mafic indices.

In Wavelet transform decomposition level was chosen as level 5. Approximation and details were picked as the mean of both images. These settings gave the best outcome of Wavelet transform image fusion. Fused images using IHS, Brovey, PCA, and Wavelet transforms are given in Figures 17 to 20.

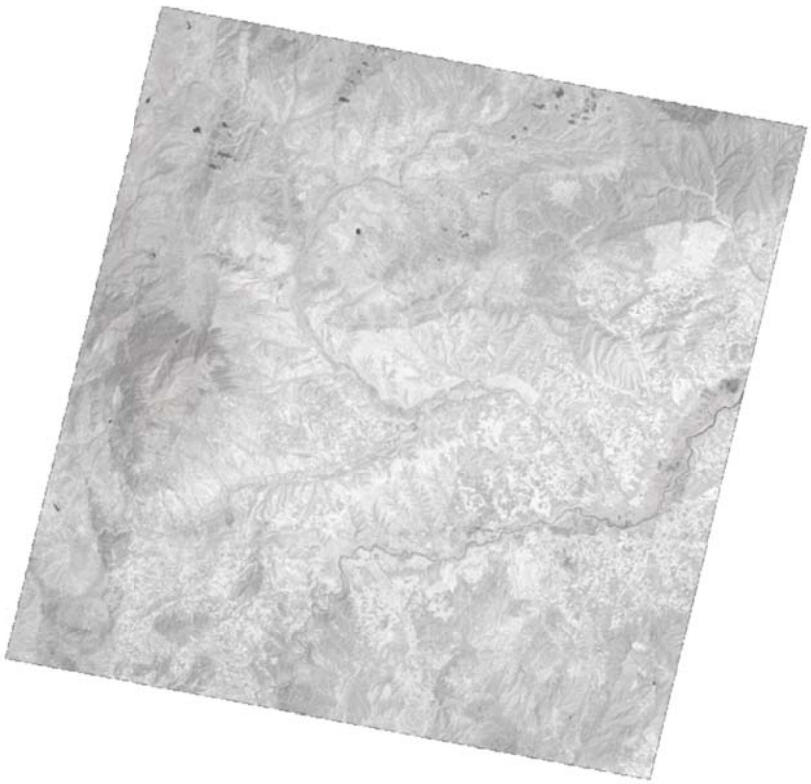

Figure 17 VNIR 3N bands fused with TIR bands 10, 11, and 12 with Brovey Transformation

Figure 18 VNIR 3N bands fused with TIR bands 10, 11, and 12 with IHS Transform.

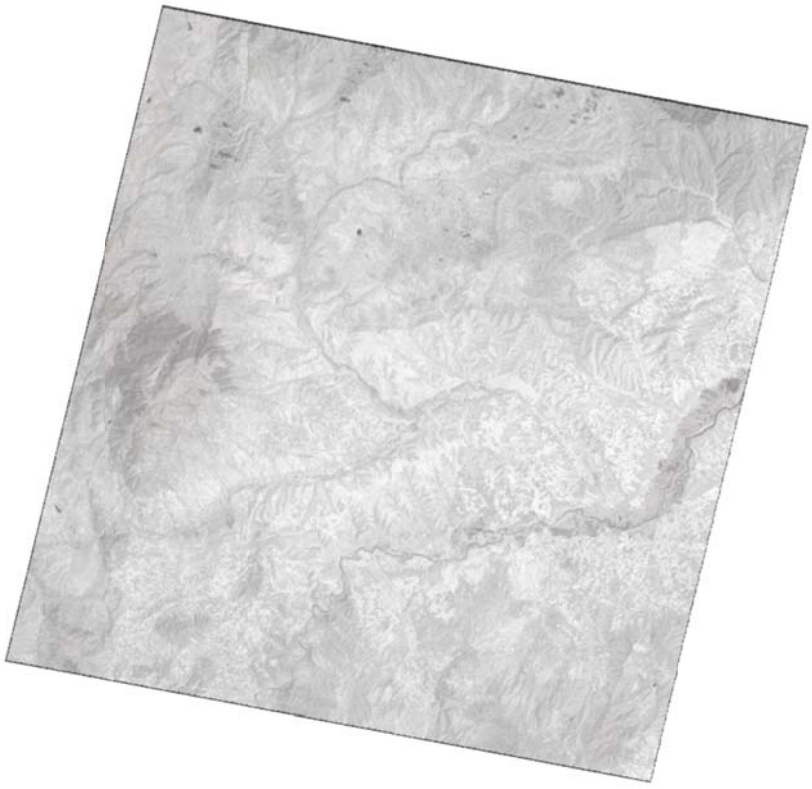

Figure 19 VNIR 3N bands fused with TIR bands 10, 11, and 12 with PCA Transform.

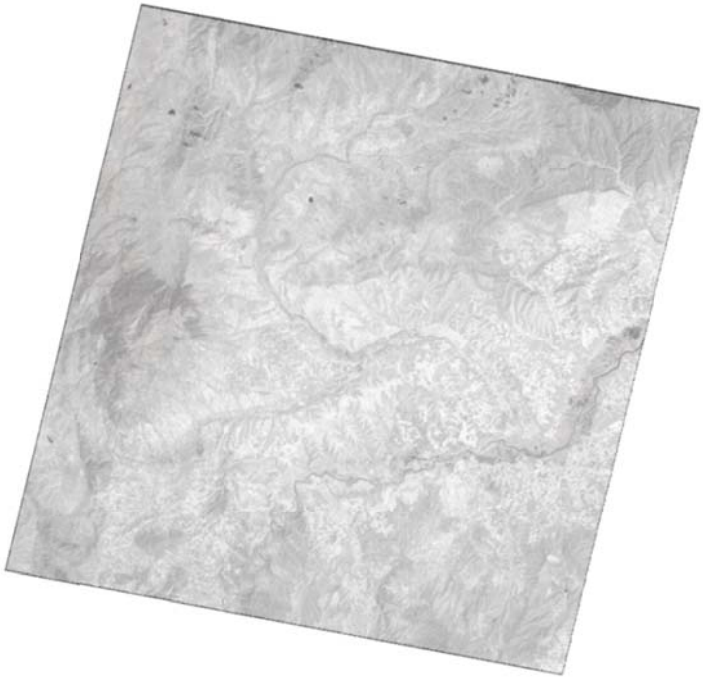

Figure 20 VNIR 3N bands fused with TIR bands 10, 11, and 12 with Wavelet Transform.

Correlation Coefficient (CC), RMSE, and ERGAS were used to check the spectral compatibility between TIR and fused images. As seen in Table 5 and 6, results were encouraging in Brovey, Wavelet, and PCA transform methods, while IHS had relatively poor results as its CC was lower while RMSE and ERGAS were significantly higher.

In contrast the HPCC which compared VNIR and fused images for resolution compatibility revealed that IHS has significantly higher resolution compared to the other three methods. The meaning of this is that more 90 meter pixels were divided into smaller 15 meter pixels with distinct DNs, whereas the spatial detail is overshadowed by the lack of spectral information in IHS transform's case which resulted in most pixels to apparently remain 90 meter visually because the smaller pixels all have the same DN.

Table 5 Objective evaluation of VNIR3N and TIR 10, 11, 12 band fusion, best results are in bold

	IHS	Brovey	PCA	Wavelet
CC	0.95071	0.9886	**0.99253**	0.99020
RMSE	51.7431	28.1597	**22.8849**	25.0625
ERGAS	5.5540	3.0226	**2.4564**	2.6902
HPCC	**0.99547**	0.69225	0.78210	0.84558

Table 6 Objective evaluation of VNIR3N and TIR 12, 13, 14 band fusion, best results are in bold

	IHS	Brovey	PCA	Wavelet
CC	0.95109	0.98865	**0.99262**	0.99034
RMSE	53.0334	28.9384	**23.4059**	25.7086
ERGAS	5.6441	3.0785	**2.4897**	2.735
HPCC	**0.99709**	0.69465	0.7836	0.84876

5.1.2. VNIR-SWIR Image Fusion

Next step is to fuse SWIR 4, 5, 6, 7, 8, and 9 bands with VNIR 3N band. All SWIR images are resampled to 15 meters per pixel resolution before the fusion. SWIR bands 4, 5, and 6 are combined into one RBG image to be fused with a VNIR 3N RGB image and TIR bands 7, 8, and 9 are used for a separate fusion since the image fusion algorithms work for RGB images. After fusion each fused band is separated and saved individually. Fused images of VNIR 3N band and SWIR band 9 using IHS, Brovey, PCA, and Wavelet transforms are given in Figures 21 to 24.

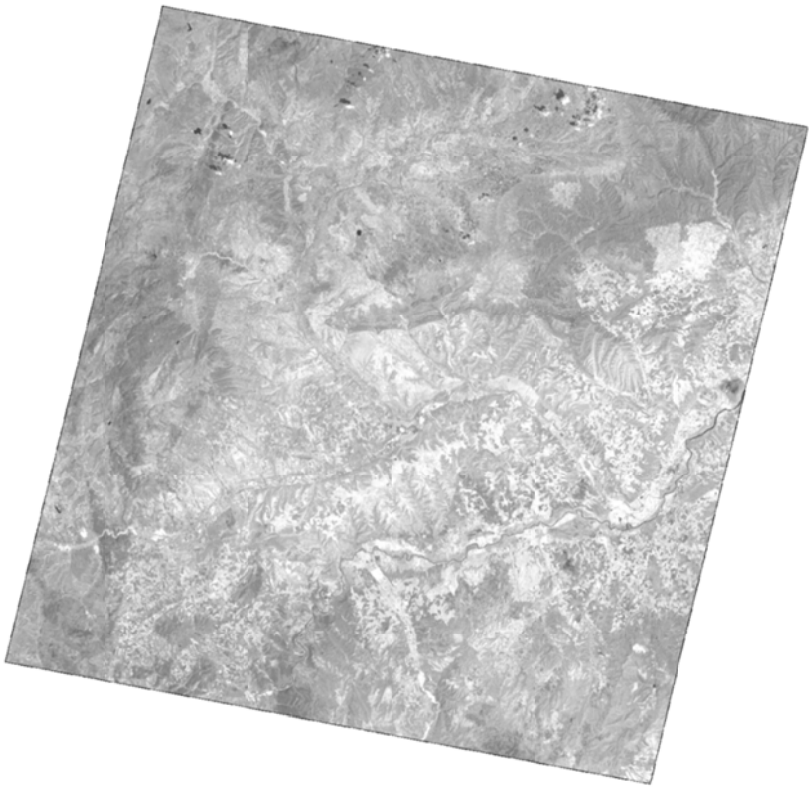

Figure 21 VNIR 3N band fused with SWIR band 9 with IHS Transformation.

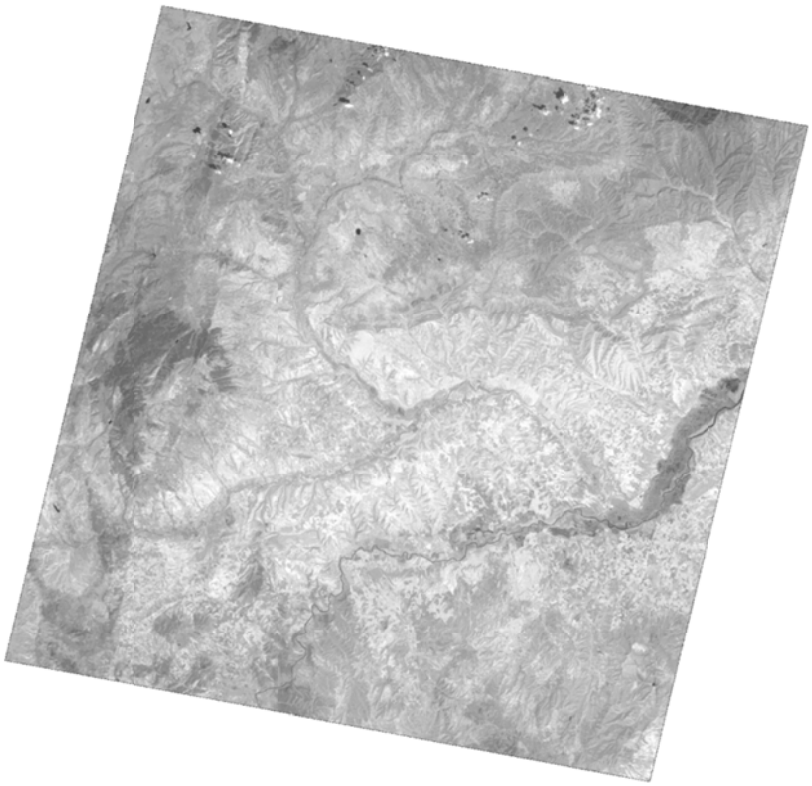

Figure 22 VNIR 3N band fused with SWIR band 9 with Brovey **T**ransformation

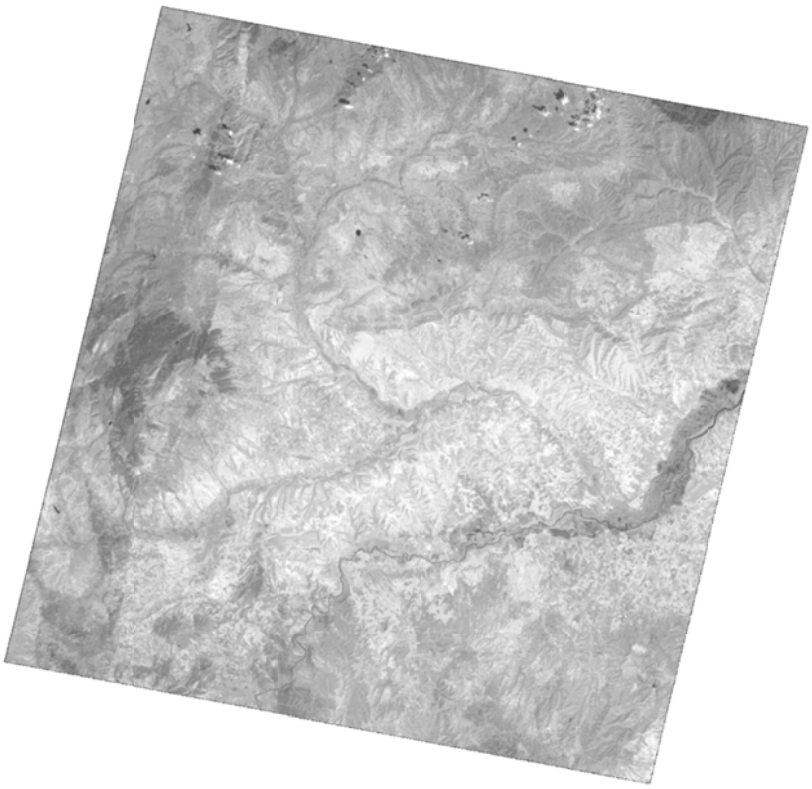

Figure 23 VNIR 3N band fused with SWIR band 9 with PCA Transformation

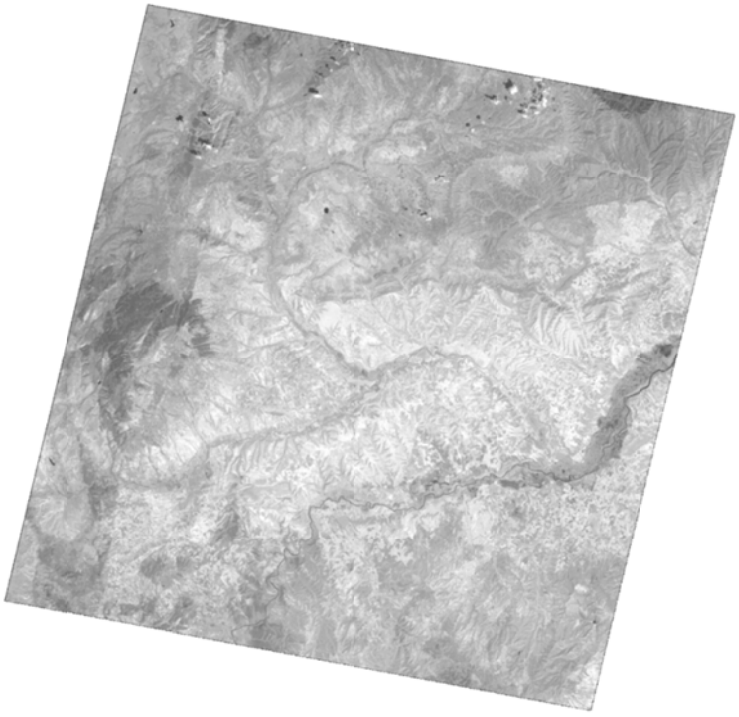

Figure 24 VNIR 3N band fused with SWIR band 9 with Wavelet Transformation

Correlation coefficient (CC), RMSE, and ERGAS were used to check the spectral compatibility between SWIR and fused images, as seen in Table 7 and 8. Compared to TIR fusions spectral evaluations displayed higher results. Brovey method replaced PCA in terms of highest spectral evaluation results in SWIR fusions.

Once again IHS is significantly better in spatial improvement compared to the other three methods. However it is observed that there is an overall decrease in spatial improvement in all methods. This is the result of SWIR having 30 meter pixels compared to TIR's 90 meter pixels, leaving less room for resolution increase.

Table 7 Objective evaluation of VNIR3N and SWIR 4, 5, 6 band fusion, best results are in bold

	IHS	Brovey	PCA	Wavelet
CC	0.96609	**0.992**	0.99154	0.99114
RMSE	24.1758	**12.1043**	12.2782	12.4454
ERGAS	9.7636	**4.8706**	4.9445	5.0124
HPCC	**0.93967**	0.72357	0.7839	0.79674

Table 8 Objective evaluation of VNIR3N and SWIR 7, 8, 9 band fusion, best results are in bold

	IHS	Brovey	PCA	Wavelet
CC	0.95871	**0.98987**	0.9893	0.98887
RMSE	26.6999	**13.6396**	13.8135	13.9696
ERGAS	10.7774	**5.4817**	5.5765	5.6366
HPCC	**0.85898**	0.66283	0.70756	0.72129

5.2. Visual Accuracy Assessment

5.2.1. TIR Spectral Indices

In this study, mafic (MI) and sulphate (SI) indices for TIR data are used. The results of the spectral indices are displayed in linear grey-scale as the resultant image is a single layer. White pixels are the minerals which the index is meant to reveal. Additionally, in order to facilitate visual interpretation, the resultant layers are subjected to contrast enhancement through linear stretching.

Each spectral index used in this study was applied on TIR images fused with VNIR 3N bands. Four different image fusion methods were utilized for each index. Figures 25 and 26 are given for a visual appraisal of the degree of spectral information preserved for each image fusion method. Each figure shows the non-fused index map together with the fused images obtained by the four methods used. Increased resolution was clear in each fused image. The non-fused image has sharp gradients in pixel boundaries; while fused images, especially IHS, have slowly varying slopes with considerably more information than the 90 meter resolution of TIR images.

While objective evaluation results from previous section displays differences between image fusion methods, the scale of the study area denies almost any visual differences without zooming in. This problem will be addressed in chapter 6.

The applied result of MI can be seen in Figure 25. The North Anatolia Ophiolitic Melange related rocks are visible here on the left side of the image as white stripes elongating in the north-south direction. Most of the area has light coloured pixels which belong to ophiolitic rocks of NAOM.

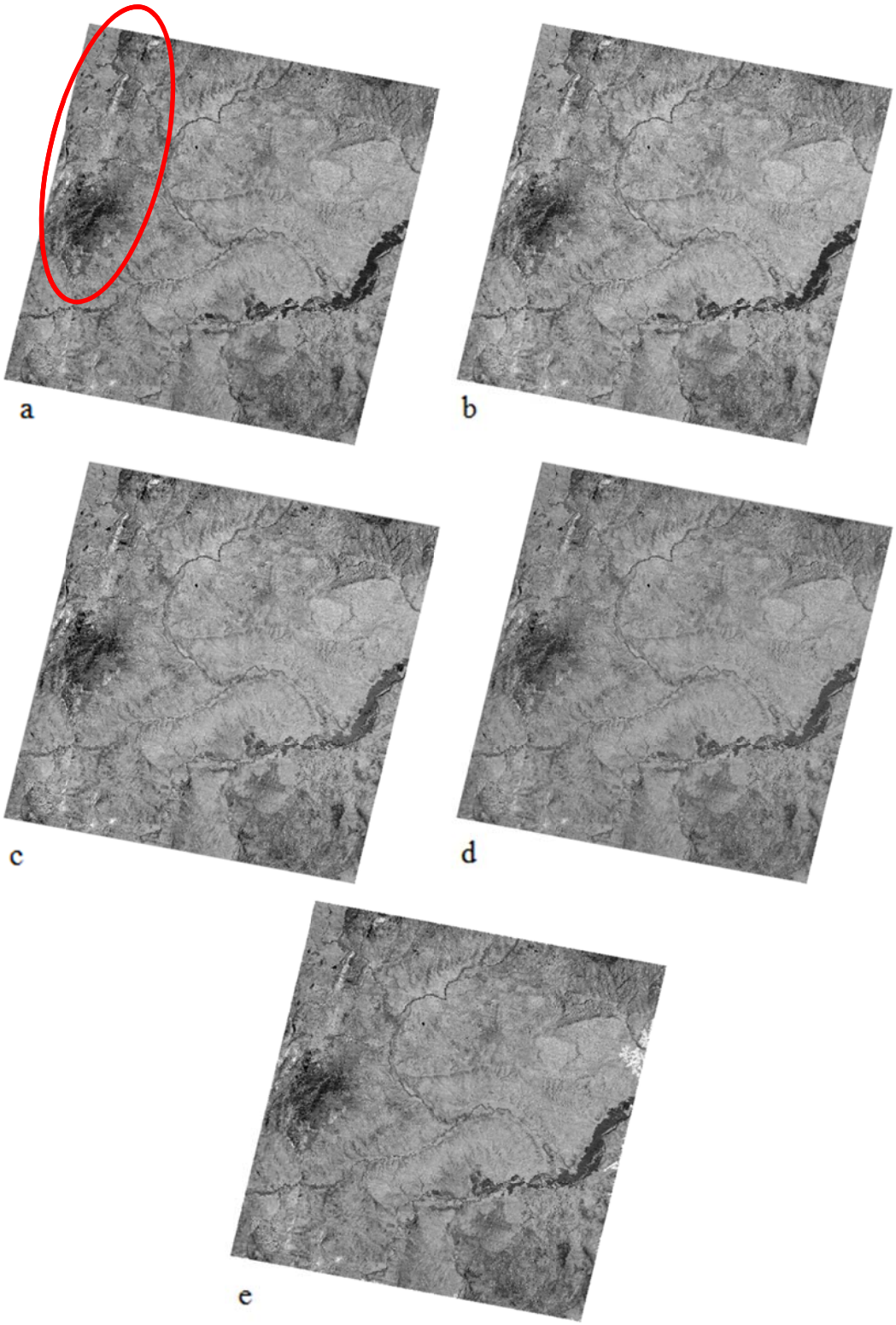

Figure 25 Mafic index images: a) non-fused and with b) Brovey, c) IHS, d) PCA, and e) Wavelet image fusion

The applied result of SI can be seen in Figure 26. In the study area Bozkır Formation is easily detected and is widespread throughout the area. The high concentration around old river beds is further evidence for the accuracy of the spectral index as evaporates such as gypsum presence in such locations.

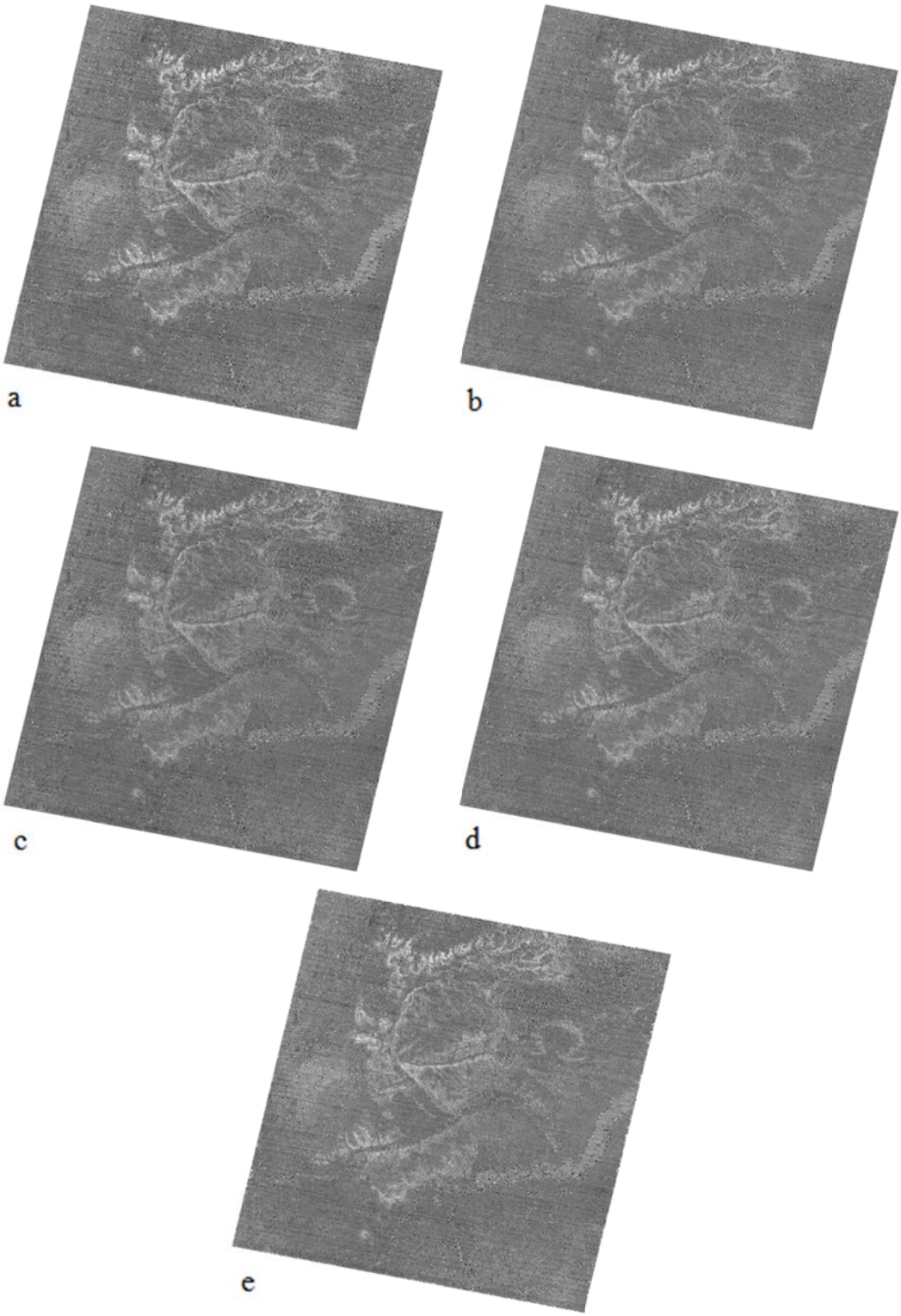

Figure 26 Sulphate index images: a) non-fused and with b) Brovey, c) IHS, d) PCA, and e) Wavelet image fusion

5.2.2 SWIR Spectral Indices

The next part is the preparation of spectral index maps of SWIR bands. OHIa index defined for SWIR is used. Just like in the previous case, white pixels are the minerals which the index is meant to reveal, calcite index being the exact opposite with black pixels representing calcite minerals. In order to facilitate visual interpretation, the resultant layers are subjected to contrast enhancement through linear stretching.

OHIa spectral index map used in this study was applied on SWIR bands 4, 5, 6, 7, 8, and 9 fused with VNIR 3N band. Four different image fusion methods were utilized for each index. Figure 27 is given for a visual appraisal of the degree of spectral information preserved for each image fusion method. The figure shows the non-fused index map together with the fused images obtained by the four methods used. PCA, Wavelet, and Brovey transform image fusion methods display a degree of preservation of the spectral information. The increase in resolution is obvious in each image. Previously homogeneous regions that turned out to have various pixel values after the image fusion is the cause of less sharp looking spectral map.

Loss of spectral information is highest in the IHS based fusion with regard to SWIR spectral indices. This is indicated by the conversion of the dark pixels in the river at the east of the study area to lighter pixels in OHIa map; it can be seen that details of the riverbank on east of the area are lost. Taking the poor objective evaluation results in Table 6 regarding spectral correlation to the original SWIR index maps; it is not possible to tie these differences merely to increase in resolution and the dispersion of previously homogeneous pixels. Despite all these, in all indices IHS provides us with the highest spatial detail. Formations normally unseen in original and other fusion methods are clearly visible and it can be argued that loss of some spectral information may be sacrificed in some applications.

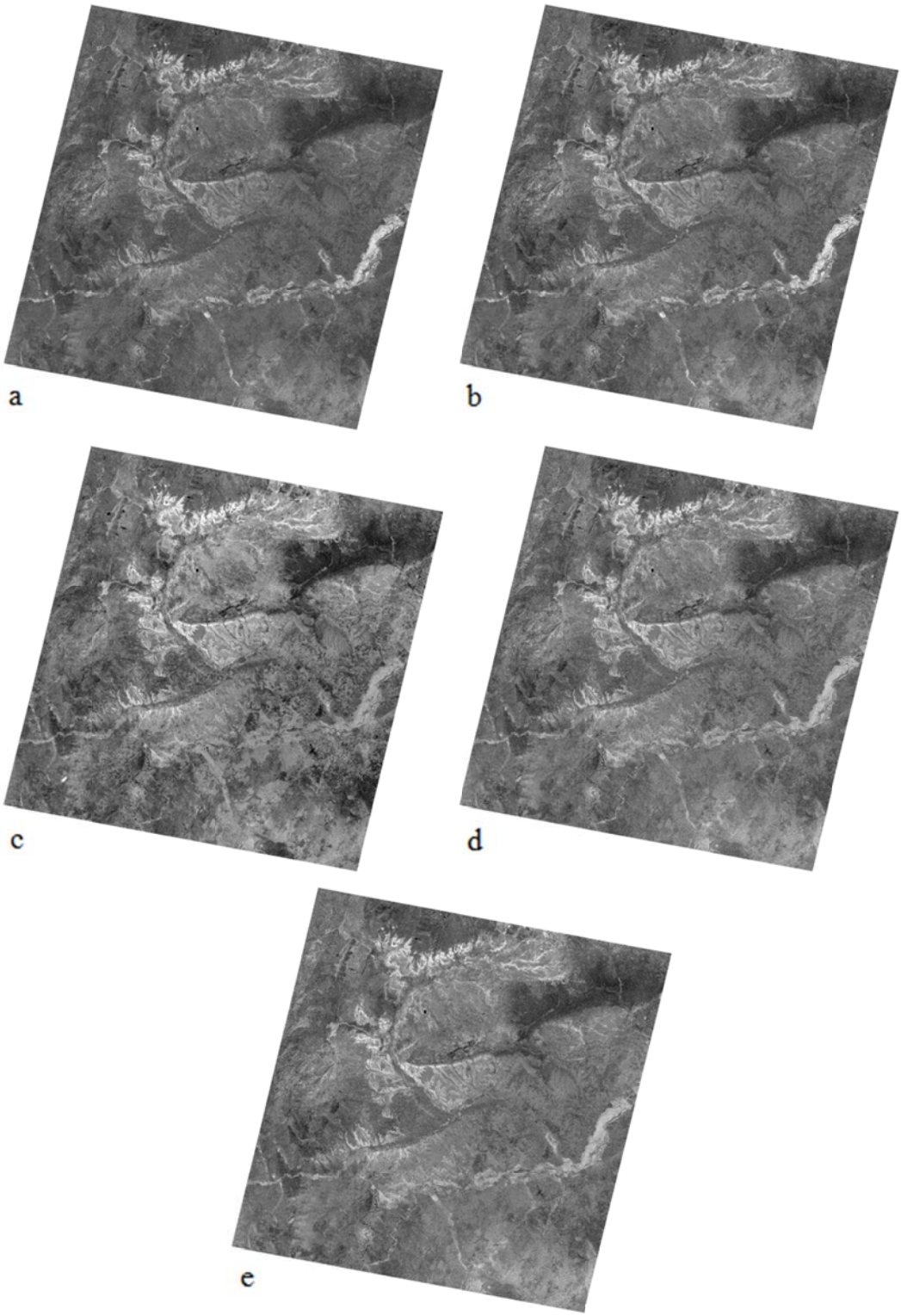

Figure 27 OHIa images: a) non-fused and with b) Brovey, c) IHS, d) PCA, and e) Wavelet image fusion

CHAPTER 6

CASE STUDIES

6.1. First Case Study

As seen in previous chapter, it is difficult to differentiate visually between fused images, obtained using different methods. The same is also the case for the spectral index maps resulting from them, since the study area is too large. In order to complete the objective of obtaining both objective and subjective evaluation, a smaller area with known geological features of the study area is selected. Figure 28 displays the case study area and its close up in colour composite map (VNIR 3N, 2, 1).

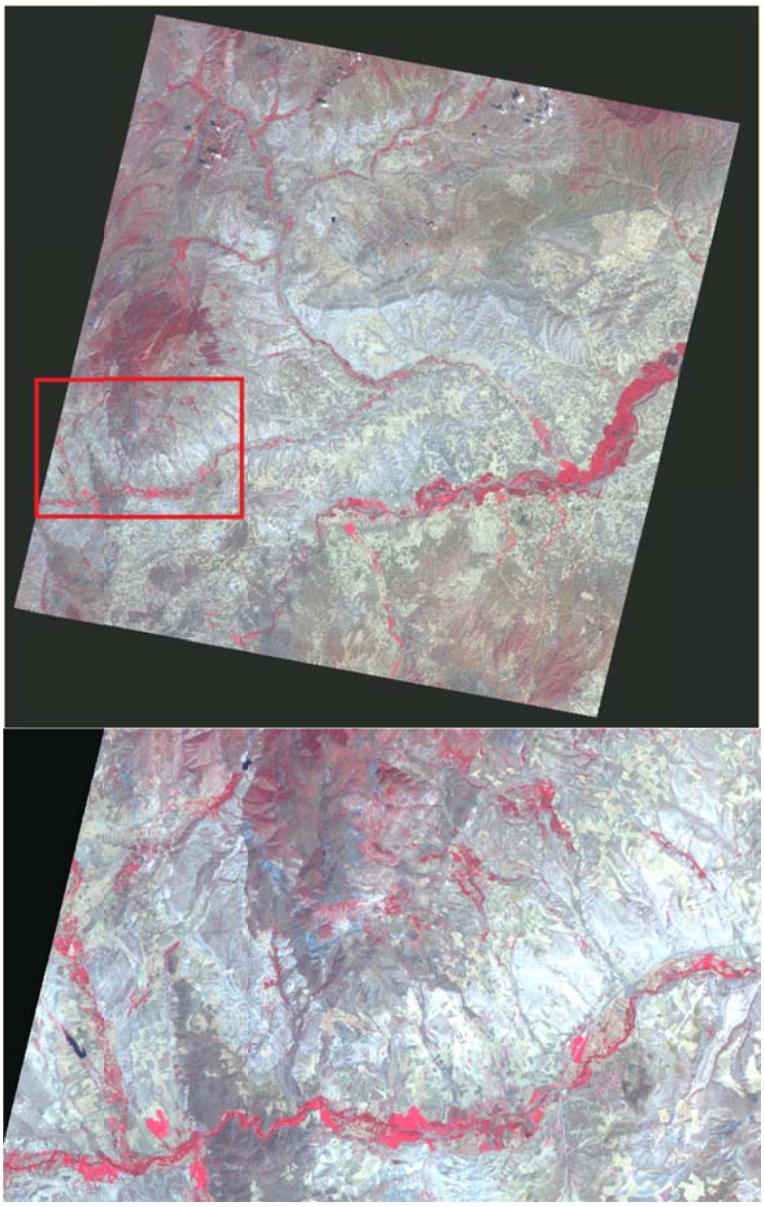

Figure 28 Location and close up of the first case study area (VNIR 3N, 2, 1)

After isolating the case study area from the main images in each band, the pre-processing procedures discussed in chapter 3 were applied on each band image. Brovey, IHS, PCA, and Wavelet ("mean" fusion rule) transformation image fusion techniques were then applied to VNIR3N band and all the SWIR and TIR bands, creating high resolution SWIR and TIR bands. The fused images can be seen in Figures 29 to 32.

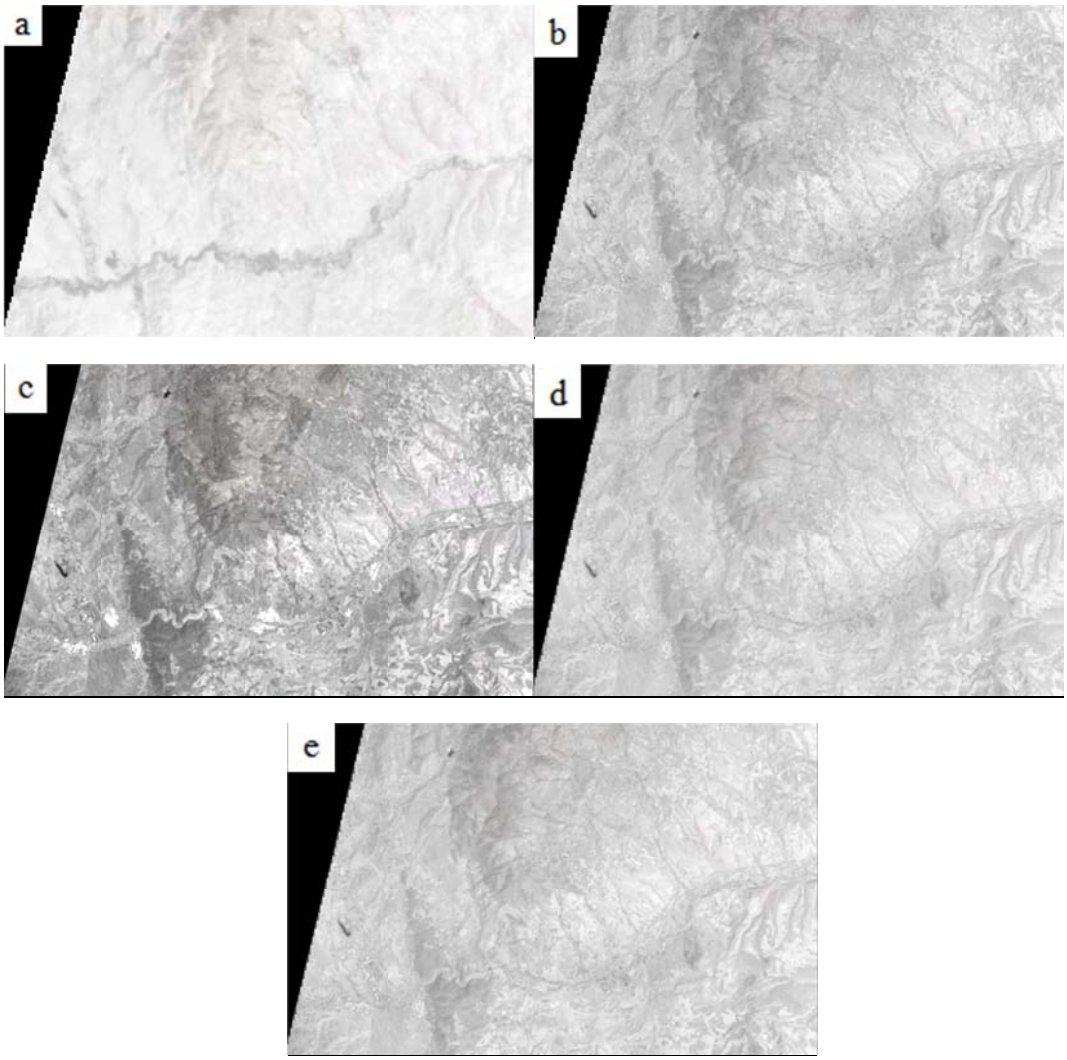

Figure 29 VNIR (3N) - TIR (bands 10, 11, 12) fusion; a) Non-fused, b) Brovey, c) IHS, d) PCA, and e) Wavelet

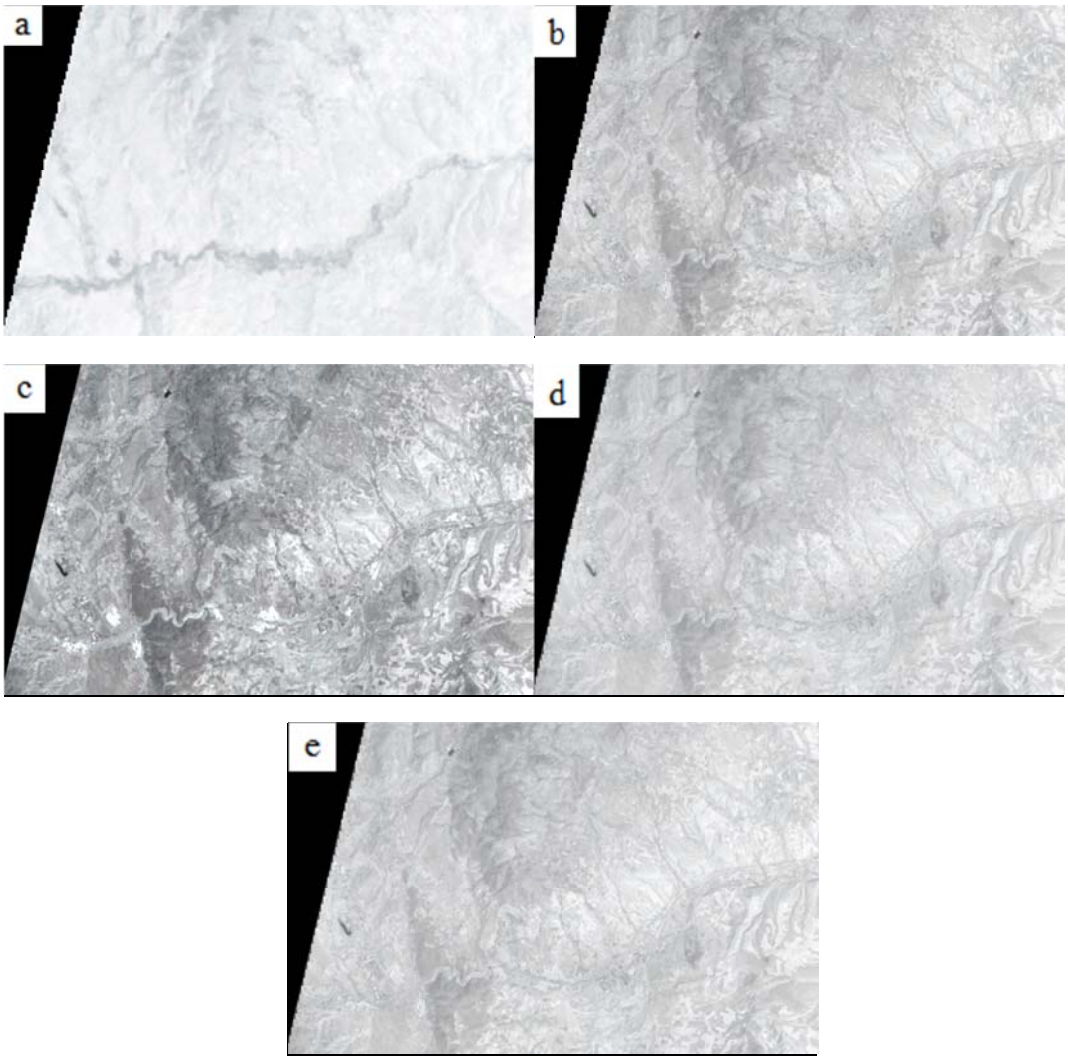

Figure 30 VNIR (3N) - TIR (bands 12, 13, 14) fusion; a) Non-fused, b) Brovey, c) IHS, d) PCA, and e) Wavelet

In Figures 29 and 30, the improvement provided by the fused images is clearly evident by visual comparison. This is expected since for the case of TIR and VNIR bands, the resolution difference between the LR and HR images is significantly high (90m to 15m). IHS transformation is observed to be vastly superior to the other transformations as can be easily observed by visual inspection.

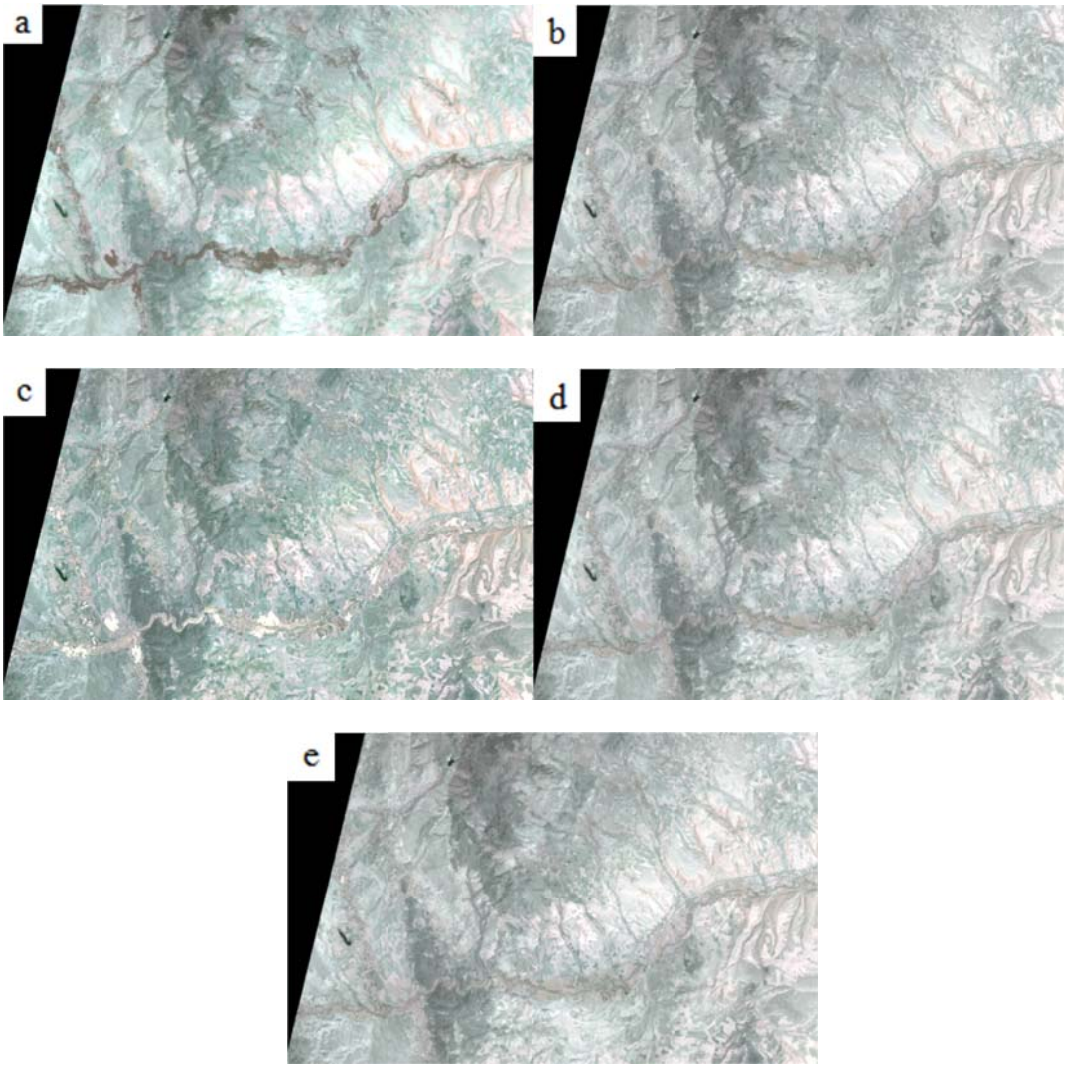

Figure 31 VNIR (3N) -SWIR (bands 4, 5, 6) fusion; a) Non-fused, b) Brovey, c) IHS, d) PCA, and e) Wavelet

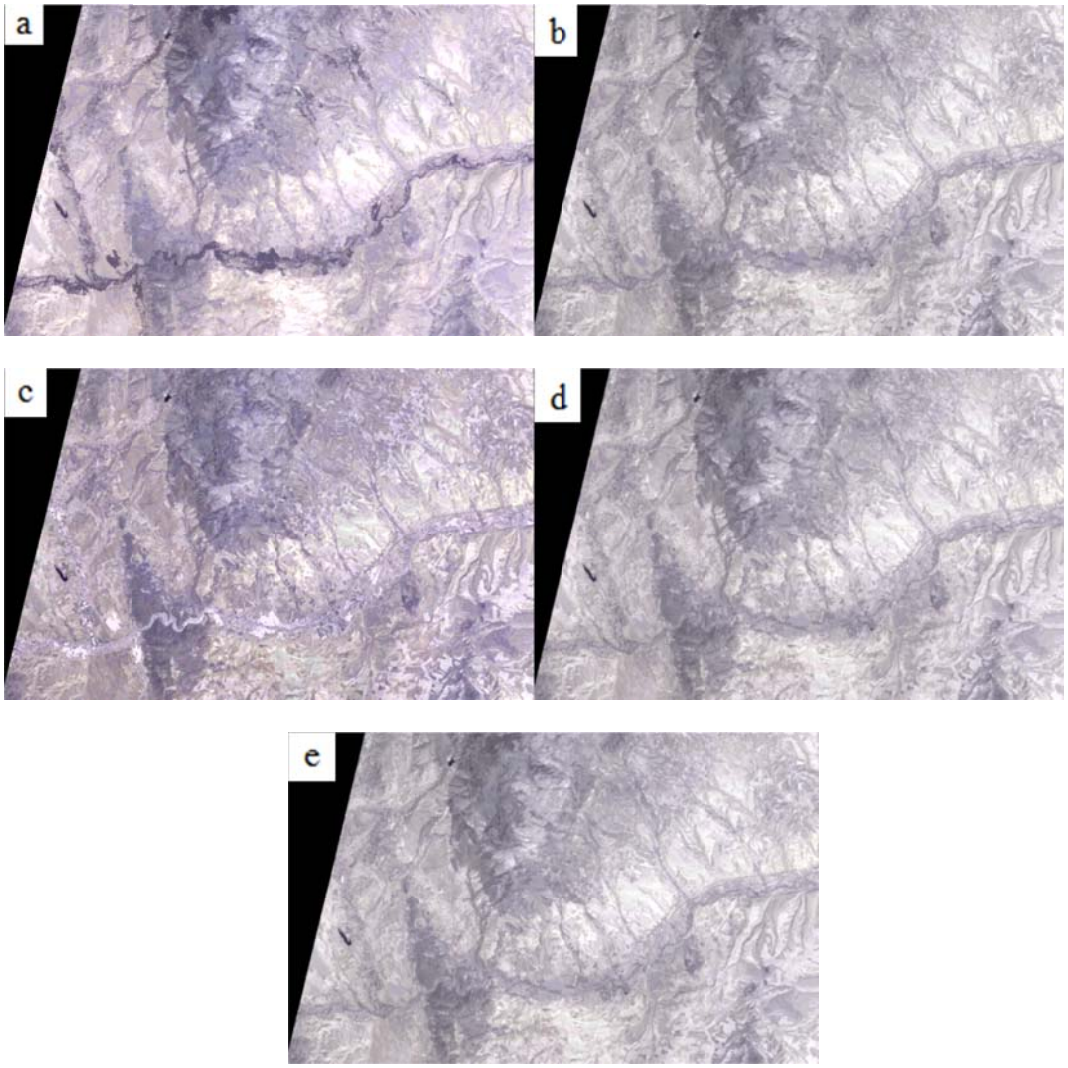

Figure 32 VNIR (3N) - SWIR (bands 7, 8, 9) fusion; a) Non-fused, b) Brovey, c) IHS, d) PCA, and e) Wavelet

In Figures 31 and 32, a visual examination of the fused images leads to the conclusion that the IHS transformation provides the best enhancement of the features through spatial improvement. The remaining three transformations, which are not as successful spatially, however, are observed to be better with respect to spectral detail. The differences among them are not clear visually, as the resolution difference between the LR and HR images is relatively small (30m to 15m).

The objective evaluation of the fused case study images are given in Tables 9 to 12. When the results for the entire selected area and the case study area, presented in Tables 5, and 7 and 8 are examined, an overall drop in spectral quality of fused TIR and SWIR images is observed. This is in line with the suggestion in part 3.2.1.1. "...to calculate the correlation coefficient for a small window instead of the entire image". However unlike CC and RMSE, ERGAS values were improved. This may be due to the selection of the case study area which has higher mean pixel values in the SWIR bands. Another change is the increase in HPCC, giving higher spatial improvement. These changes were not substantial and the status quo between the image fusion methods didn't change. PCA is still the best in spectral information preservation with the exception of CC in VNIR-SWIR fusions, while IHS is still has the highest spatial improvement. Similar conclusions are reached when the results presented in Tables 6, and 9 and 10 are compared.

Table 9 Objective evaluation of VNIR3N and TIR bands 10, 11, and 12 image fusions in first case study area, best results are in bold

	IHS	Brovey	PCA	Wavelet
CC	0.82806	0.9543	**0.9659**	0.96076
RMSE	58.8160	32.0537	**27.5154**	28.4182
ERGAS	4.5278	2.4675	**2.1182**	2.1817
HPCC	**0.99671**	0.7219	0.84929	0.87786

Table 10 Objective evaluation of VNIR3N and TIR bands 12, 13, and 14 image fusions in first case study area, best results are in bold

	IHS	Brovey	PCA	Wavelet
CC	0.83174	0.95503	**0.967**	0.96169
RMSE	60.2131	32.8886	**28.0844**	29.1203
ERGAS	4.5967	2.5096	**2.1432**	2.2221
HPCC	**0.99758**	0.72465	0.85212	0.88166

Table 11 Objective evaluation of VNIR3N and SWIR bands 4, 5, and 6 image fusions in first case study area, best results are in bold

	IHS	Brovey	PCA	Wavelet
CC	0.90191	**0.9778**	0.97678	0.97455
RMSE	28.1562	14.1999	**14.0457**	14.2498
ERGAS	7.8192	3.9165	**3.8791**	3.9363
HPCC	**0.94045**	0.64979	0.77313	0.79899

Table 12 Objective evaluation of VNIR3N and SWIR bands 7, 8, and 9 image fusions in first case study area, best results are in bold

	IHS	Brovey	PCA	Wavelet
CC	0.88393	**0.97242**	0.97184	0.96882
RMSE	30.5843	15.7523	**15.4387**	15.7998
ERGAS	8.4824	4.3372	**4.2638**	4.366
HPCC	**0.86058**	0.59535	0.68956	0.7237

Once the image fusions were done the spectral maps were created using the band equations explained in chapter 3. Figure 33 to 35 display sulphate, mafic, and hydroxyl "a" index maps of the case study area.

It is known that the riverbanks at the east side of the study area have large and easily distinguishable sulphate formations and hydroxyl bearing mineral formations. At the north-west of the centre of the study area, there is a clearly visible ophiolite outcrop originating from the NAOM elongating in the same direction. Further an alunite formation right at the centre of the spectral map.

The images here, however, are still too large to determine the differences between fused images and the non-fused image. The formations are examined in detail in the next section, second case study, in order to determine which image fusion method is the best.

The spectral index maps of the first study area were cropped to focus on the areas of interest. The parts of SI, MI, and OHIa that will be examined in detailed will be marked on the non-fused images of the spectral indices in Figures 33, 34, and 35 respectively.

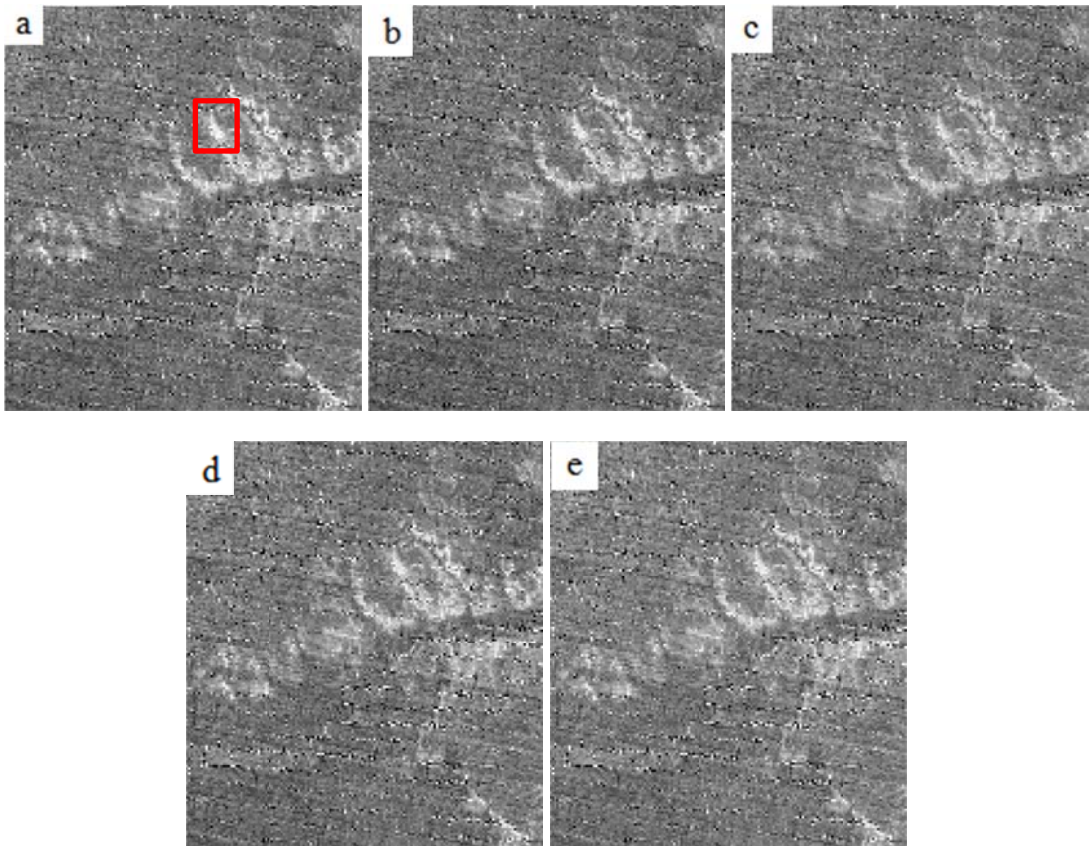

Figure 33 Sulphate Index of first case study area; a) Non-fused, b) Brovey, c) IHS, d) PCA, and e) Wavelet

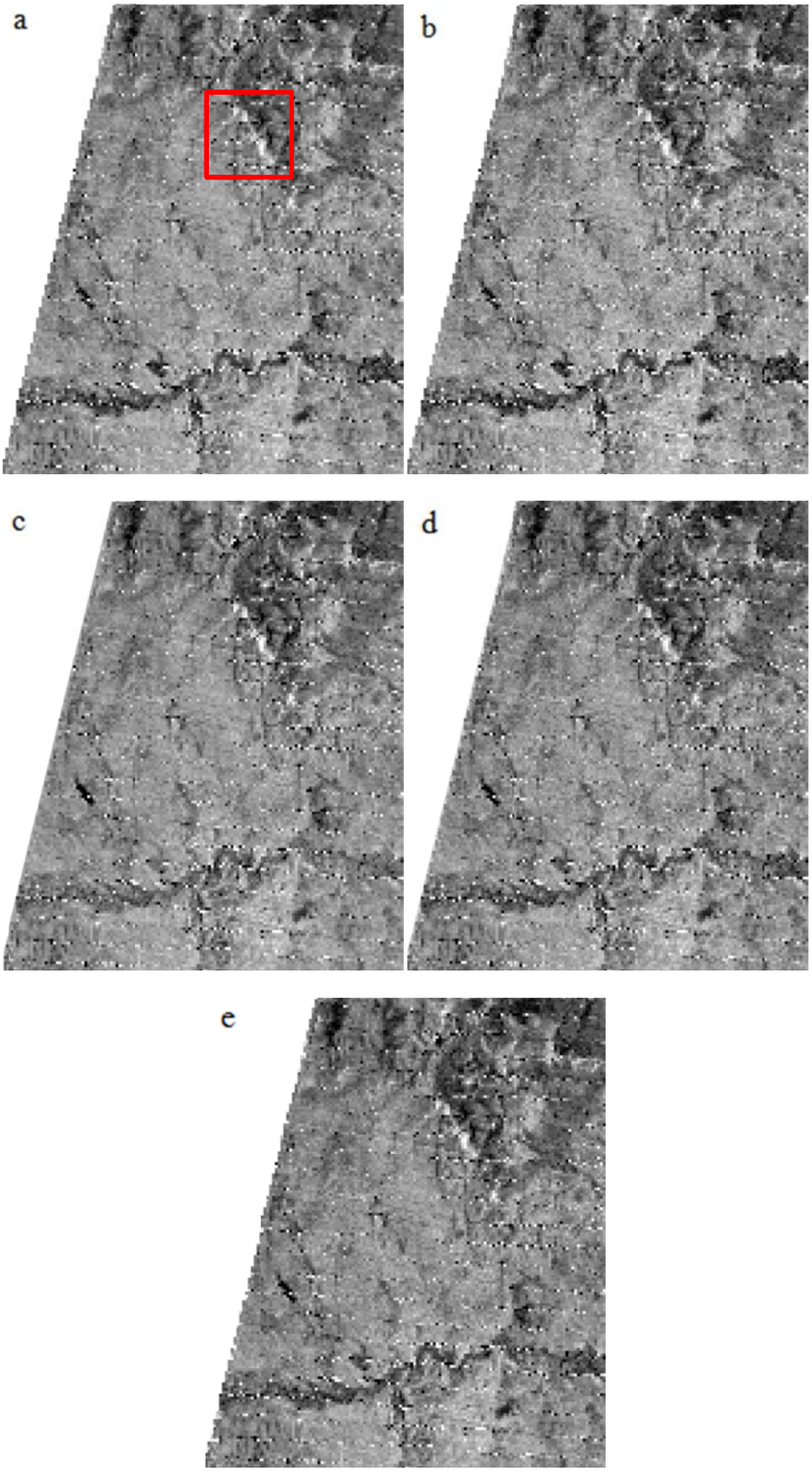

Figure 34 Mafic Index of first case study area; a) Non-fused, b) Brovey, c) IHS, d) PCA, and e) Wavelet

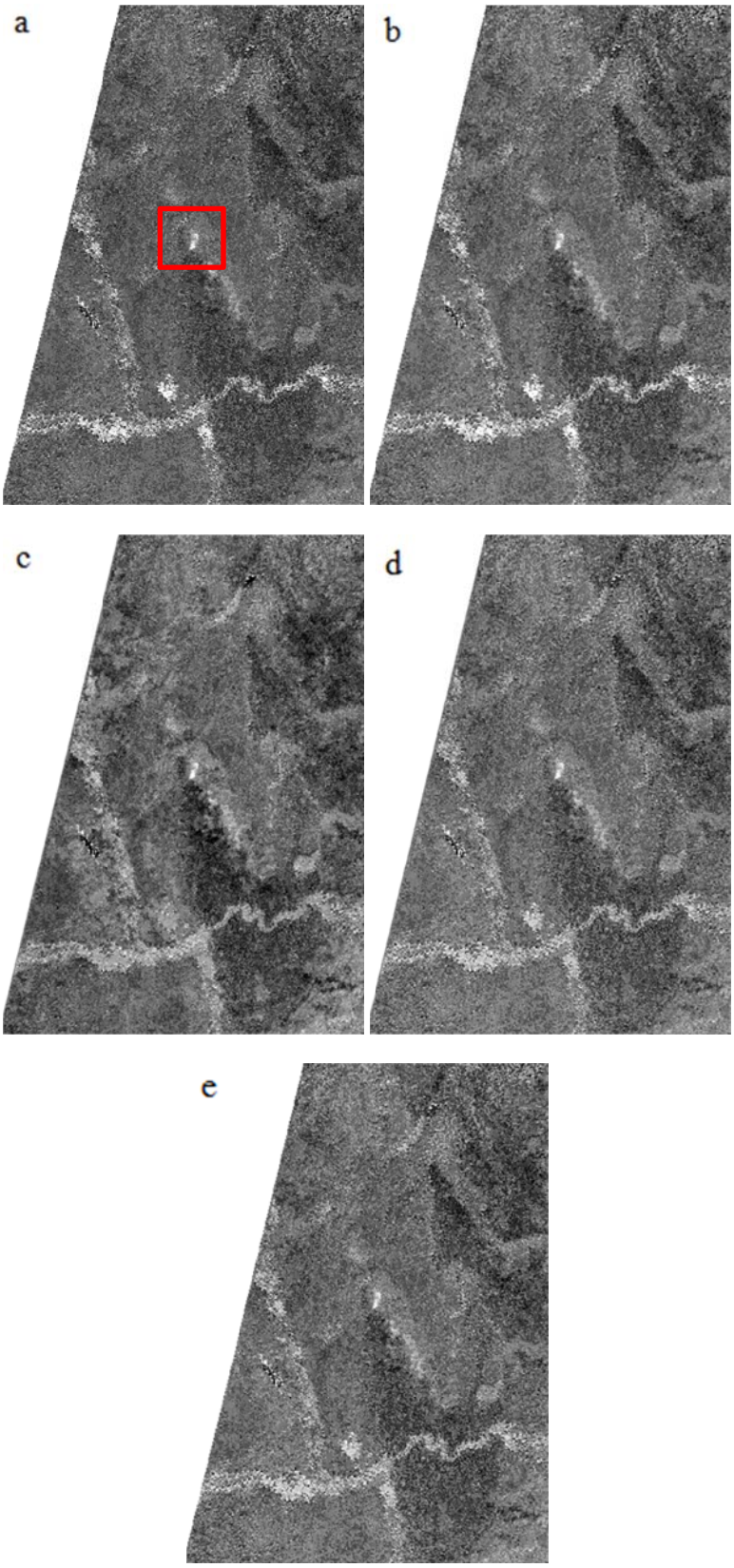

Figure 35 OHIa of first case study area; a) Non-fused, b) Brovey, c) IHS, d) PCA, and e) Wavelet

6.2. Second Case Study and In-Depth Analysis

The image fusion has clearly increased the spatial resolution of the raw spectral map as previously homogeneous pixels now comprise of different DN values. However it is noted that these newly formed pixels, using different transformations, don't always agree with each other. An example is given in Figure 36, which is taken from MI map, Figure 34, of non-fused and all fused index maps.

The four pixels, each 90 meters, in the non-fused MI map are further divided into smaller pixels, smallest being 15 meters. While Brovey and PCA create new pixels, they do not form a well-defined feature. On the other hand, it can be seen that IHS and Wavelet fused images reveal a variation not visible in the 90 meter pixels of the raw image. The feature crosses diagonally from the top left pixel to the bottom left pixel, forming softer boundary between the grey pixel at top left and the darker coloured pixel at bottom right. If carefully examined the same 90 meter pixels in Brovey and PCA have a resemblance in the background but they are buried under darker pixels.

IHS further displays higher resolution pixels with smoother transition of DN values between 90 meter pixels, resulting in the dissolving of previously distinct 90 meter pixel boundaries. From this example alone it can be said IHS has superior spatial improvement which is supported by objective evaluation results given in earlier chapters. There is however the danger of not noticing the spatial improvement of IHS on larger images by naked eye, as the smooth transitions between smaller pixels can often be perceived as homogeneous 90 meter (or 30 meter) pixels.

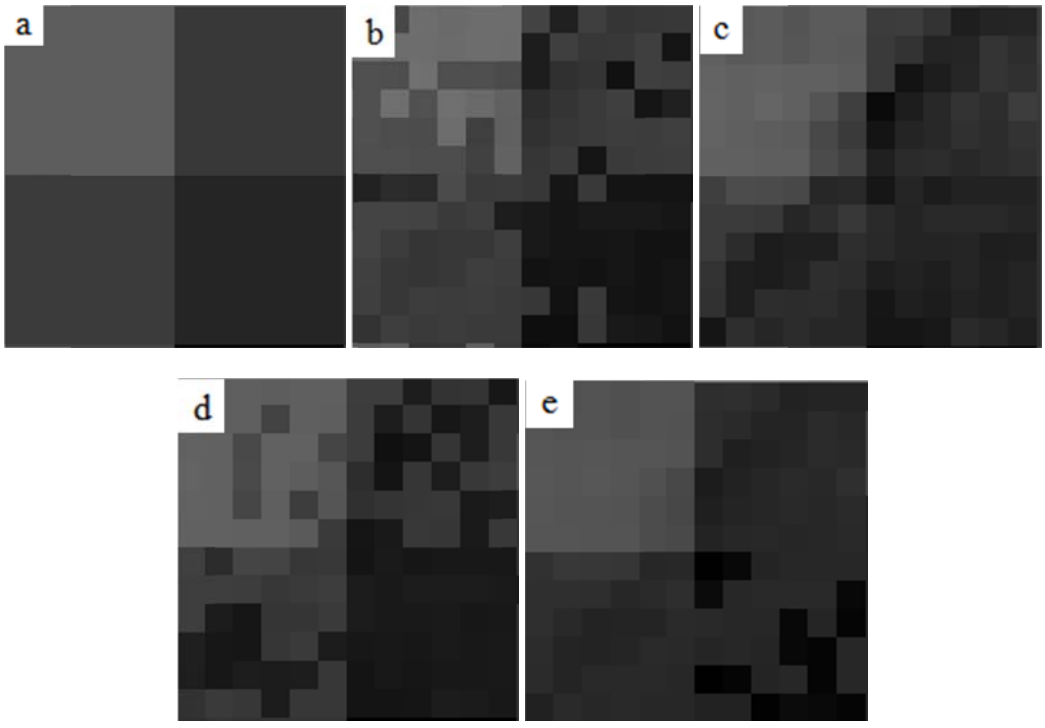

Figure 36 Four 90 meter pixel spatial improvement; a) Non-fused, b) Brovey, c) IHS, d) PCA, and e) Wavelet

As a result case study areas, where individual pixels can been seen, are required for visual accuracy assessment of image fusion methods. Thus, a second case study was prepared, focusing on the three mono mineral/rock outcrops within the first case study area. Figure 37 shows three areas chosen within the first case study area.

On Figure 37, slightly north-west of the centre of first case study area, the ophiolotic melange of NAOM can be seen in bluish tint. These ophiolitic rocks are expected to be seen as light coloured pixels in mafic index spectral map. Further, while not visible on colour composite map, gypsum formations are present at the northern side of the Kızılırmak River at the east end of the case study area. Sulphate index map is expected to detect these features. Finally bentonite is seen in light bluish tints and at a bentonite quarry to the west of the map. These features will be revealed with OHIa spectral index.

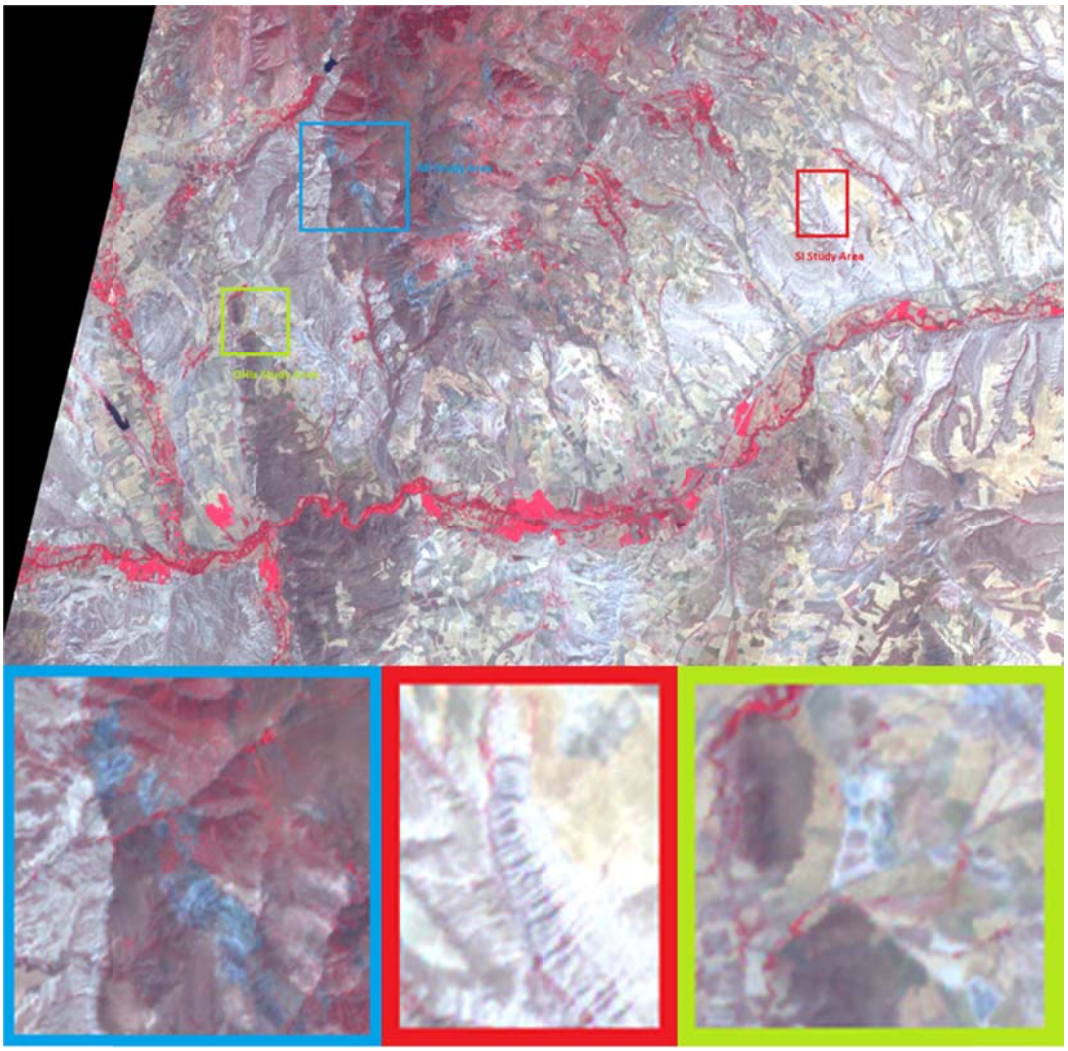

Figure 37 Location and close up of the second case study areas within first case study area; MI (blue), SI (red), and OHIa (green) study area (VNIR 3N, 2, 1)

Same procedures of pre-processing were applied on each VNIR, SWIR and TIR bands of the isolated SI, MI, and OHIa study area images. All four image fusion methods used in this study were applied to the second case study areas. The fused images can be seen in Figures 38 to 41.

The objective evaluations of the fused SI, MI, and OHIa case study images are given in Tables 13 to 16. The most notable feature of the new fusions were that SI and MI case study areas compared to the first case study area is the major drop in spectral data preservation and increase in spatial resolution improvement. This is due to the smaller areas selected for the second case studies and the difference of spatial resolution between TIR and VNIR bands.

In Figures 38 and 39, the TIR images have almost no distinguishable geographic features while VNIR images displays quite a bit of them. Hence image fusion is expected to change most of the spectral information in TIR images in favour of adding spatial information from VNIR images. The result can be seen both in objective evaluation results and visual examination. CC values drop significantly and RMSE values increase, yielding poorer results for preservation of spectral information. Unlike first case study, ERGAS values this time followed other spectral evaluations and showed increased values. The cause of this is again attributed to the change in mean pixel value of the selected areas. Wavelet fusion provided highest spectral preservation among all methods. HPCC gave higher values for Brovey, PCA, and Wavelet. IHS this time displayed minor decrease in spatial improvement, getting marginally lower values than PCA.

In Figures 40 and 41, there is a human made bentonite quarry site that has a clear shape in VNIR image while not visible in SWIR images. Image fusion's effectiveness in improving spatial resolution is evident as all fused images reveal the quarry site. Preservation of spectral information, the fused SWIR images do not show the significant decrease in spectral evaluations as in fused TIR images. The changes in objective evaluation values mirror the change from original study area to the first case study area. Again as in fused TIR images, Wavelet fusion has the highest spectral evaluation values. This is possibly the result of the fusion rule "mean" performing better in smaller areas. IHS, while suffering in HPCC values, still performs best in spatial improvement. The difference between fusion methods' spatial improvement got significantly smaller.

After seeing these low spectral evaluation values a question must be asked. Was the spectral information in TIR and SWIR images lost during fusion? The answer to this question is given in spectral index maps in the following sections.

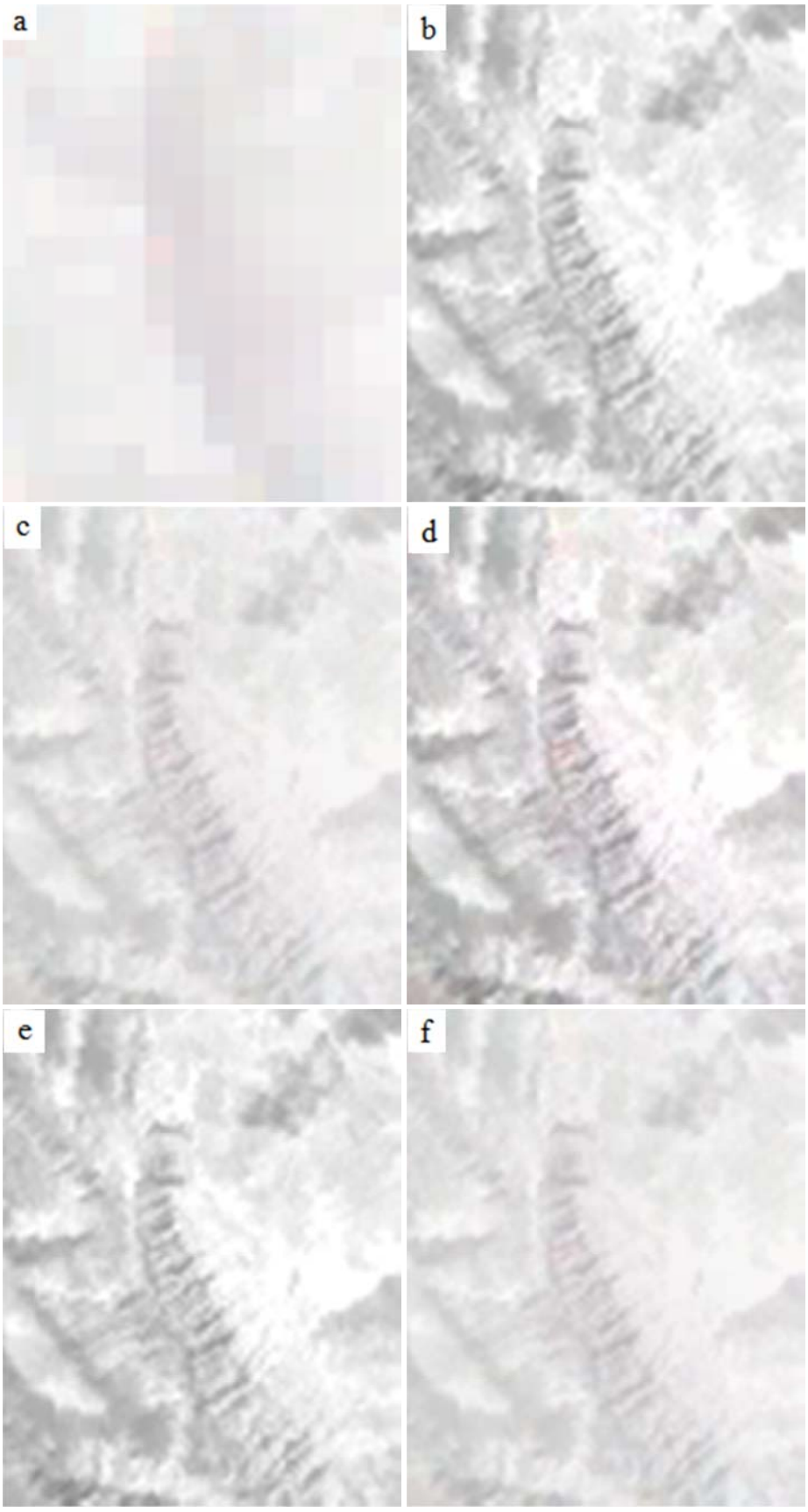

Figure 38 Sulphate Index study area; a) non-fused TIR (bands 10, 11, 12), b) non-fused VNIR3N, fused images of c) Brovey, d) IHS, e) PCA, and f) Wavelet

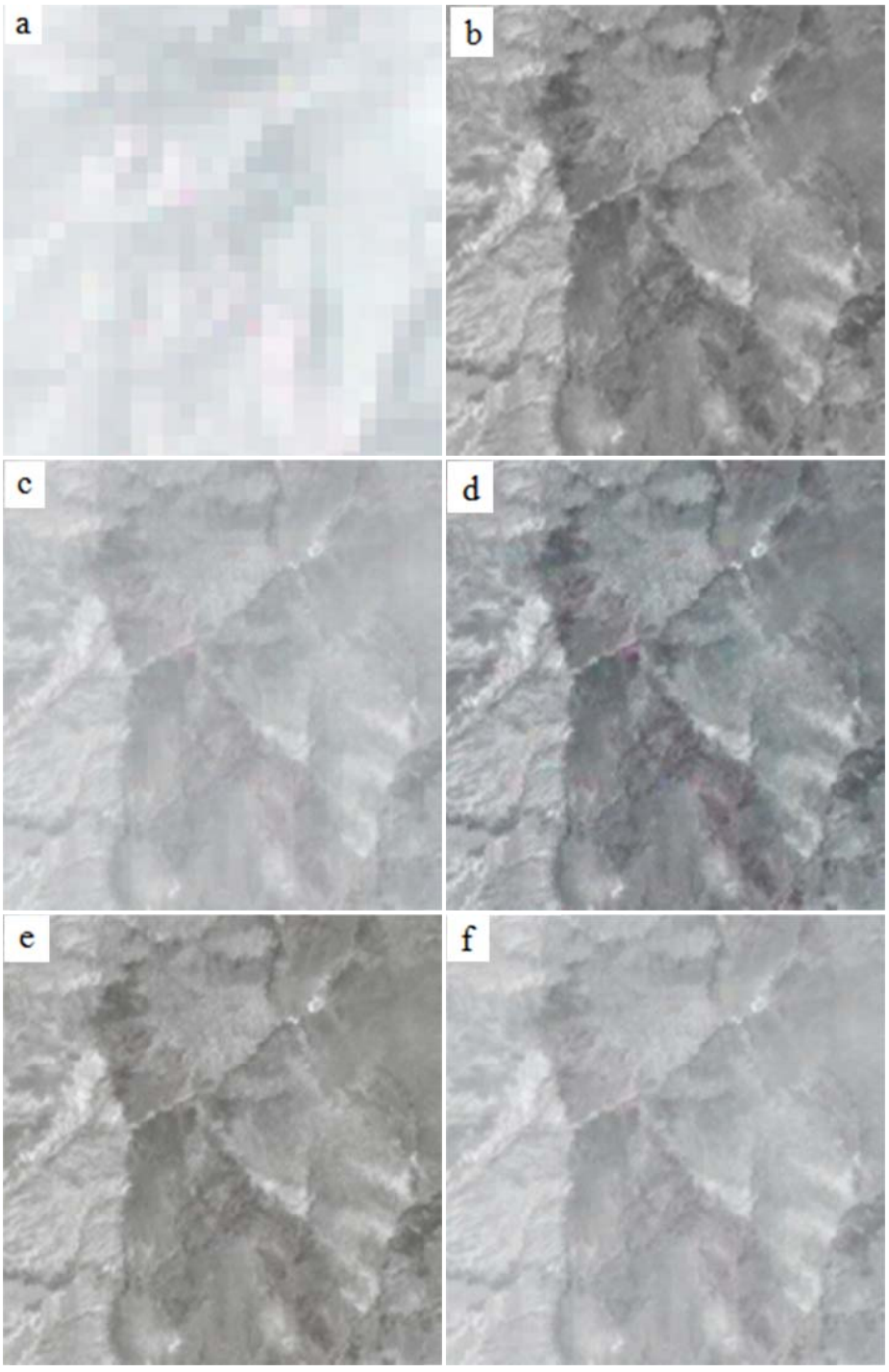

Figure 39 Mafic Index study area; a) non-fused TIR (bands 12, 13, 14), b) non-fused VNIR3N, fused images of c) Brovey, d) IHS, e) PCA, and f) Wavelet.

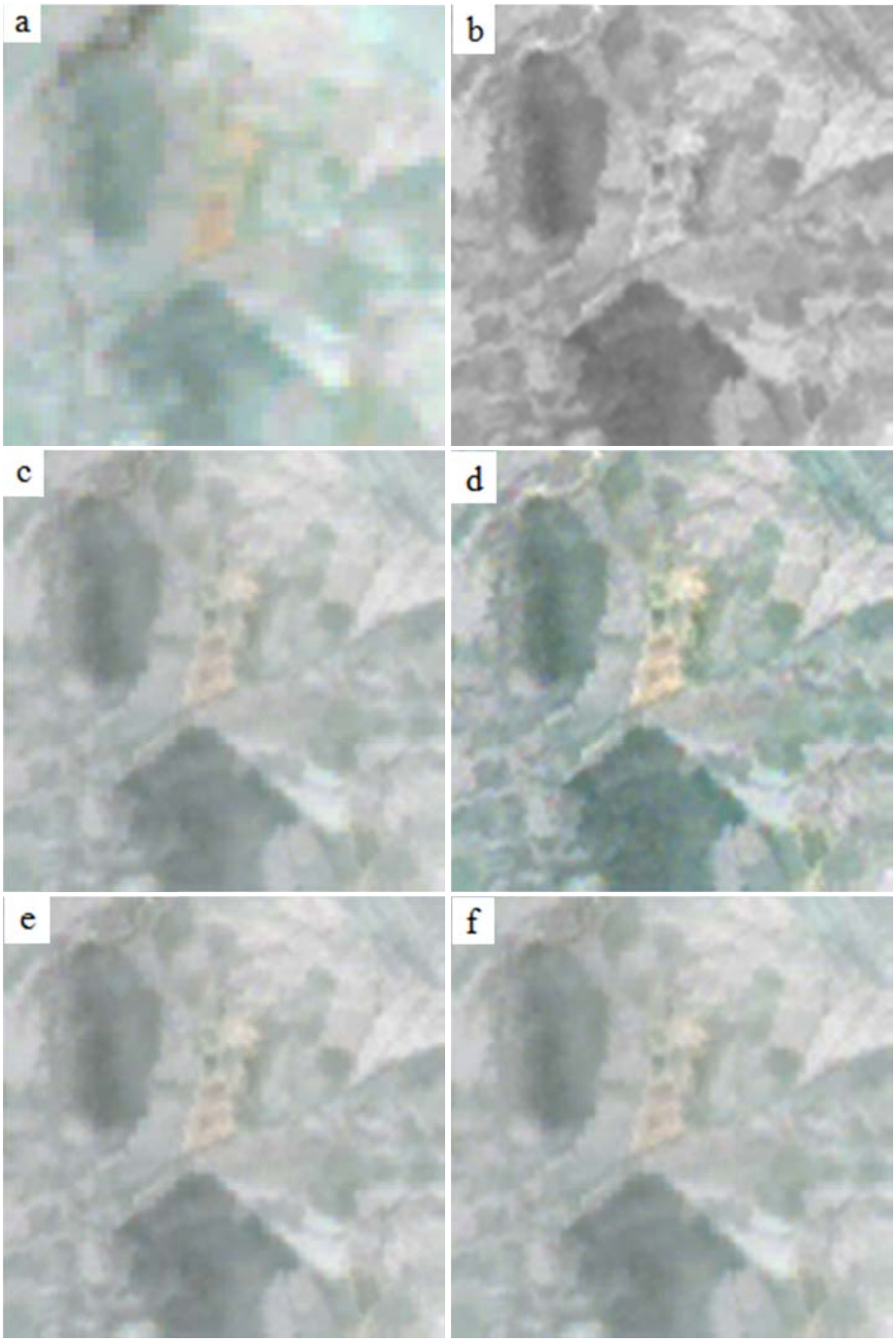

Figure 40 OHIa Index study area; a) non-fused SWIR (bands 4, 5, 6), b) non-fused VNIR3N, fused images of c) Brovey, d) IHS, e) PCA, and f) Wavelet.

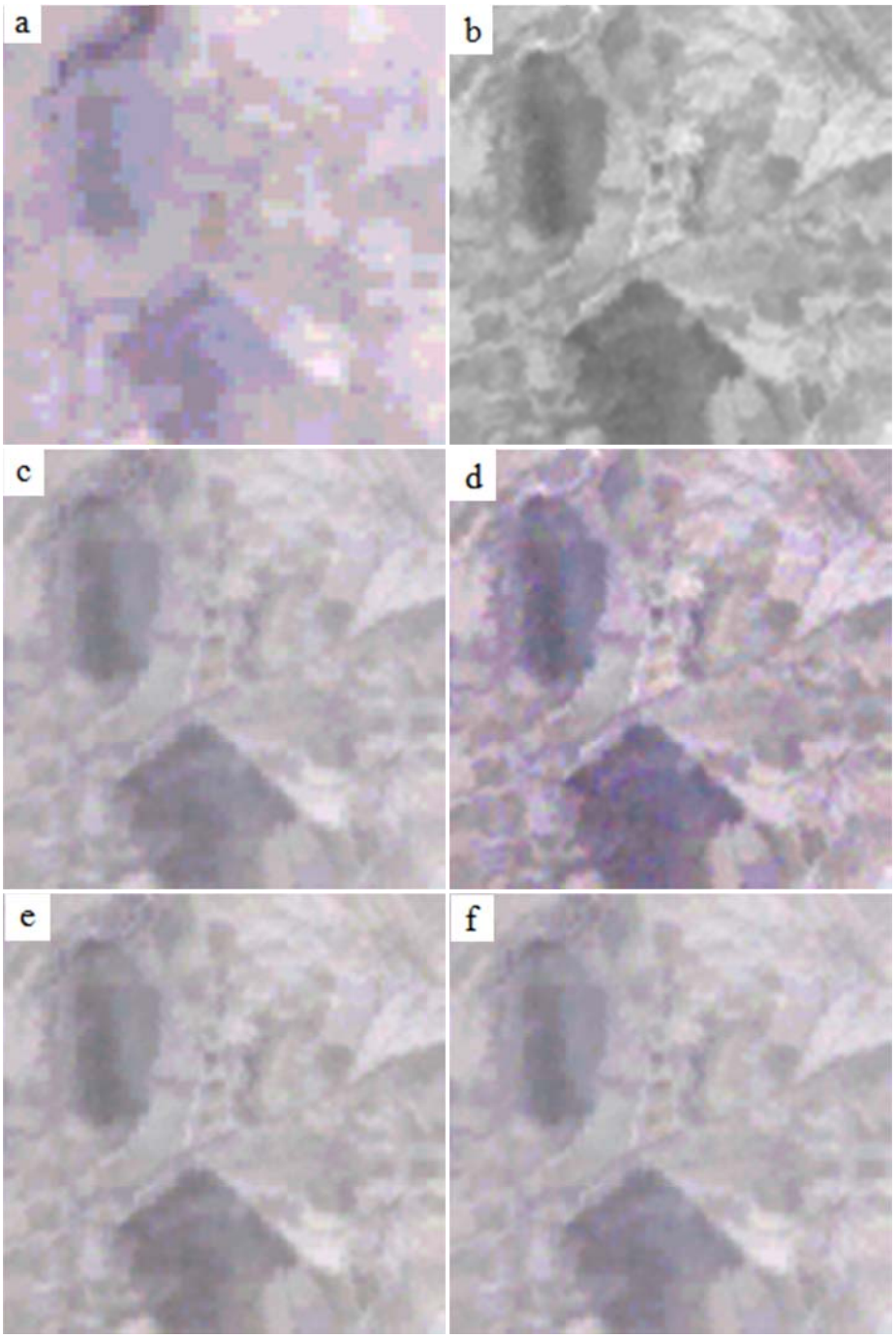

Figure 41 OHIa Index study area; a) non-fused SWIR (bands 7, 8, 9), b) non-fused VNIR3N, fused images of c) Brovey, d) IHS, e) PCA, and f) Wavelet.

Table 13 Objective evaluation of VNIR3N and TIR bands 10, 11, and 12 image fusions in Sulphate Index study area, best results are in bold

	IHS	Brovey	PCA	Wavelet
CC	0.021184	0.2261	0.046543	**0.24205**
RMSE	27.6499	14.552	28.1019	**13.7595**
ERGAS	1.9667	1.0349	1.9988	**0.97858**
HPCC	0.99756	0.98468	**0.99968**	0.98405

Table 14 Objective evaluation of VNIR3N and TIR bands 12, 13, and 14 image fusions in Mafic Index study area, best results are in bold

	IHS	Brovey	PCA	Wavelet
CC	0.26664	0.45201	0.24564	**0.54939**
RMSE	78.7001	44.3547	71.1353	**39.1546**
ERGAS	5.8405	3.288	5.2715	**2.9027**
HPCC	0.99606	0.9721	**0.99786**	0.94871

Table 15 Objective evaluation of VNIR3N and SWIR bands 4, 5, and 6 image fusions in OHIa Index study area, best results are in bold

	IHS	Brovey	PCA	Wavelet
CC	0.76187	0.90826	0.89473	**0.91325**
RMSE	24.223	13.303	14.0439	**12.5877**
ERGAS	6.4156	3.4852	3.6731	**3.2983**
HPCC	**0.92448**	0.8207	0.84774	0.80919

Table 16 Objective evaluation of VNIR3N and SWIR bands 7, 8, and 9 image fusions in OHIa Index study area, best results are in bold

	IHS	Brovey	PCA	Wavelet
CC	0.67839	0.8586	0.81742	**0.867**
RMSE	27.0083	15.0614	16.9165	**14.2244**
ERGAS	7.1199	3.9252	4.4016	**3.7114**
HPCC	**0.83203**	0.7478	0.82308	0.72768

6.2.1. Sulphate Index Case Study

The sulphate spectral index maps are displayed in Figures 42 to 46. Sulphate was detected in a much larger area as seen in previous SI maps, however this small section displays the power of image fusion.

Brovey and PCA fused SI maps all show that the areas with white and light coloured pixels are not perfect gypsum outcrops when the 90 meter pixels are divided into 15 meter pixels. A large number of smaller pixels in the previously homogenous white 90 meter pixels display darker coloured pixels, showing that these areas are not as homogenous as the non-fused SI shows us.

IHS goes one step ahead of the other three methods and displays a geological feature not seen in the raw SI and even in other image fusion SI maps. The smooth transitions of DN values in pixels also give more accurate information on how the gypsum is distributed in the homogeneous 90 meter pixels of the non-fused SI.

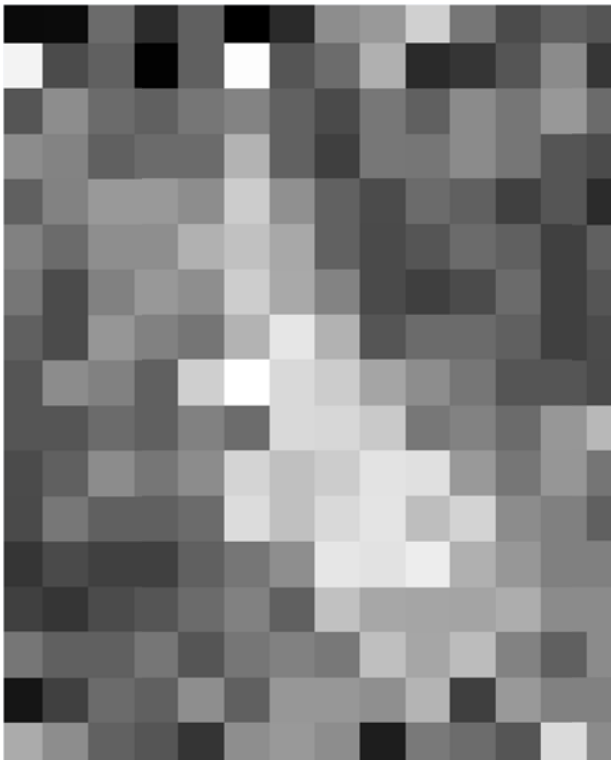

Figure 42 Non-fused SI map

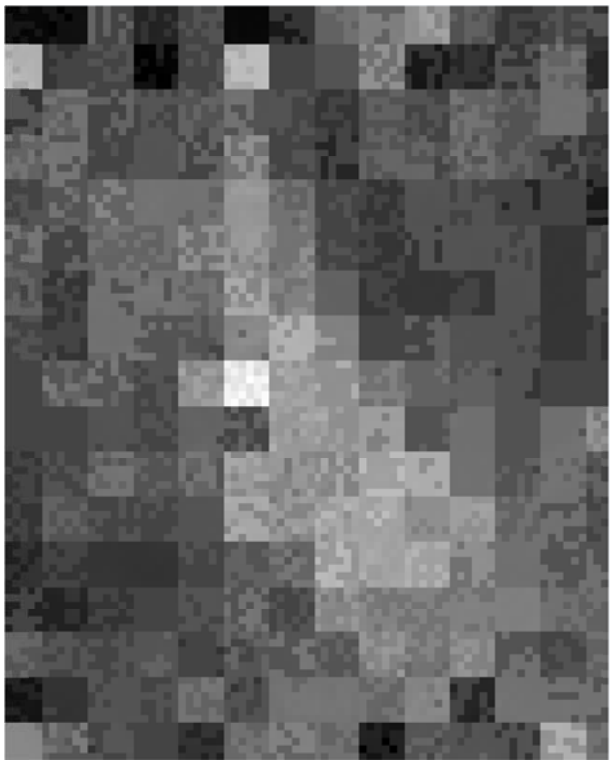

Figure 43 SI map done with Brovey

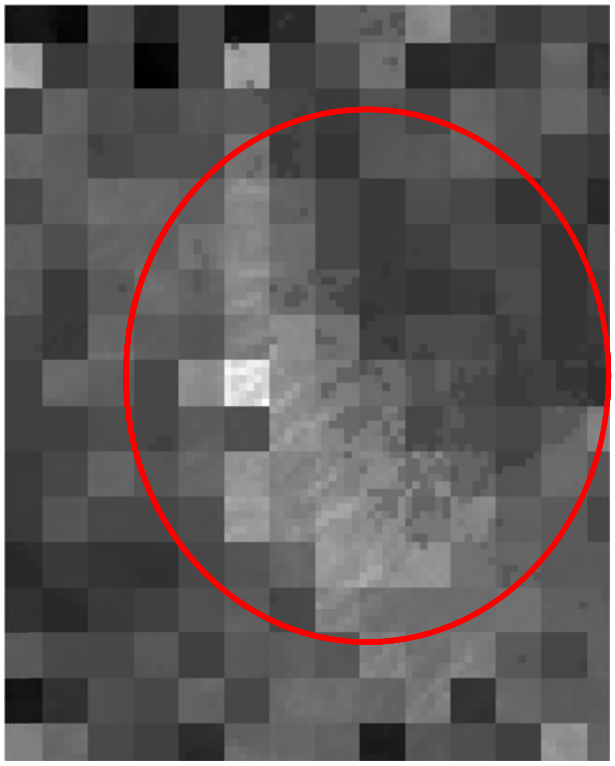

Figure 44 SI map done with IHS

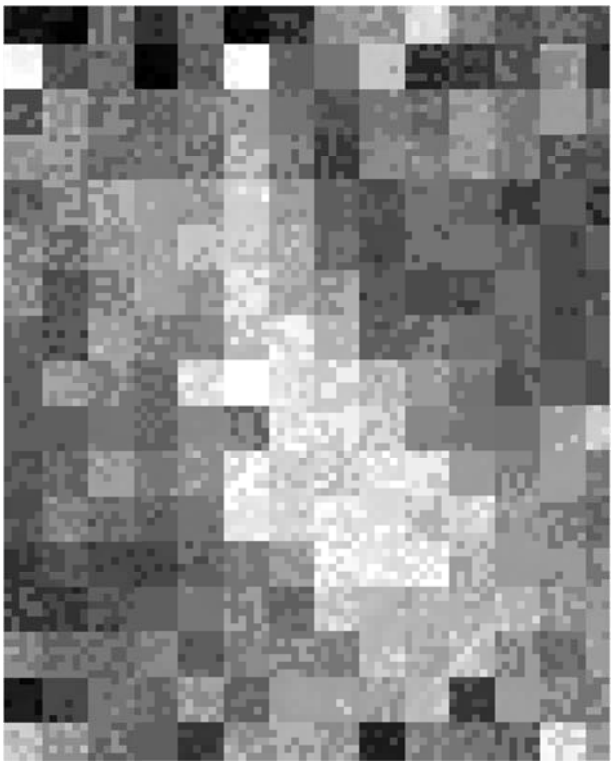

Figure 45 SI map done with PCA

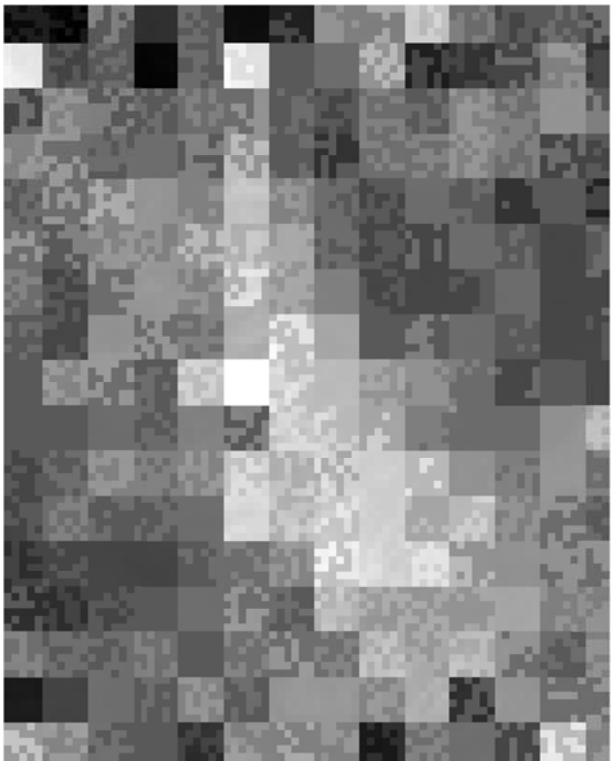

Figure 46 SI map done with Wavelet

6.2.2. Mafic Index Case Study

The ophiolite outcrop is visible in both non-fused and fused mafic spectral index maps in Figures 47 to 51 as light coloured pixels elongating North West to South East.

IHS displays clear geological features that are barely visible in the non-fused MI image. Even smooth transitions between 90 meter pixels are present, concealing the 90 meter pixels inherent from the TIR image. However, the level of spatial improvement is still not sufficient and the 90 meter pixels can still be distinguished by naked eye despite being divided to 15 meter pixels. Obviously, even the 15 meter resolution is somewhat rough.

Wavelet transformation comes close to IHS transformation's level of spatial improvement in some pixels; but overall it fails to display the features as clearly as IHS does. Brovey and PCA are able to create 15 meter pixels and provide some sense of spatial improvement; however, this improvement is not comparable to that of the IHS transformation.

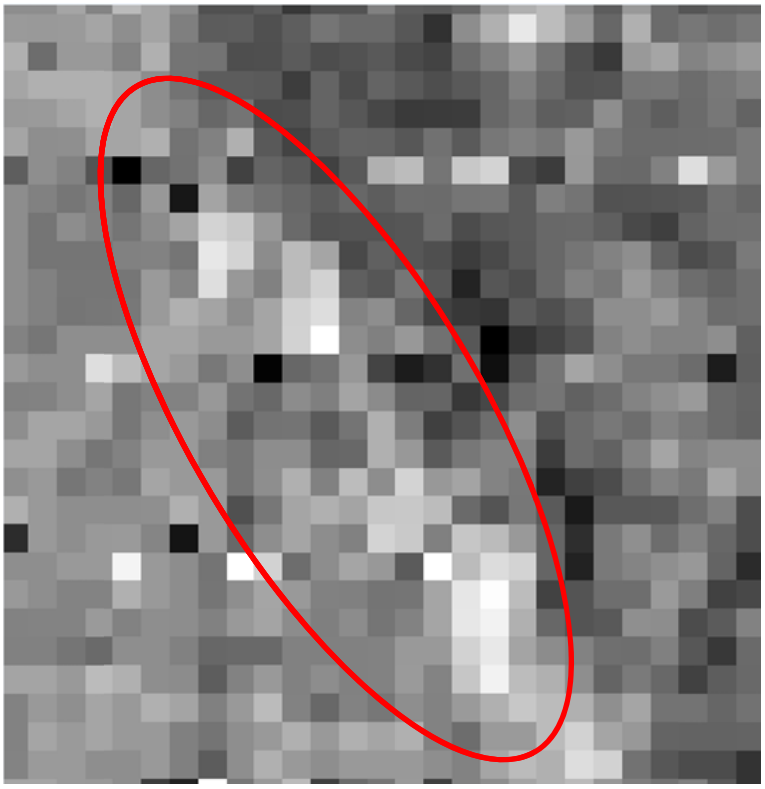

Figure 47 Non-fused MI map

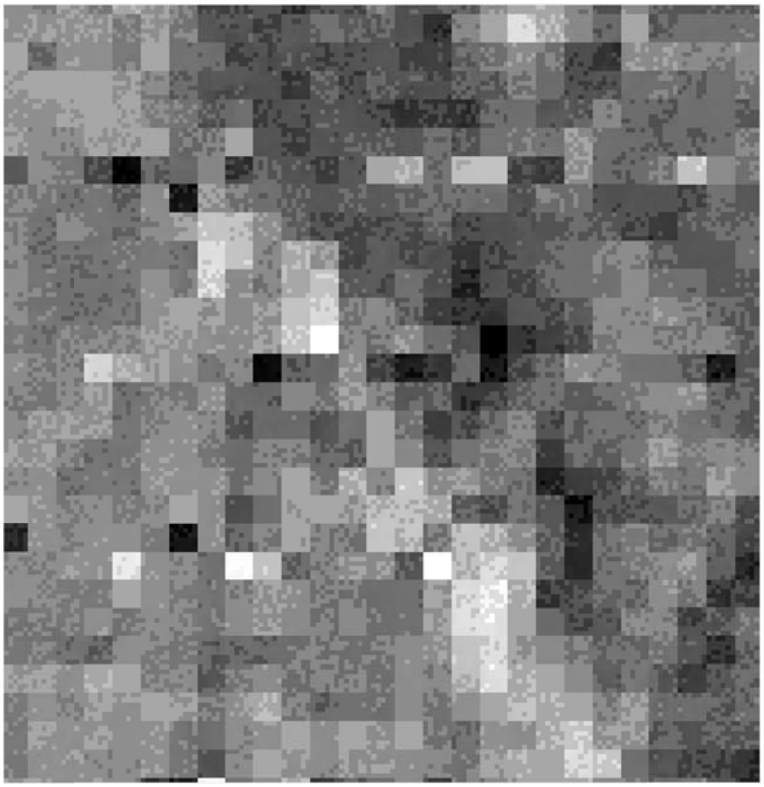

Figure 48 MI map done with Brovey

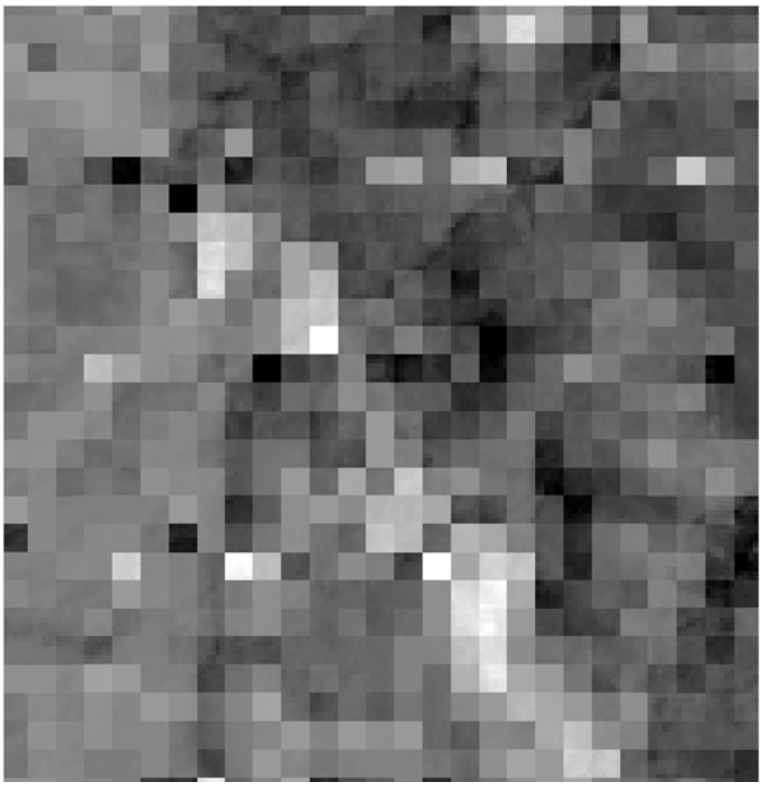

Figure 49 MI map done with IHS

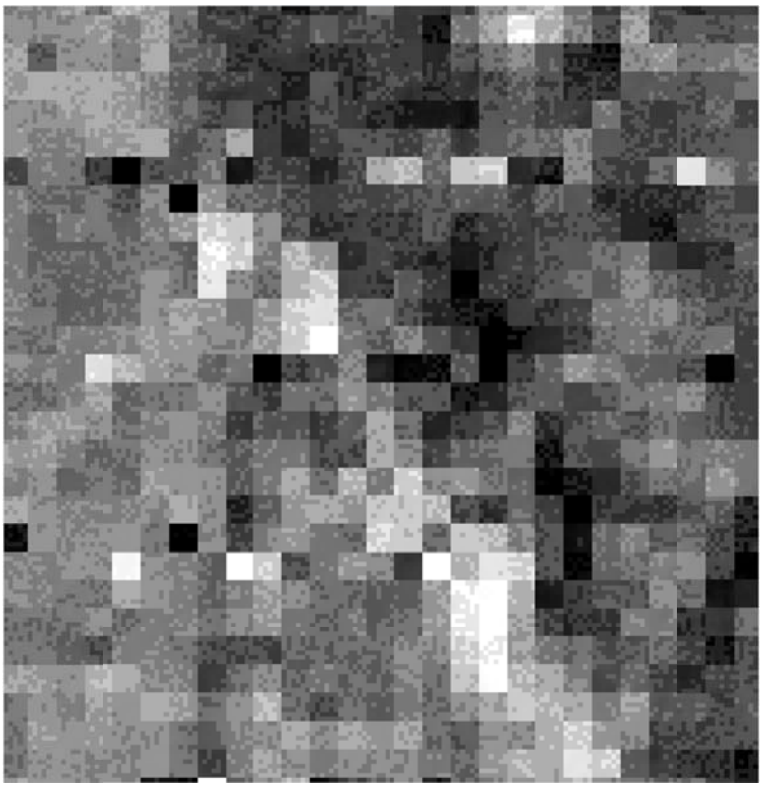

Figure 50 MI map done with PCA

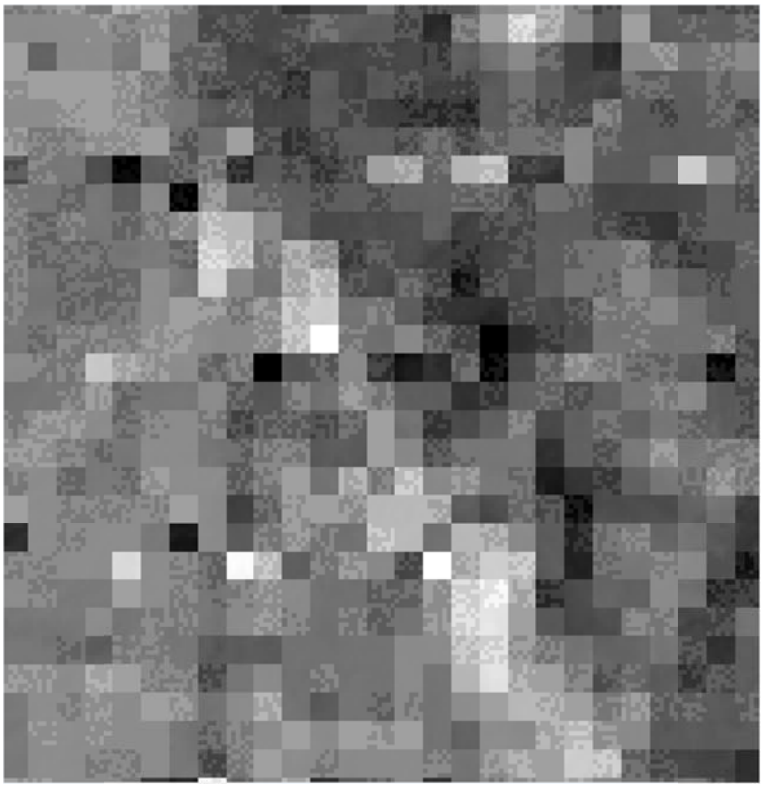

Figure 51 MI map done with Wavelet

6.2.3. OHIa Case Study

OHIa maps shown in Figures 52 to 56 are different than the previous MI and SI images. This is a result of using the 30 meter pixel size SWIR images instead of the 90 meter pixel size TIR images. The second factor is that the bentonite quarry in the OHIa study area is mono-mineral as the bentonite ore is placed tightly together. As a result the light coloured pixels at the bentonite quarry site are expected to be homogeneous.

The first noticeable difference is that, now, it is more difficult to differentiate Brovey, PCA, and Wavelet images from the non-fused image. Closer examination shows that these fusion methods do produce 15 meter pixels that are very similar to the smooth transition that IHS produced in TIR spectral indices. However, they are not clear without zooming in.

The spatial improvement in Brovey, PCA, and Wavelet fused images are not as impressive as in TIR spectral indices, as the ratio of resolution between HR and LR images have been reduced by a factor of three. This is supported in the objective evaluation results as HPCC values are lower in SWIR fusions compared to TIR fusions. IHS produces marginally better results as its spatial improvement is greater than the other methods, as has been displayed in the objective evaluation results.

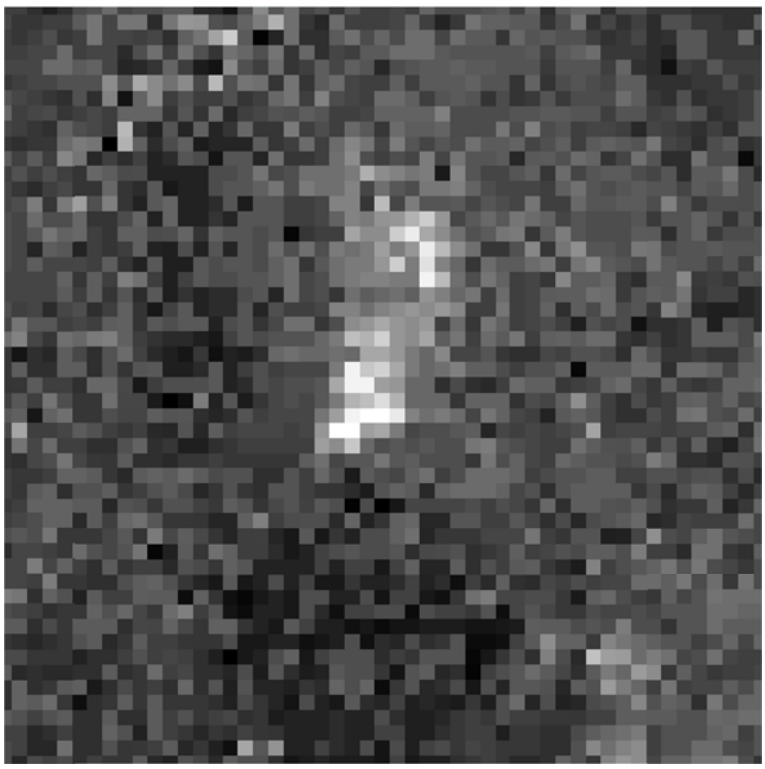

Figure 52 Non-fused OHIa map

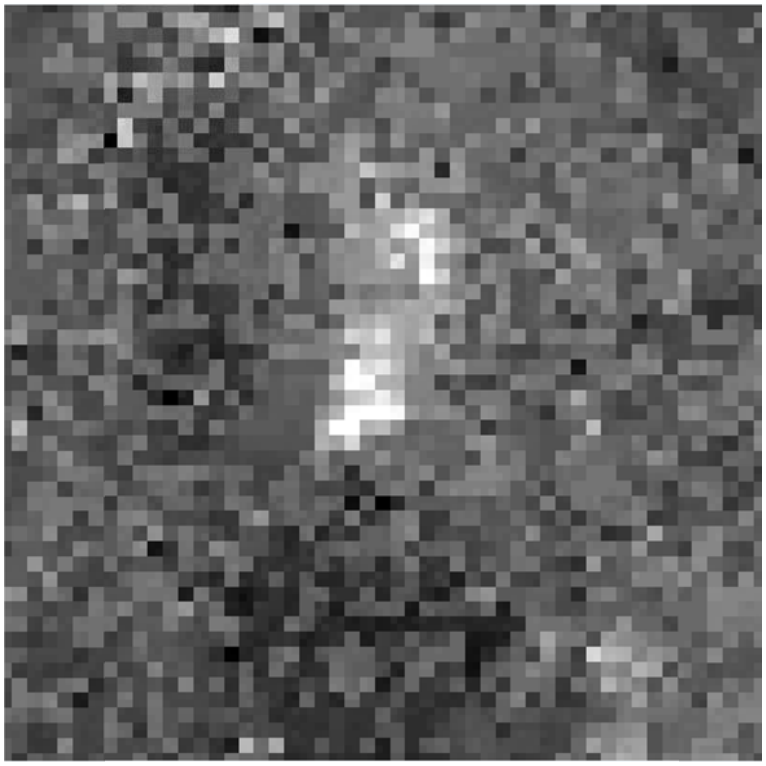

Figure 53 OHIa map done with Brovey

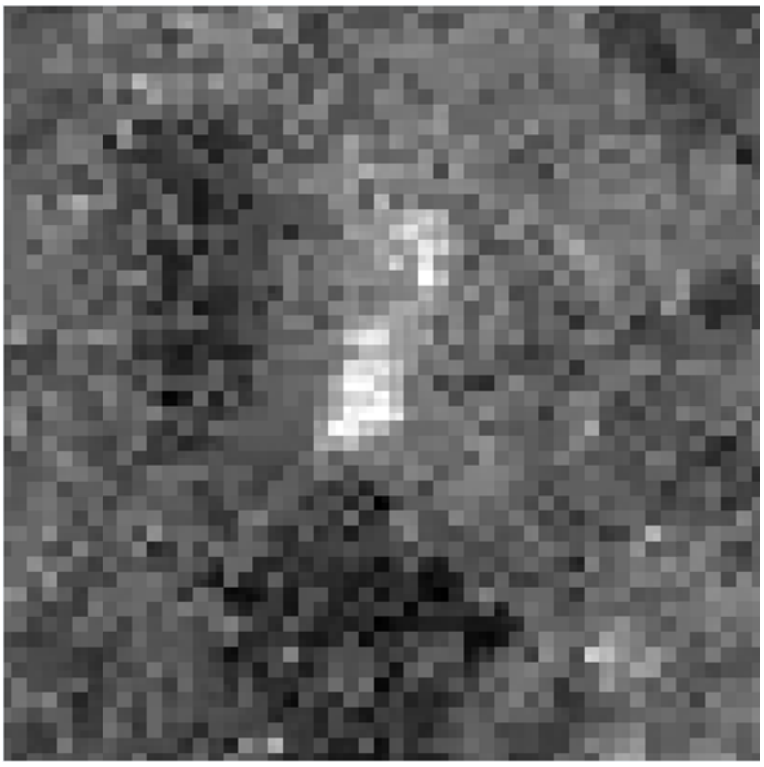

Figure 54 OHIa map done with IHS

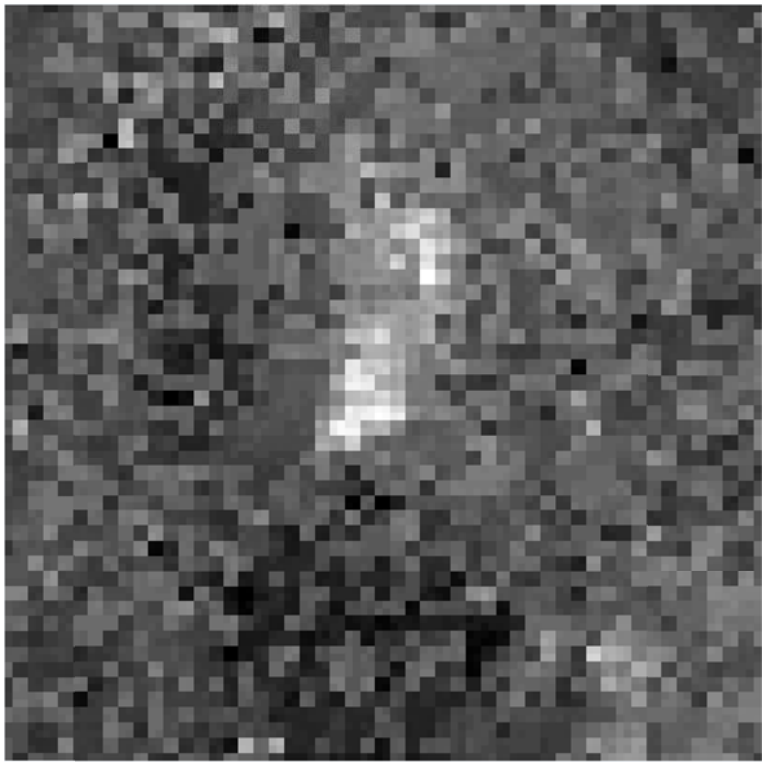

Figure 55 OHIa map done with PCA

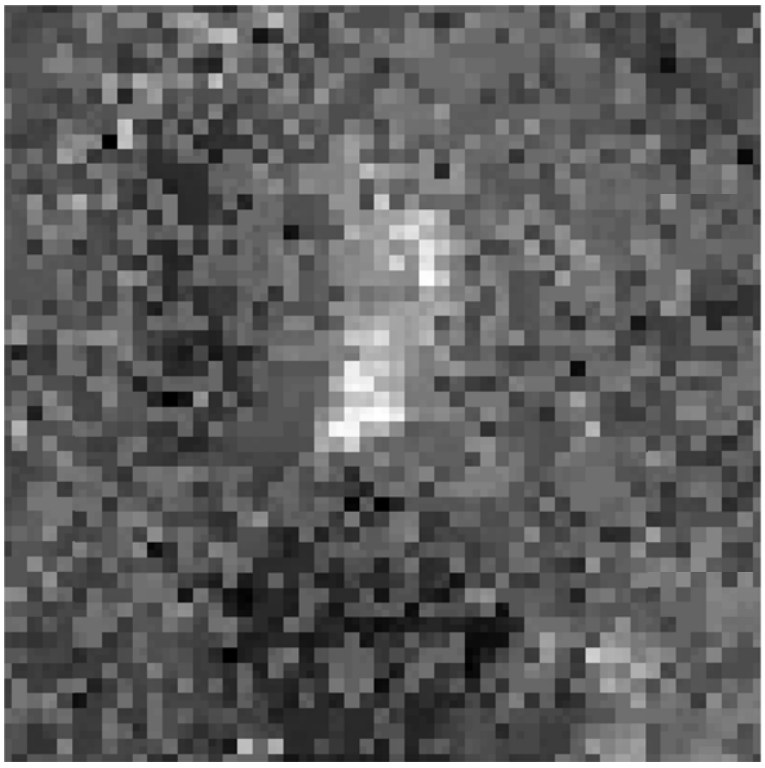

Figure 56 OHIa map done with Wavelet

CHAPTER 7

DISCUSSION AND CONCLUSION

7.1. Discussion

One of the common uses of image fusion is pan-sharpening which is used to fuse the panchromatic images with the visible multispectral band images in remote sensing applications. A large number of such applications can be found in literature, in which various methods of image fusion have been used and their performances are compared to find the best method. A close look into the literature, however shows that a similar approach to the fusion of thermal and shortwave infrared images have not received much attention. This study aims to contribute to literature with regard to the use of image fusion to improve the spatial resolution of thermal infrared and shortwave infrared images as distinct from ordinary pan-sharpening applications.

To test the image fusion's effectiveness a study area from Çankırı was chosen. Satellite images from all ASTER bands were used for the study. For this purpose a GUI was developed using MATLAB and its toolboxes. Four distinct image fusion methods, IHS, PCA, BT, and WT were picked for their common use in literature and reliability. The methods were, in general, successful in increasing 90 meter and 30 meter spatial resolutions to 15 meter resolution and maintain multispectral image properties with relatively minor loss according to objective evaluation. The increase in spatial resolution is not only observed by objective evaluation but also evident to naked eye view when images are zoomed in for a closer view as displayed in the case study.

Before the image fusion process, the images were imported out of the HDF file, and then were subjected to pre-processing. Emissivity data was converted into reflectance according to the information provided in metadata. Additionally recalibration of TIR bands was done to remove the known sensor related errors in them. Each one of the TIR and SWIR images were then resampled to the size of VNIR bands for the image fusion. After image fusions were performed, objective evaluation results were obtained and spectral index maps were produced from the fused image bands.

Same procedures were applied on a smaller parts of the study area in a case study, since the entire study area was too large to notice most of the details regarding spatial improvement and preservation of spectral information. Smaller case study areas selected the images were examined down to individual pixels. In the second case study Sulphate, Mafic, and OHIa index case study areas were used to show the differences between fused images in detail.

The overall spatial resolution increase in IHS fused images is substantial and visible to the naked eye as it is possible to see formations, which are vague or not visible in the original index maps and index maps obtained by the other fusion methods. These details are supported by the high HPCC results obtained in the evaluation results. However, spectral objective evaluation results of CC, RMSE, and ERGAS were relatively poor when compared to those of the other methods. In spectral index maps, it was noted that there was some losses of spectral information for TIR and SWIR bands, as some pixel values of the fused images and the original images did not match. Most of the apparent loss of spectral information can be attributed to dispersion of previously homogeneous 90 or 30 meter pixels into smaller 15 meter pixels with diverse values.

PCA and BT performed better in preserving spectral information, matching the original TIR and SWIR bands very closely. However their spatial correlation with VNIR bands was less than the other methods. As stated in chapter 3, loss of spectral information is unavoidable when increasing spatial resolution. Objective evaluation shows how close the fused image is to the multispectral image in terms of spectral information rather than the ground truth. Increase in spatial resolution is bound to deteriorate spectral information since a perfect spectral preservation means there is no spatial improvement. The four pixel example in case study shows us that BT and PCA do divide 90 meter pixels into 15 meter pixels but the newly formed pixels do not form coherent shapes as IHS does, which displays the lack of spatial improvement.

WT provided a good balance of both spatial resolution improvement and spectral information preservation even though it is not the best in either case. Its resolution improvement is greater than both BT and PCA, but lower than IHS. On the other hand, it preserves spectral information to a higher level when compared with IHS.

Image fusion is a valuable tool for improving the spatial resolution of image data. Despite loss of some resolution detail and spectral information, better separation of ground material without using superior thermal infrared images from other platforms and satellites was shown to be possible. In this study image fusion was used with shortwave, thermal infrared and visible near infrared bands. Yet this is a relatively unexplored practice in literature, thus further exploration of possibilities with different methods and images from different satellites may be pursued.

7.2. Future Work

It should be noted that Wavelet image fusion can use different fusion rules other than "mean" used in this study. It may be possible to get even better results from Wavelet transformation by choosing a fusion rule appropriate for the image used or creating an entirely new rule to meet desired specifications. For future studies it is recommended that more image fusion methods should be tested with thermal images from different satellites. An interesting application would be the use of even higher spatial resolution images than VNIR bands of ASTER bands in improving the TIR and SWIR bands.

7.3. Conclusion

This study shows that IHS provides the best spatial improvement among the image fusion techniques presented. IHS will reveal hidden details of the low resolution images at the cost of losing some spectral information. Wavelet and PCA transform on the other hand has less spatial resolution improvement but preserve spectral information of lower resolution images used in fusion better. Despite being very close to each other, WT has more inputs and types, hence it has great flexibility and the chance to fine tune image fusion.

From the point of view of improvement in spatial resolution and minimization of spectral information loss and flexibility, WT comes out to be a compromise choice among the four methods used in an overall sense. If improvement of spatial resolution of images is to be emphasized, IHS is proposed as the image fusion method to be used.

REFERENCES

Agam, N., Kustas, W.P., Anderson, M.C., Li, F. and Colaizzi, P.D. (2007). Utility of thermal sharpening over Texas high plains irrigated agricultural fields. Journal of Geophysical Research 112.

Aiazzi B., Baronti S., Garzelli A., Santurri L, Selva M., (2005). Spatial Enhancement of TIR ASTER Data via VNIR Images and Generalized Laplacian Decomposition, Proceedings of 4th EARSel Workshop on Imaging Spectroscopy.

Al-Wassai F. A., Kalyankar N. V., Al-Zuky A. A. (2011). Arithmetic and Frequency Filtering Methods of Pixel-Based Image Fusion Techniques, IJCSI Journal, Volume 8, Issue 3, No 1.

Al-Wassai F. A., Kalyankar N. V., Al-Zaky A. A. (2012). Spatial and Spectral Quality Evaluation Based on Edges Region of Satellite, Second International Conference on Advanced Computing & Communication Technologies, pp.265-275.

Al-Wassai, Kalyankar. (2012) A Novel Metric Approach Evaluation for the Spatial Enhancement of Pansharpened Images, International Conference of Advanced Computer Science & Information Technology (ACSIT-2012), Chennai, India.

ASTER GDS. (2010). Retrieved 08 07, 2013, from ASTER-ERSDAC GDS Web site: http://gds.aster.ersdac.jspacesystems.or.jp/gds_www2002/news20100312_e.html

ASTER Mission (2004). Retrieved 08 07, 2013 from official ASTER website: http://asterweb.jpl.nasa.gov/

Canga E. F. (2002). Image fusion, MSc Thesis, University of Bath.

Collins B. H., Olsen R. C., and Hackwell J. (1997). Thermal Imagery Spectral Analysis, SPI E Vol. 3118, 0277-786.

Ehlers M., Klonus S., Astrand P. J., Rosso P. (2010) Multi-sensor image fusion for pansharpening in remote sensing, Institute for Geoinformatics and Remote Sensing, University of Osnabrueck, Osnabrueck, Germany.

Güngör O. (2008). Multi Sensor Multi Resolution Image Fusion, PhD. thesis, Purdue University.

Harish L., Jayanth J., Shivaprakash K., Kumar A. (2011). An Experimental Research on Fusion Algorithms of Remotely Sensed Image. International Journal of Advanced Computing and Intelligence, v.1, n.1.

Image Fusion (2007). Retrieved 05 07, 2013 from http://en.wikipedia.org/wiki/Image_fusion

Jeganathan C., Hamm N. A. S., Mukherjee S., Atkinson P. M., Raju P. L. N., Dadhwal V. K. (2011). Evaluating a thermal image sharpening model over a mixed agricultural landscape in India, International Journal of Applied Earth Observation and Geoinformation, VOL 13, Pages 178-191.

Jiménez-Muñoz J. C., Sobrino J. A. (2007). Feasibility of Retrieving Land-Surface Temperature from ASTER TIR Bands Using Two-Channel Algorithms: A Case Study of Agricultural Areas, IEEE Geoscience and Remote Sensing Letters, Vol. 4, No. 1.

Jing. (2008). Spectral Distortion Analysis in Image Fusion Algorithms for Remote Sensing and Development of Fusion Methods, PhD. Thesis, ProQuest Dissertations and Theses, York University.

Kaymakçı, N. (2000). Tectono-stratigraphical Evolution of the Çankırı Basin (Central Anatolia, Turkey). Ph.D. Thesis, Faculty of GeoScience (Vening Meinesz Research School of Geodynamics), Utrecht University.

Kaymakçı, N. Özçelik, Y. White, S.H. and Van Dijk, P.M. (2009). Tectono-stratigraphy of the Çankiri Basin: Late Cretaceous to Early Miocene evolution of the Neotethyan Suture Zone in Turkey. In: Van Hinsbergen, D.J.J., Edwards, M.A. and Govers, R. (eds.), Geodynamics of Collision and Collapse at the Africa-Arabia-Eurasia subduction zone, Geological Society of London London Special Issue, 311, 67-106.

Kaymakçı, N., Özçelik, Y., White, H. S., & Van Dijk, P. M. (2001). Neogene Tectonic Development of the Çankırı Basin (Central Anatolia, Turkey). The Bulletin of Turkish Association of Petroleum Geologists, 13(1), 27-58.

Klonus-Ehlers (2009). Performance of evaluation methods in image fusion. Proceedings of the 12th International Conference on Information Fusion, International Society of Information Fusion - IEEE, 1409-1416.

Kruse F. A. (2002). Combined SWIR and LWIR Mineral Mapping Using MASTER/ASTER, IEEE, 0-7803-7536.

Kumar. P. P. (2009) Image Fusion by Using Wavelets, Project Report, J.N.T. University Hayderabad.

Li, H. Manjunath, B.S. and Mitra, S.K. (1994). Multisensor image fusion using the wavelet transform. Graphical Models and Image Processing, 57:235–245.

Li J. (2000). Spatial Quality Evaluation of Fusion of Different Resolution Images, International Archives of Photogrammetry and Remote Sensing, Vol. XXXIII, Part B2, Amsterdam.

Li S., Yang B. (2011). A new pan-sharpening method using a compressed sensing technique, IEEE Transactions on Geoscience and Remote Sensing, VOL 49, NO 2.

MATLAB, version 7.12.0.635 (R2011a).

Malviya, A. and Bhirud, S. G. (2010). Objective Criterion for Performance Evaluation of Image Fusion Techniques, International Journal of Computer Applications, 1(25):57–60, Published By Foundation of Computer Science.

Nicolov S., Hill P., Bull D., Canagarajah N. (2000). Wavelets for image fusion, Proceedings of the 3rd International Conference on Information Fusion.

Ninomiya, Y., & Fu, B. (2002). Quartz index, carbonate index and SiO2 content index defined for ASTER TIR data. Journal of Remote Sensing Society of Japan, 22, 50-61.

Okyay Ü. (2012). Lithologic Discrimination and Mapping by ASTER Thermal Infrared Imagery, MScThesis, METU, Geological Engineering.

Oudre L. (2007). Study of two new spatial domain image fusion methods. MSc thesis, Imperial College London.

Öztan, N. S., & Süzen, M. L. (2011). Mapping Evaporate Minerals by ASTER. International Journal of Remote Sensing, 32(6), 1651-1673.

Sarup J., Singhai A. (2011). Image Fusion Techniques for Accurate Classification of Remote Sensing Data, International Journal of Geomatics and Geosciences, Volume 2, No 2.

Smith, A. M. (2012). *How to convert ASTER radiance values to reflectance: an online guide*. (C. o. Resources, Producer, & University of Idaho) Retrieved May 3, 2012, from www.cnrhome.uidaho.edu/default.aspx?pid=85984.

Strait M., Rahmani S., and Markurjev D. (2008). Evaluation of Pan-Sharpening Methods, UCLA Department of Mathematics. Retrieved 05 07, 2013 http://www.math.ucla.edu/~wittman/reu2008/Reports/pan_report.pdf

Tu T. M., Su, S. C., Shyu H. C., Huang P. S. (2001). A new look at IHS-like image fusion methods, Information fusion, Vol 2, 177-186.

Yamaguchi, Y., and Takeda, I. (2003). Mineralogical Mapping by ASTER in Cuprite, Nevada, USA. Asian Journal of Geoinformatics, 3(3), pp. 17-24.

Yin Z., Malcolm A. A. (2000). Thermal and Visual Image Processing and Fusion, SIMTech Technical Report (AT/00/016/MVS).

Yüksel, A., Akay, A. E., & Gündoğan, R. (2008). Using ASTER imagery in land use/cover classification of eastern Mediterranean landscapes according to CORINE land cover project. Sensors, 8, 1237-1251.